THEORETICAL AND EXPERIMENTAL STUDY ON OPTIMAL CONDITIONS IN CARBONATE ACIDIZING

A Dissertation

by

KAI DONG

Submitted to the Office of Graduate and Professional Studies of
Texas A&M University
in partial fulfillment of the requirements for the degree of

DOCTOR OF PHILOSOPHY

Chair of Committee,	A. Daniel Hill
Committee Members,	Ding Zhu
	Hisham Nasr-El-Din
	Charles Glover
Head of Department,	A. Daniel Hill

December 2015

Major Subject: Petroleum Engineering

ABSTRACT

Optimal acid injection rate is important to know for a carbonate matrix acidizing design. This rate is currently obtained through fitting acidizing coreflood experimental results. A model is needed to predict optimal acid injection rates for various reservoir conditions.

A wormhole forms when larger pores grow in cross-sectional area at a rate that greatly exceeds the growth rate of smaller pores due to surface reaction. This happens when the pore growth follows a particular mechanism, which is discussed in this study. Our model focuses on the growth of the pore with the mode size in a pore size distribution - the pore size that appears most frequently in the distribution. By controlling the acid velocity inside of it, we can make this particular pore grow much faster than other smaller pores, thus reaching the most favorable condition for wormholing. This also results in a balance between overall acid/rock reaction and acid flow. With the introduction of a porous medium model, the acid velocity in the mode-size pore is upscaled to the interstitial velocity at the wormhole tip. This interstitial velocity at the wormhole tip controls the wormhole propagation. The optimal acid injection rate is then calculated based on a semi-empirical flow correlation.

The optimal injection rate depends on the rock lithology, acid concentration, temperature, and rock pore size distribution. All of these factors are accounted for in this model. It can predict the optimal rates of acidizing coreflood experiments correctly for a variety of rock types, as compared with our acidizing coreflood experimental results. In addition, based on our model, it is also found that at optimal conditions, the wormhole

propagation velocity is linearly proportional to the acid diffusion coefficient for a diffusion limited reaction. This is proven both experimentally and theoretically in this study. Since there is no flow geometry constraint while developing this model, it can be applied to field scales. Applications are illustrated in this study.

Due to fundamental differences of flow geometries, upscaling the linear flow acidizing coreflood experimental results to field scale has limited success. In this work, the optimal conditions for field scale are calculated directly from the optimal interstitial velocity at the wormhole tip. This eliminates the need for core scale optimal conditions. A simulated case with published field data is studied. Acid pumping rate is optimized for this case. Since the model inputs can be readily obtained from drill cutting analysis, the need for downhole cores is eliminated, making this model more practical.

Acidizing coreflood experiments with dolomite cores at varying temperatures are carried out. The rock porosity, permeability and pore size distribution are measured. The dissolution patterns are found by CT scan the acidized cores. Together with the model developed in this work, a treatment design method is developed for acidizing dolomite formations. Besides, suggestions are also made for the treatment.

DEDICATION

Dedicated to my wife, Yuxin Huang, for her encouragement and love.

ACKNOWLEDGEMENTS

I would like to express my sincere gratitude to both Dr. A. Daniel Hill and Dr. Ding Zhu for admitting me into this group and helping me to choose this interesting topic; for their supervision and guidance through this research. I appreciate their patience and inspiration when I need time to think about the physics. And I also appreciate the opportunity they provided to broaden my professional knowledge. Thanks also to them for sharing their career and life experience. I learned a lot from them.

I would like to give my appreciation to Dr. Hisham Nasr-El-Din. His Well Stimulation class is very helpful for guiding me into matrix acidizing area. His advice on my theoretical research, suggestions on interpreting experimental data are valuable for this whole study. I can always get surprise while talking to him, both in office and elevator.

Thanks also to Dr. Charles Glover for being my committee member and for his interest in my topic. His Transport Phenomena class provides me a well-suited framework to begin my study, and formulate flow equations of this research. His comments and suggestions made throughout this study are very helpful.

I thank Haoran Cheng, Kenji Ueda, Jordan Etten and Vanessa Ndonhong in matrix acidizing group for their help and discussion. I also thank my colleagues in our research group. Working with them is enjoyable.

Thanks to John Maldonado for his help on cutting core samples for this research.

Thanks also to my friends at Texas A&M University. They make my life full of fun in the past years. I will always remember the days together with them.

Additionally, I would like to acknowledge the financial support from Acid Stimulation Research Project (ASRP), as well as the facility support of the Harold Vance Department of Petroleum Engineering.

NOMENCLATURE

A_p	Pore cross-sectional area, μm^2
$A_{p,\text{mode}}$	Cross-sectional area of the pore with the mode size, μm^2
A_{tip}	Wormhole tip flow area, μm^2
C_0	Bulk acid concentration, gmole/ml
C_{wall}	Acid concentration at wormhole wall, gmole/ml
C_{tip}	Acid concentration at wormhole tip, gmole/ml
C_s	Acid concentration at pore surface, gmole/ml
C_{bl}	Acid concentration inside the boundary layer, gmole/ml
D	Diffusion coefficient, cm^2/s
Da	Damkohler number, dimensionless
d_{wh}	Wormhole diameter, mm
d_{core}	Core diameter, inch
E_f	Surface reaction rate constant, $gmole^{1-n}cm^{3n-2}s^{-1}$
K	Acid mass transfer coefficient, cm/s
$L_{p,\text{mode}}$	Length of the pore with the mode pore radius, μm
$\bar{L}_p$	Average pore length of porous medium, μm
M	Acid molecular weight, g/gmole
M_i	i^{th} moment solution, cm^{2i-3}
M_0	0^{th} moment solution, cm^{-3}
M_1	1^{st} moment solution, cm^{-1}

M_2	2nd moment solution, cm
N	Number of pores per unit volume of porous medium, $1/cm^3$
N_p	Number of pores
N_{ac}	Acid capacity number, dimensionless
N_{kine}	Kinetic number, dimensionless
N_{pe}	Peclet number, dimensionless
Δp	Pressure drop, psi
PV_{bt}	Breakthrough pore volume, dimensionless
$PV_{bt,opt}$	Breakthrough pore volume at optimal conditions, dimensionless
q	Flow rate, cm^3/s
q_{tip}	Acid flow rate at wormhole tip, cm^3/s
r	Surface reaction rate, $gmole/cm^2/s$
r_p	Pore radius, μm
S_p	Pore surface area, um^2
t	Time, s
T_2	Transverse relaxation time, ms
v_i	Interstitial velocity, cm/s
$v_{i,opt}$	Optimal interstitial velocity, cm/s
$v_{i,tip}$	Interstitial velocity at wormhole tip, cm/s
$v_{i,tip,opt}$	Interstitial velocity at wormhole tip at optimal conditions, cm/s
$\bar{v}_p$	Average acid velocity in a pore, cm/s
$\bar{v}_{p,\mathrm{mode}}$	Average acid velocity in the mode-size pore, cm/s

$\bar{v}_{p,\mathrm{mode},opt}$	Average acid velocity in the mode-size pore at optimal conditions, cm/s
v_{wh}	Wormhole propagation velocity, cm/s
$v_{wh,opt}$	Wormhole propagation velocity at optimal conditions, cm/s
w^2	Flow area, cm^2

Greek

β	Acid gravimetric dissolving power, mass rock/mass acid
ε	Flow coefficient in Hagen-Poiseuille's equation, $cm^{-1}s^{-1}$
κ	Overall reaction rate coefficient, cm/s
μ	Viscosity, mPa·s
Γ_p	Pore perimeter, μm
ρ_a	Acid density, g/cm^3
ρ_r	Rock density, g/cm^3
ρ_2	Surface relaxivity, μm/s
η	Pore size density function, $1/cm^5$
Ψ	Pore growth function, cm^2/s
χ	Acid volumetric dissolving power, volume rock/volume acid

Subscripts

tip	Wormhole tip
opt	Optimal condition

p	Pore
mode	Mode pore size
wh	Wormhole
bl	Boundary layer

TABLE OF CONTENTS

Page

LIST OF FIGURES

Page

LIST OF TABLES

1 INTRODUCTION

1.1 Background

Carbonate matrix acidizing is one of the oldest well stimulation techniques. Acids are pumped below the formation fracturing pressure, through the wellbore to the formation, creating wormholes that can bypass formation damage. In order to have the best stimulation results, wormholes need to be designed to penetrate through the damaged area, and reach the longest possible distance.

Acid flow rate plays an important role in an acidizing treatment. The wormhole efficiency relationship reveals that the best wormholing efficiency can be achieved at a certain acid flow rate, namely the optimal acid injection rate. If acid flow rate is lower than the optimal flow rate, a significant amount of acid is used when wormhole breaks through the core. In a field treatment, low acid flow rate produces almost no stimulation results at all. Higher acid flow rate causes additional acid to be wasted creating branches along the dominant wormhole, which decreases its ultimate length. **Fig. 1.1** shows the wormhole efficiency relationship and corresponding wormhole structures. In order to have a successful treatment, acid needs to be pumped with optimal rate or a little higher.

Optimal conditions can be very different with varying conditions, like temperature, acid type/concentration and rock types. It is difficult to select a proper acid and determine its optimal injection rate based solely on limited downhole cores. Therefore, a model is needed to predict the optimal condition for a particular situation. It is in this background that we carry out a detailed study on optimal conditions of carbonate acidizing.

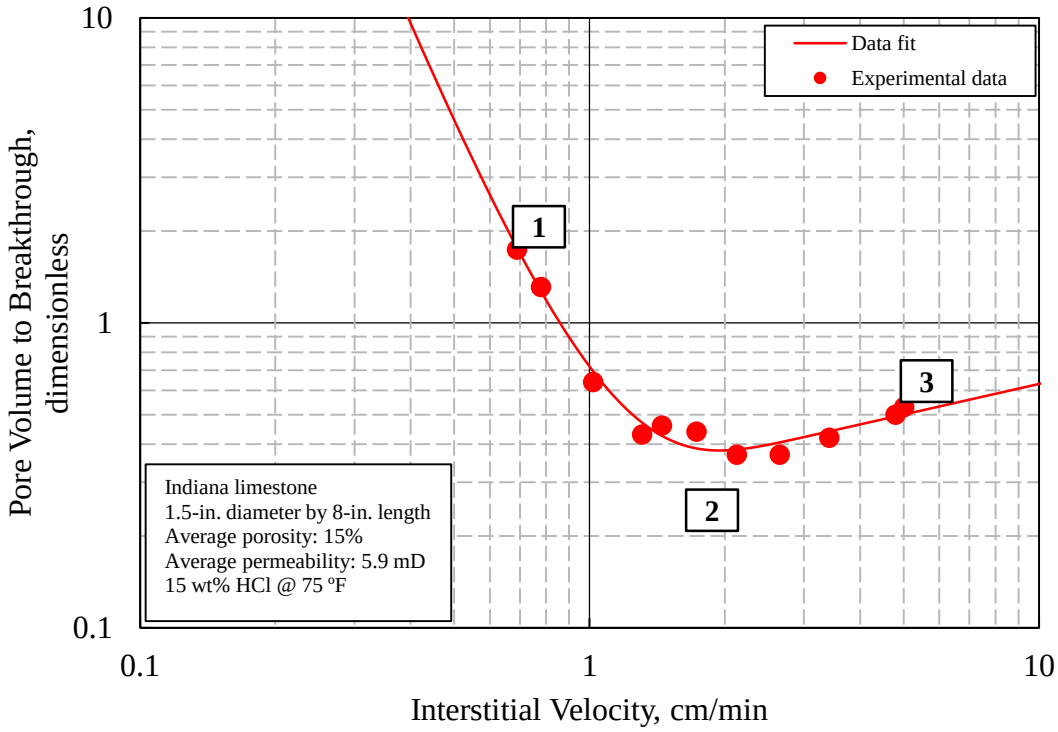

Fig. 1.1a Wormhole efficiency relationship (Dong, 2012)

Fig. 1.1b Wormhole castings

1.2 Literature Review

Research on carbonate acidizing process can be grouped into three categories, pore-scale research, core-scale research, and field-scale research.

1.2.1 Pore Enlargement and Wormhole Formation

When acid is introduced into a rock, it reacts with its minerals and change its pore structure. The macro properties like porosity and permeability of the rock change accordingly. In order to describe this phenomenon more precisely, Schechter and Gidley (1969) studied the changes of pore structure and pore size distribution due to surface reaction. They set up a porous medium model with pores represented by capillaries distributed randomly. Pore enlargement is described by a pore growth function and the change of pore size distribution is described by a pore evolution function. They concluded that it is the larger pores that determine the response of rocks to acid attack for high surface reaction rates, and this response is sensitive to the distribution of these larger pores, as shown in **Fig. 1.2**. It shows that the distribution of larger pores change with time while the distribution of smaller pores remain the same.

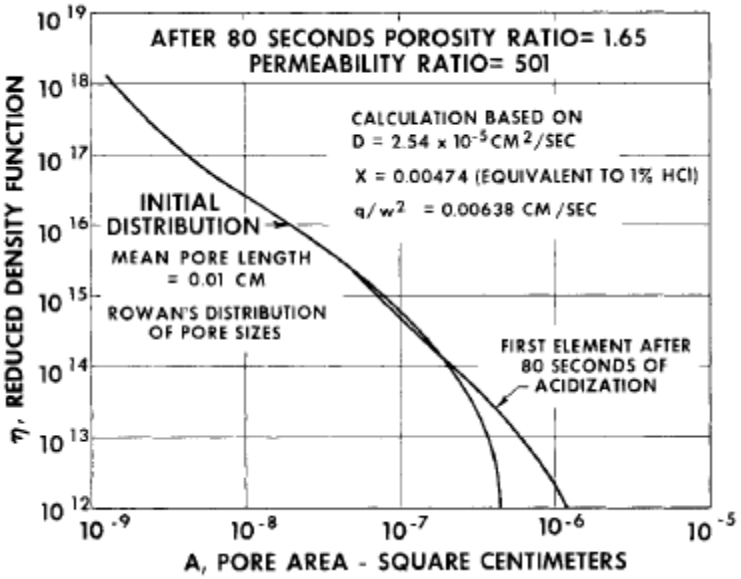

Fig. 1.2 The change of pore size distribution with time due to acid/rock surface reaction (Schechter and Gidley, 1969)

The effectiveness of this model was verified experimentally with retarded acid injected into sintered glass disk (Guin et al. 1971). Excellent agreement was obtained for permeability increase between experiments and model prediction. Furthermore, the pore evolution equation was solved by a simulation procedure using Monte Carlo techniques (Guin and Schechter 1971). Besides pore enlargement, the collisions between neighboring pores were also accounted for in this simulation. They found that for diffusion-controlled reactions (high surface reaction rate), wormholes tend to occur and acid preferentially flows through these channels. It is best explained by the enlargement of larger pores and collisions between them. This process is independent of the fine pore distribution since the fine pores receive little acid.

Network modeling was developed to simulate wormhole initiation and formation (Hoefner and Fogler 1988). The network consists of nodes connected by bonds of cylindrical tubes. In order to be close to real rock, the pore size distribution was repeatedly simulated until good agreement with an experimentally determined distribution was obtained. The bond growth rate was studied for both diffusion limited and reaction limited cases. They found that if the bond growth is limited by diffusion, a dominant wormhole can form; if the bond growth is limited by surface reaction, permeability increases very little and no channel forms.

Pore growth modeling laid the foundation for wormhole modeling. Next section introduces the research on wormhole propagation.

1.2.2 Wormhole Propagation

Hung et al. (1989) developed a mechanistic model to describe wormhole tip propagation. This model is based on rock/acid mass balance at the wormhole tip and has a general application. His model reveals that wormhole propagation velocity has a linear relationship with acid capacity number, acid interstitial velocity at the wormhole tip, and the ratio of tip acid concentration to original acid concentration.

Daccord, G. et al. (1989) performed experiments by injecting water into plaster to simulate a radial wormhole propagation process. He then described the whole wormhole pattern using a single parameter called “equivalent size”, and formulated the wormhole growth. He found that the dimensionless wormhole propagation velocity is proportional to the injection rate to the power of -1/3. If converted to real wormhole propagation

velocity, it is proportional to the injection rate to the power of 2/3 (Daccord, G. et al. 1993). Further studies show that this relationship is valid for both linear case and radial case. However, this model is only valid when acid flux is larger than the optimal acid flux. If acid flux is approaching zero, the wormhole propagation velocity becomes infinite in this model, which makes it unpractical.

Both Hung et al and Daccord, G et al developed a relationship between wormhole propagation velocity and injection rate. Significant difference exits between them. The relationship developed by Hung et al describes instantaneous propagation of the wormhole tip. The one from Daccord, G et al, however, describes an average wormhole velocity for the whole core.

Buijse and Glasbergen (2005) developed a semi-empirical model to correlate wormhole propagation velocity and acid injection rate. Recently their model is used to fit acidizing coreflood experimental data, as shown in Fig. 1.1a. While using this model, two parameters are needed, optimal interstitial velocity and corresponding optimal breakthrough pore volume. These two parameters can be obtained by experiments. Like the correlation from Daccord, G et al, this model also describes an average wormhole propagation velocity for the whole core.

Wormhole competition commonly exists during the acidizing process, both in linear and radial flow geometry. In an acidizing coreflood experiment, only one dominant wormhole is usually formed, while other wormholes cease growing at some point, as can be seen from various wormhole CT images. The existence of multiple wormholes affects the pressure field, and thus the acid flow profile. Longer wormholes accepts more acid

than shorter wormholes (Hung et al, 1989), and propagate even faster. Once the fluid behind the dominant wormhole is fully compressed, virtually all acid flows into the dominant wormhole and drives its propagation. For acidizing along the wellbore, how wormholes compete with each other is important to know for a treatment design. Huang et al. (1999) numerically studied the flow field around the wellbore with an existing wormhole extended into formation. The wormhole population density along the wellbore was thus studied.

1.2.3 Optimal Conditions of Carbonate Acidizing

Experimental results have shown that the best wormholing efficiency can be obtained at a certain acid injection rate. We call this the optimal conditions. Extensive work has been done to study this particular condition, both experimentally and theoretically.

Acidizing coreflood experiments are an important method to determine the optimal conditions for a specific acid/carbonate system. The experimental setup usually consists of a syringe pump, acid/brine accumulators, a coreholder and a backpressure regulator. Brine is injected at a constant flow rate to measure core permeability, and thereafter acid is injected at a constant flow rate. The volume of consumed acid is measured when wormhole breaks through the core. Repeated experiments with different acid injection rates are needed to find the optimal condition.

Through acidizing coreflood experiments, several investigators have studied factors that affect the optimal conditions. These factors include reservoir temperature, HCl concentration, carbonate rock types. In general, increasing temperature can make both the

optimal acid flux and the corresponding optimal breakthrough pore volumes become larger. Higher acid concentration results in larger optimal acid flux and lower optimal breakthrough pore volumes. The optimal breakthrough pore volumes for dolomite is larger than that of limestone.

Other than experiments, different models for predicting optimal conditions have also been developed.

Wang's (Wang et al. 1993) model focused on the largest pores naturally existing in a rock. A transition pore area was defined, that was used to distinguish the growth mechanisms of small pores and large pores. If the area of a pore is larger than this transition pore area, this pore grows rapidly and a wormhole can form. To some extent, her model can predict the optimal acid injection rate for linear coreflood acidizing experiments. However, the surface reaction rate is used to represent the overall reaction rate in her model, with diffusion rate being ignored. This leads to an incorrect prediction of temperature effect. Besides, the method for calculating optimal pore volumes to breakthrough ($PV_{bt,opt}$) is not developed in her model.

Gong and El-Rabaa (1999) developed a correlation to calculate the optimal conditions using flow/reaction dimensionless numbers. Fundamentally, this model is based on Daccord's model. They calculated the derivatives of the diffusion limited relationship and made it equal to zero. The idea is that the minimum point of a curve has a zero derivative. Unfortunately, the optimal injection rate calculated from this model is orders of magnitude less than the experimental results.

Panga et al. (2005) studied different conditions of dissolution patterns based on the ratio of transverse to axial length scales. He showed that when the transverse length scale and the axial length scale are of the same order, the optimal condition happens. Furthermore, he studied the optimal conditions for kinetically controlled reaction and mass transport controlled reaction separately. However, experimental and theoretical studies have shown that kinetically controlled reaction produce uniform dissolution but not wormholing dissolution.

Fredd and Fogler (1999) studied the effects of transport and reaction on wormholing process using a wide range of reactive fluids. The optimal conditions were identified for low concentration HCl, EDTA, CDTA, DTPA and HAc with Indiana limestone respectively. They defined the Damkohler number as the ratio between the overall acid reaction rate at the wormhole wall and the acid flow rate in the wormhole. They found that when the Damkohler number equals to 0.29, the optimal condition can be achieved for all the reactive fluids they studied. However, in order to have this Damkohler number available, a pre-existing wormhole diameter and length need to be identified, which limits its application.

Generally, models for optimal conditions are progressing. With more experimental data available, more physics can be unveiled. The development of a reliable model becomes eventually possible.

1.2.4 Application of Lab Results to Field Design

The flow geometries in the field are typically observed as radial flow and spherical flow during the acidizing treatment (Furui et al. 2010). Unlike acidizing coreflood experiment, acid pumping rate needs to increase continuously to compensate increasing acid loss into formation. Research have been carried out to apply linear acidizing coreflood experimental results to field scales, but limited success has been achieved.

Based on Buijse and Glasbergen's model, Furui et al. (2012) incorporated Hung's mechanistic model and his linear flow relationship into it. After model combination and variable transformation, Furui's model focuses on the wormhole tip interstitial velocity, instead of acid interstitial velocity across the whole formation. His model can be used to predict wormhole propagation distance for a given amount of acid in field conditions. In order to use this upscaling model, we need to know the optimal interstitial velocity ($v_{i,opt}$) and corresponding optimal breakthrough pore volume ($PV_{bt,opt}$). As input parameters, these two values need to be obtained through linear acidizing coreflood experiments.

1.3 Problem Description, Objectives and Significance

Matrix acidizing is widely used to stimulate wells in carbonate reservoirs. Among all factors, acid type and its pumping rate are the most important factors for a successful treatment. Currently, industry tends to pump acid using maximal pumping rate below fracturing pressure. This could cause several problems. For a particular acid, if the maximal pumping rate results in fluxes lower than the optimal flux, compact dissolution occurs, which results in minimal stimulation. If the maximal pumping rate results in fluxes

higher than the optimal flux, acid is wasted creating branches along the dominant wormholes. Besides, other than HCl, organic acids and chelating agents are also commonly used to stimulate wells in carbonate reservoirs. It is difficult to select a proper acid and determine the optimal injection rate based solely on coreflood experiments. So detailed theoretical study is needed to calculate optimal injection condition for a particular acid/rock system.

In the meanwhile, different methods are attempted to make use of linear acidizing coreflood experimental results, but improvements are needed. Our method developed in this study starts from physics happening at the wormhole tip, which is only a function of reservoir/acid properties, and upscale them to the field scale directly, without the need for core scale data.

This is the reason that we carry out this scientific and systematic study on the optimal conditions of carbonate acidizing. Our model can be used to predict a priori the type of acid used and its pumping rate. In order to achieve this, the following objectives are set for this study.

(1) To gather all pre-existing acidizing coreflood experimental data, analyze the effects of temperature and acid concentration on the optimal conditions qualitatively.

(2) To characterize pore size distribution of different carbonate rocks. Identify the size of pores that appear most frequently in the rock, which is the mode of the pore size in a distribution.

(3) To develop a model that calculates the optimal acid interstitial velocity at the wormhole tip ($v_{i,tip,opt}$), for different acid/carbonate systems.

(4) To upscale the wormhole tip interstitial velocity to different flow geometries, from core scale with linear flow geometry to field scale with radial flow or spherical flow geometries. The results are verified with existing experimental results and published field data.

(5) To quantitatively study the effects of temperature and acid concentration on the optimal conditions.

1.4 Approach

In order to complete this study, both theoretical and experimental approaches are used. Theoretically, a model for optimal conditions is derived. Acidizing coreflood experiments are used to calibrate the model and verify its effectiveness. In addition, the pore properties of rocks in this study are examined by using Micro-CT Scanner, Thin Section and Nuclear Magnetic Resonance (NMR).

1.4.1 Theoretical Approach

The theory developed in this work aims to predict the optimal condition for a particular acid/carbonate rock system. In the meanwhile, the effects of temperature and acid concentration are quantified through this theory. The effect of rock lithology is also discussed based on this theory. It consists of steps described below.

- The overall chemical reaction between acid and the pore surface is modeled. An acid mass balance equation inside of a single pore is solved to get acid concentration distribution.
- Pore growth function is derived based on acid/rock mass balance equation. This function describes the rate of change of pore cross-sectional area with time.
- Through further analysis of pore growth function, a transition pore area is found that divides the growth function into two different growth mechanisms. By making the mode of the pore size distribution equal to the transition pore size, the optimal acid velocity in the mode-size pores ($\bar{v}_{p,\mathrm{mode},opt}$) can be obtained.
- A porous medium model is introduced, which is used to upscale the acid velocity in the mode-size pore to the acid flux in the porous medium.
- Based on numerical simulation study and experimental study, wormhole tip region is selected for further investigation. By upscaling $\bar{v}_{p,\mathrm{mode},opt}$ to the wormhole tip region, the optimal interstitial velocity at the wormhole tip ($v_{i,tip,opt}$) can be obtained.
- Optimal injection rates for different flow geometries can be upscaled based on $v_{i,tip,opt}$, using different flow relationships.

The flowchart shown in **Fig. 1.3** below briefly describes the theoretical work.

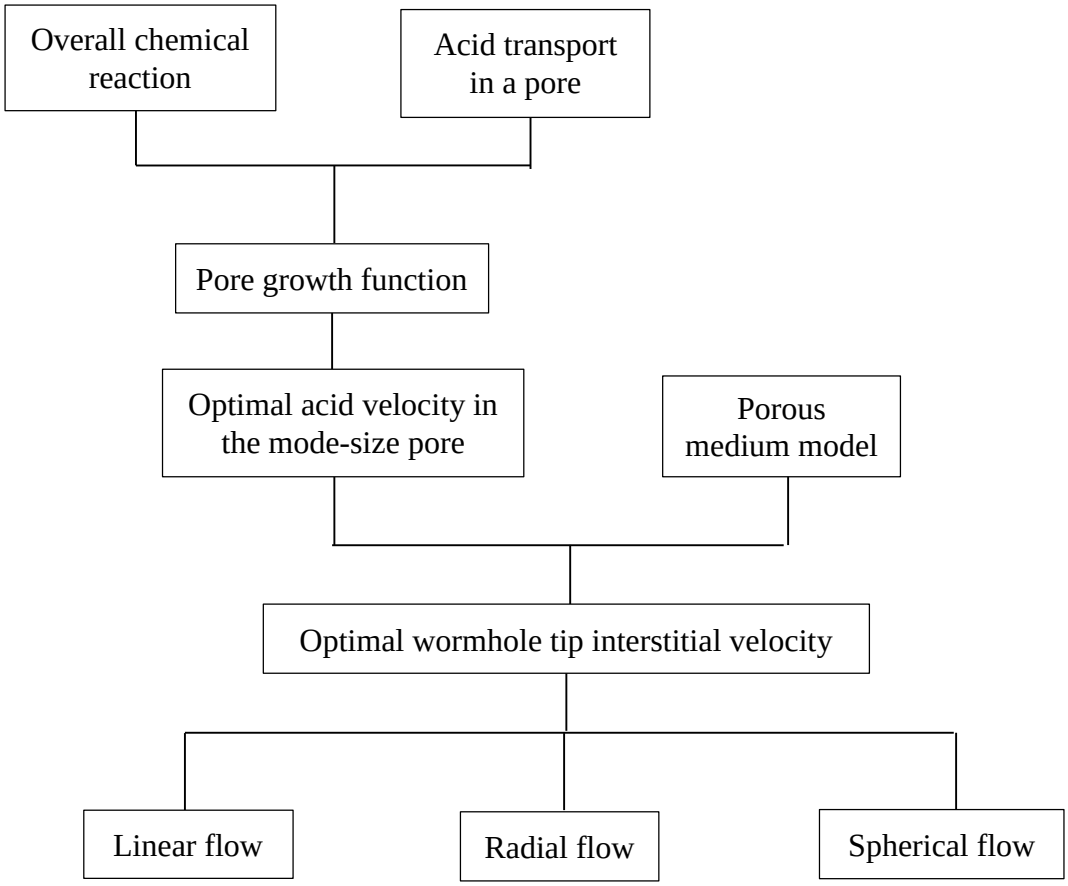

Fig. 1.3 Framework of the theoretical study

1.4.2 Experimental Approach

In order to verify the validity of this model, acidizing coreflood experiments are carried out to obtain the optimal conditions for different acid/rock combinations. Factors that affect the optimal conditions include acid concentration, temperature, and lithology. Experiments are designed to isolate each variable and study its effect individually. Procedures for experimental approach are shown below:

(1) Collect representative carbonate samples and characterize them. These rocks include four types of limestone and one type of dolomite.

(2) Study rock pore structures and pore size distributions.

(3) Perform a series of acidizing coreflood experiments at pre-designed experimental conditions, e.g. specific temperature, acid concentration etc. Obtain optimal conditions for each set of experiments.

The experimental setup is shown in **Fig. 1.4** below. Procedures on how to complete individual experiment can be found in Dong (2012).

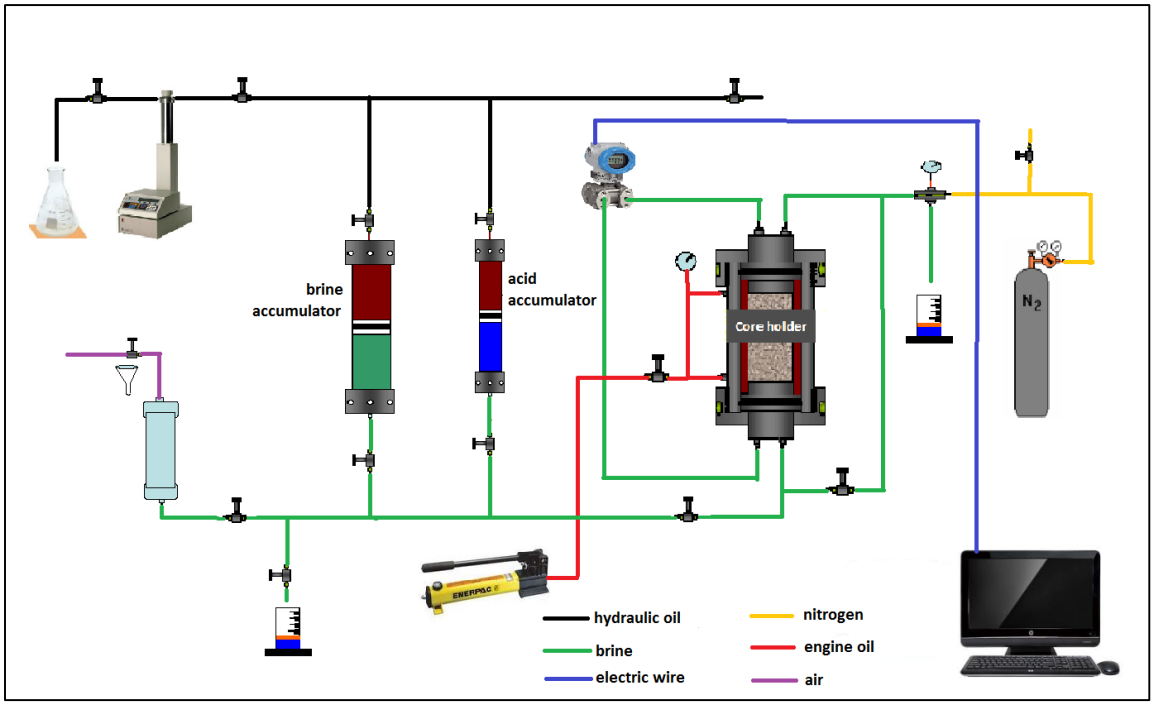

Fig. 1.4 Acidizing coreflood experimental setup

The flowchart shown in **Fig. 1.5** briefly describes the experimental work.

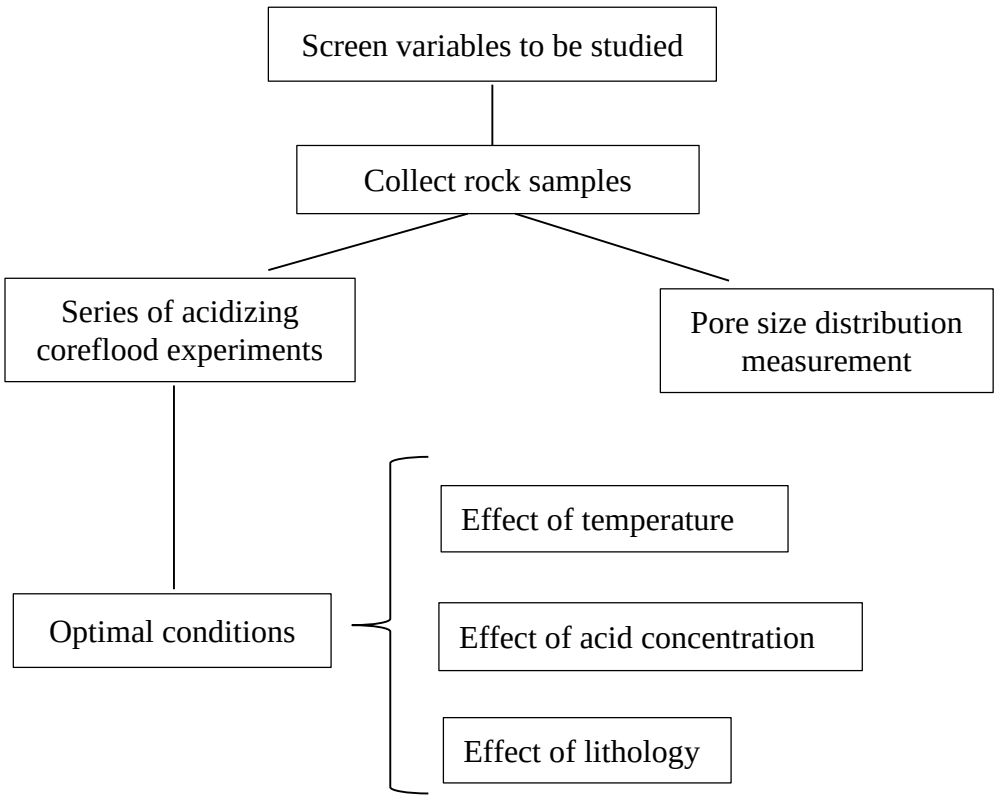

Fig. 1.5 Framework of the experimental study

1.5 Dissertation Outline

In this dissertation, Section 1 gives the general background of this research by reviewing the literature; then objectives of this research are stated. The importance of this research is also discussed.

In Section 2, a new model is developed to calculate optimal conditions of carbonate acidizing. It first describes pore enlargement mechanism. Acid flow velocity in the mode-

size pore is then calculated. A porous medium model is used to upscale the flow velocity from pores to the bulk porous medium. After that, fluid loss during acidizing is studied and wormhole diameter is calculated. A semi-empirical flow relationship is introduced to calculate the optimal acid injection rate.

Section 3 analyzes the sensitivity of wormhole propagation, both experimentally and theoretically. The factors to be studied are temperature and acid concentration. The effects of pore structure and pore size distribution are briefly discussed.

Section 4 discusses a method to upscale acidizing coreflood experimental results to field design. A field case study is illustrated.

Section 5 presents a comprehensive model application for acidizing of a dolomite formation. Both experimental study and theoretical study are carried out. Acid treatment suggestions are made.

Section 6 summarizes the whole work and conclusions are made. In addition, recommendations are made for future study.

2 OPTIMAL CONDITIONS OF CARBONATE ACIDIZING

2.1 Introduction

A successful carbonate acidizing treatment strongly depends on the acid injection rate. From the wormhole efficiency relationship, if acid pumping rate is lower than the optimal pumping rate, a significant amount of acid is consumed. The wellbore is enlarged and yet no wormholes formed. A conservative method is to pump acid using the highest flow rate of the pumping unit, expecting this rate is higher than the optimal rate. Therefore, even with this conservative method, it is also important to determine the optimal pumping rate a priori for a specific acid/rock system.

The sequence of this section is arranged as follows. First, wormholing mechanism is explained on the pore scale. After that, a method to calculate the optimal interstitial velocity at the wormhole tip is developed. Then this tip interstitial velocity is upscaled based on fluid loss analysis. In the end, a calculation example is presented.

2.2 Mechanism of Wormholing

2.2.1 Overall Chemical Reaction

The overall chemical reaction in this study involves acid diffusion to the rock surface and acid/rock surface reaction. In chemical engineering, this is one type of heterogeneous chemical reaction, which is defined as a reaction happening between two different phases. In this work, the liquid phase is acid, and the solid phase is the pore wall. The liquid phase

consists of the bulk fluid and the diffusional boundary layer. An acid concentration gradient exists in the diffusional boundary layer, as shown in **Fig. 2.1**.

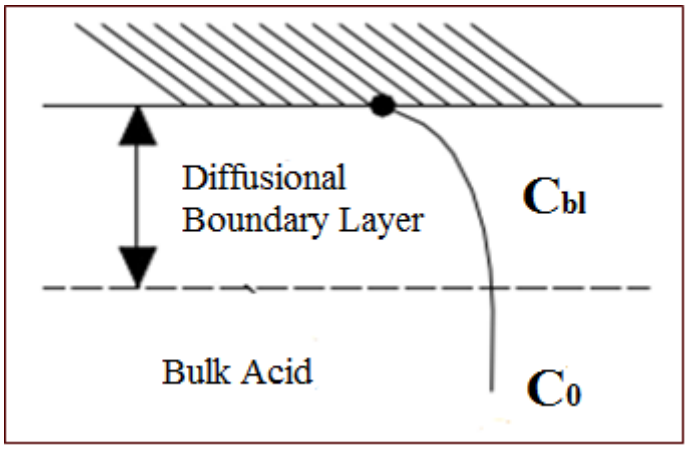

Fig. 2.1 Overall chemical reaction

When the chemical reaction in the diffusional boundary layer is at steady state, the rate of acid diffusing to the pore surface equals to the rate of surface reaction. We can describe the boundary condition using Eq. 2-1 below

$$D(\frac{\partial C_{bl}}{\partial n}) = E_f C_s^m \qquad (2\text{-}1)$$

where D is the acid diffusion coefficient, C_{bl} is the acid concentration in the diffusional boundary layer, n is the outward normal, E_f is the surface reaction rate constant, C_s is the surface acid concentration and m is the reaction order.

The boundary condition can be written as another form with dimensionless variables, by introducing $C_D=C/C_0$ and $N=n/L$. Then the boundary condition becomes

$$\frac{D}{E_f L C_0^{m-1}}\left(\frac{\partial C_{D-bl}}{\partial N}\right)_{y=0} - C_{D-s}^{m} = 0 \tag{2-2}$$

where C_0 is the acid bulk concentration, L is the diffusional boundary layer thickness, $C_{D\text{-}bl}$ is the dimensionless acid concentration in the diffusional boundary layer and $C_{D\text{-}s}$ is the dimensionless surface acid concentration.

The coefficient of the first term in Eq. 2-2 denotes the ratio between acid mass transfer rate and surface reaction rate. It is defined as kinetic number.

$$N_{kine} = \frac{D}{E_f L C_0^{m-1}} \tag{2-3}$$

The diffusional boundary layer thickness L can be obtained by solving acid convection diffusion equation inside the boundary layer. However, this parameter can be reduced by introducing a mass transfer coefficient K, which is the ratio between the diffusion coefficient D and the diffusional boundary layer thickness L (Levich, Veniamin G, 1962).

$$K = \frac{D}{L} \tag{2-4}$$

Levich V.G (1962) also derived the equation to calculate the mass transfer coefficient K as shown by Eq. 2-5.

$$K = 1.2819\left(\frac{\bar{v}_p}{r_p L_p}\right)^{1/3} D^{2/3} \tag{2-5}$$

where $\bar{v}_p$ is the average acid velocity in the pore, which is averaging the parabolic velocity profile in the pore, as shown in **Fig. 2.2**; r_p is the pore radius, and L_p is the pore length.

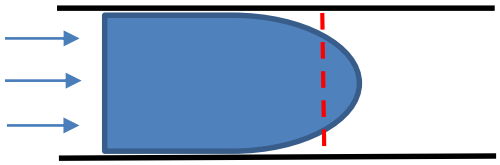

Fig. 2.2 Acid flow velocity profile in a pore. The velocity profile is parabolic, and the average velocity is denoted as the red dash line

In order to determine if a reaction is diffusion limited or surface reaction limited, the relative importance of K and $E_f C_0^{m-1}$ needs to be analyzed. Eq. 2-2 can be written in another form as Eq. 2-6.

$$K(C_0 - C_s) = E_f C_0^{m-1} C_s \tag{2-6}$$

The surface acid concentration C_s is difficult to determine and it can be reduced through Eq. 2-6, and is shown by Eq. 2-7.

$$C_s = \frac{KC_0}{K + E_f C_0^{m-1}} \tag{2-7}$$

Substituting Eq. 2-7 into either side of Eq. 2-6, we can then get an overall reaction rate equation and overall reaction rate coefficient.

$$r = \kappa C_0 \tag{2-8}$$

$$\kappa = \frac{KE_f C_0^{m-1}}{K + E_f C_0^{m-1}} \tag{2-9}$$

In Eq. 2-9, if $K >> E_f C_0^{m-1}$, the surface reaction rate is slow and is the limiting step of the overall reaction. In this case, $\kappa = E_f C_0^{m-1}$. If $K << E_f C_0^{m-1}$, the diffusion rate

is slow and is the limiting step of the overall reaction. In this case, $\kappa = K$. In order to better understand this equation, a plot of it is shown in **Fig. 2.3**, with $K = 1\text{cm/s}$.

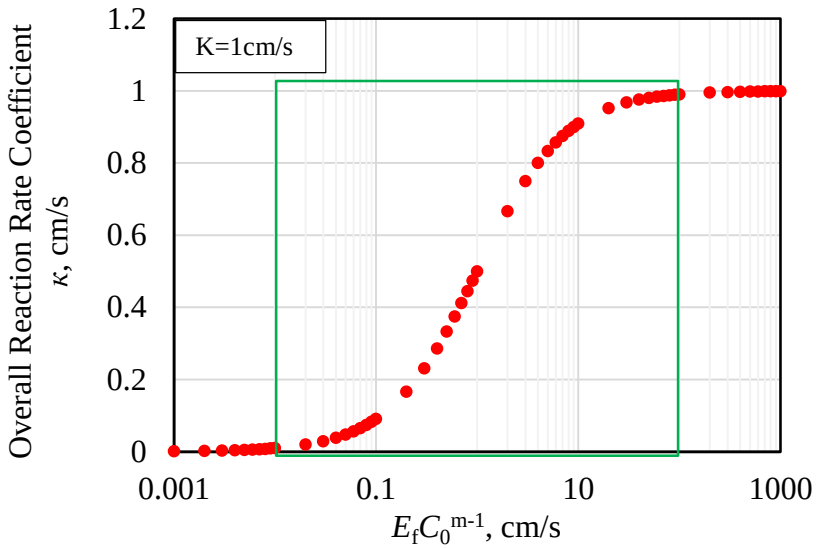

Fig. 2.3 Overall reaction rate coefficient

We can see from Fig. 2.3, if $E_f C_0^{m-1}$ and K are within around 100 times difference, both of the surface reaction rate and convective diffusion rate play roles on the overall reaction rate. The overall reaction is mixed kinetics. Otherwise, it is solely dependent on one of them.

In order to use these parameters and equations properly, the units of them are summarized in **Table 2.1**.

Table 2.1 Parameter units for overall reaction rate calculation

K	cm/s
C_0	gmole/ml
$E_f C_0^{m-1}$	cm/s
r_p	cm
L_p	cm
D	cm^2/s
$\bar{v}_p$	cm/s

2.2.2 Pore Growth Function

When acid is flowing in a pore, it tends to react with the pore surface and enlarge the pore cross-sectional area. A pore growth function is used to describe its growth mechanism. It is first derived by Schechter and Gidley (1969). For consistency, the derivation is brought here in this section. The difference with the original derivation is that the overall reaction rate is used here instead of surface reaction rate used originally.

Assuming the acid flow in a pore is steady state and acid is incompressible, and the parabolic acid flow profile is averaged by a constant flow velocity $\bar{v}_p$, an acid mass balance equation and its boundary condition can be described by Eq. 2-10. The particular pore of interest is depicted by **Fig. 2.4**.

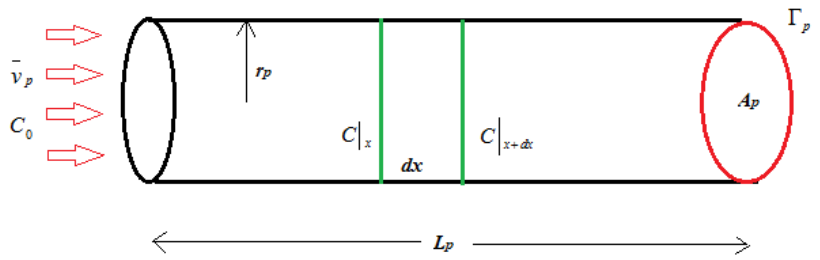

Fig. 2.4 Sketch description of acid flowing through a cylindrical pore

$$(C\big|_{x+dx} - C\big|_x) \cdot A_p \cdot \bar{v}_p = -\kappa C \cdot \Gamma_p \cdot dx$$
$$C\big|_{x=0} = C_0 \tag{2-10}$$

where A_p is the pore cross-sectional area and Γ_p is the pore perimeter. The subscript p denotes pore. This equation describes the change of acid concentration in a unit volume equals to the amount of acid that is reacted with the pore surface. By solving Eq. 2-10, we can get the acid concentration distribution along the pore, as shown by Eq. 2-11 below

$$C = C_0 \exp(-\frac{\kappa \Gamma_p x}{A_p \bar{v}_p}) \tag{2-11}$$

For a limited time dt, the mass of rock dissolved can be related to the mass of acid consumed through the acid dissolving power.

$$\rho_r dA = \kappa C \cdot M \cdot \beta \cdot \Gamma_p dt \tag{2-12}$$

where ρ_r is the rock density and M is the acid molecular weight. The pore growth rate is the rate of change of the pore cross-sectional area, and can be described by Eq. 2-13.

$$\frac{dA}{dt} = \frac{\kappa C M \beta \Gamma_p}{\rho_r} \tag{2-13}$$

If we integrate the pore growth rate along the pore length, we can get the average pore growth rate, namely pore growth function as shown by Eq. 2-14 below

$$\psi = (\frac{dA}{dt})_{ave} = C_0 \frac{\beta M A_p \bar{v}_p}{\rho_r L_p}[1-\exp(-\frac{\kappa \Gamma_p L_p}{A_p \bar{v}_p})] \tag{2-14}$$

The volumetric dissolving power χ is

$$\chi = \frac{C_0 \beta M}{\rho_r} \tag{2-15}$$

Substituting Eq. 2-15 into Eq. 2-14, the pore growth function can be written as

$$\psi = \frac{\chi A_p \bar{v}_p}{L_p}[1-\exp(-\frac{\kappa \Gamma_p L_p}{A_p \bar{v}_p})] \tag{2-16}$$

As indicated by Eq. 2-16, the pore growth function depends on acid/rock reaction, rock pore properties and acid flow velocity inside the pore. While analyzing the pore growth, there are four categories of limits to be discussed. They are slow surface reaction and fast surface reaction, small pores and large pores.

Slow surface reaction: $E_f \to 0$, $\kappa = E_f C_0^{m-1} \approx 0$. The exponential term in Eq. 2-16 is close to 0. From Taylor Series expansion,

$$\psi_{slow} = \frac{\chi A_p \bar{v}_p}{L_p}[1-(1-\frac{E_f C_0^{m-1} \Gamma_p L_p}{A_p \bar{v}_p})] = E_f C_0^{m-1} \chi \Gamma_p = 2\sqrt{\pi} E_f C_0^{m-1} \chi A_p^{1/2} \tag{2-17}$$

Fast surface reaction: $E_f \to \infty$, $\kappa = K$. Eq. 2-16 becomes

$$\psi_{fast} = \frac{\chi A_p \bar{v}_p}{L_p}[1-\exp(-\frac{K \Gamma_p L_p}{A_p \bar{v}_p})] \tag{2-18}$$

Hagen Poiseuille's law states that with the same pressure gradient, flow velocity is linearly proportional to the flow cross-sectional area for the pipe flow, as shown in Eq. 2-19 and 2-20.

$$q = -\frac{\pi r^4}{8\mu}\frac{\Delta p}{l} = -\frac{1}{8\pi\mu}\frac{\Delta p}{l}A^2 \tag{2-19}$$

$$\bar{v} = \frac{q}{A} = -\frac{1}{8\pi\mu}\frac{\Delta p}{l}A = \varepsilon A \tag{2-20}$$

where $\varepsilon = -\frac{1}{8\pi\mu}\frac{\Delta p}{l}$, r is the pipe radius, A is the pipe cross-sectional area, l is the pipe length, μ is the fluid viscosity, and Δp is the pressure difference across the pipe length, q is the flow rate and $\bar{v}$ is the average flow velocity in the pipe. Substituting Eq. 2-20 into Eq. 2-18, we can get Eq. 2-21.

$$\psi_{fast} = \frac{\varepsilon\chi A_p^2}{L_p}[1-\exp(-\frac{K\Gamma_p L_p}{\varepsilon A_p^2})] \tag{2-21}$$

For fast surface reaction, the exponential term determines the final form of the growth function. In order to understand this equation better, the exponential function is plotted in **Fig. 2.5**. If the exponential term in Eq. 2-21 is less than around -5, then $\psi \sim A^2$. However, it is not always achieved. In most cases, small pores grow based on $\psi \sim A^2$, because the exponential term is large. Large pores tend to grow based on $\psi \sim A^{2/3}$ because the exponential term is small.

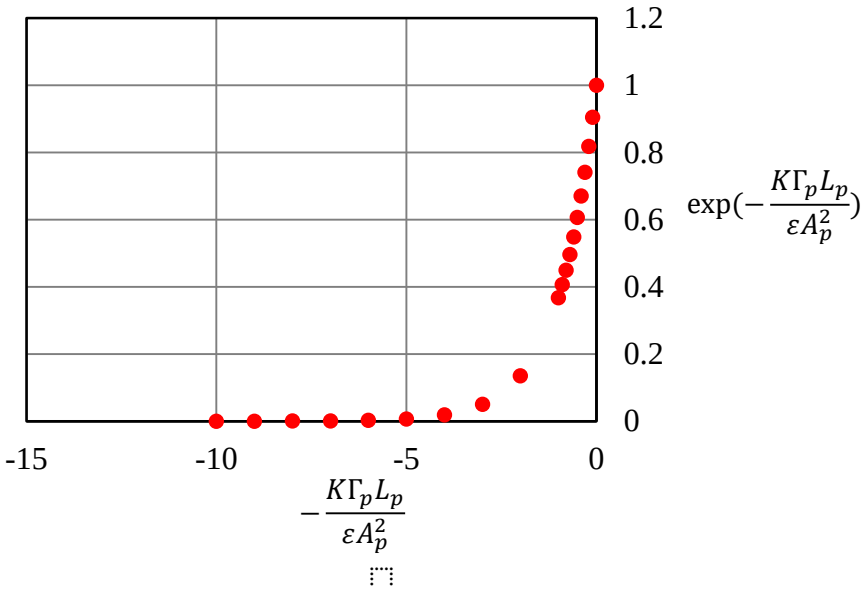

Fig. 2.5 Exponential term in Eq. 2-21

An example is given to show the pore growth for fast surface reaction. There are four pores to be investigated, with pore radius 30 μm, 10 μm, 5 μm and 1 μm respectively. The pore length is 10 times pore radius for each pore. The reaction is for 15 wt% HCl and limestone at room temperature. **Table 2.2** shows the input data. The calculation finishes when the largest pore reaches 10 times its initial area. That is when the pore with radius 30 μm reaches a pore area of 9000π μm^2.

Table 2.2 Input data for fast reaction

Volumetric dissolving power, χ	0.082	volume $CaCO_3$ per volume 15 wt% HCl
Diffusion coefficient, D	3.5×10^{-5}	cm^2/s
ε	10^6	$cm^{-1}s^{-1}$
First pore radius, r_{p1}	1	μm
First pore length, L_{p1}	10	μm
Second pore radius, r_{p2}	5	μm
Second pore length, L_{p2}	50	μm
Third pore radius, r_{p3}	10	μm
Third pore length, L_{p3}	100	μm
Fourth pore radius, r_{p4}	30	μm
Fourth pore length, L_{p4}	300	μm

Fig. 2.6 shows the pore growth rate and its slope for the four different pores. We can see that with the increase of pore area, pore growth rate increases, but its slope tends to decrease from 2 to 2/3.

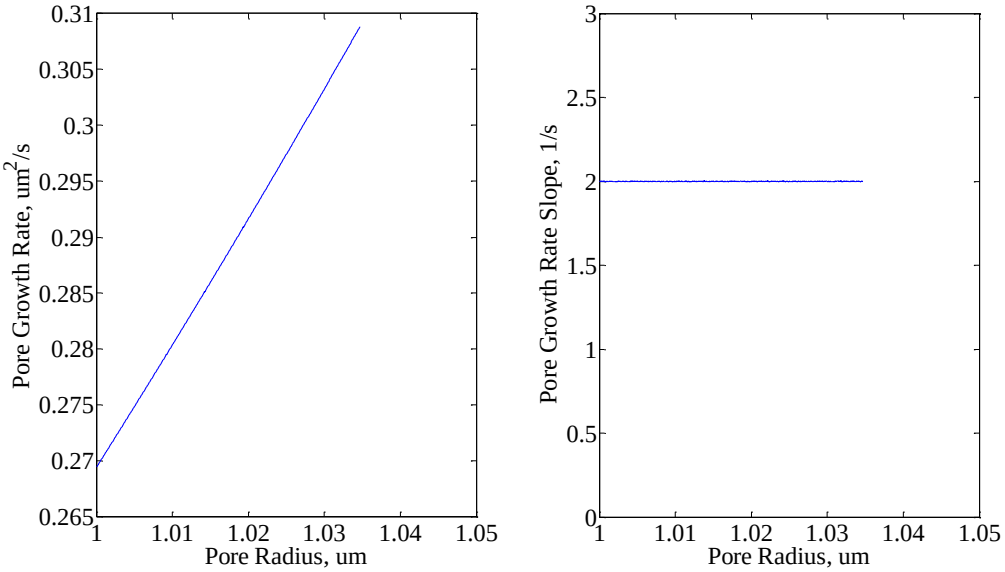

Fig. 2.6a Pore A_1 growth rate and its slope

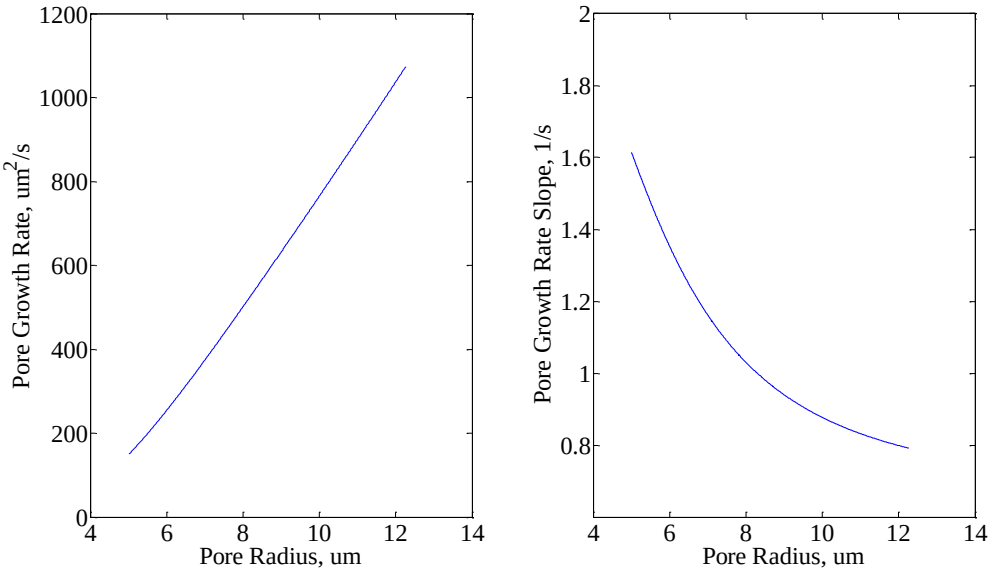

Fig. 2.6b Pore A_2 growth rate and its slope

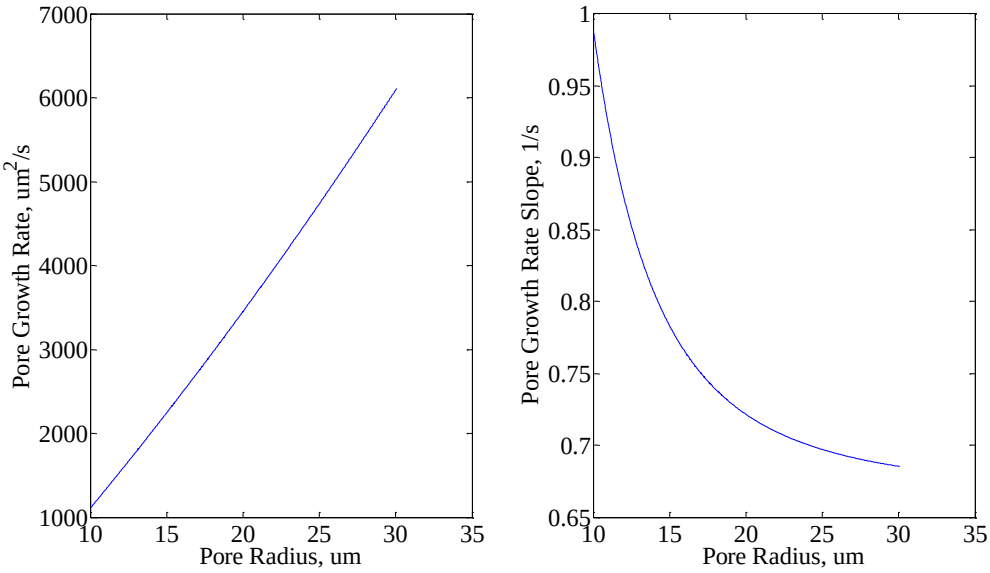

Fig. 2.6c Pore A_3 growth rate and its slope

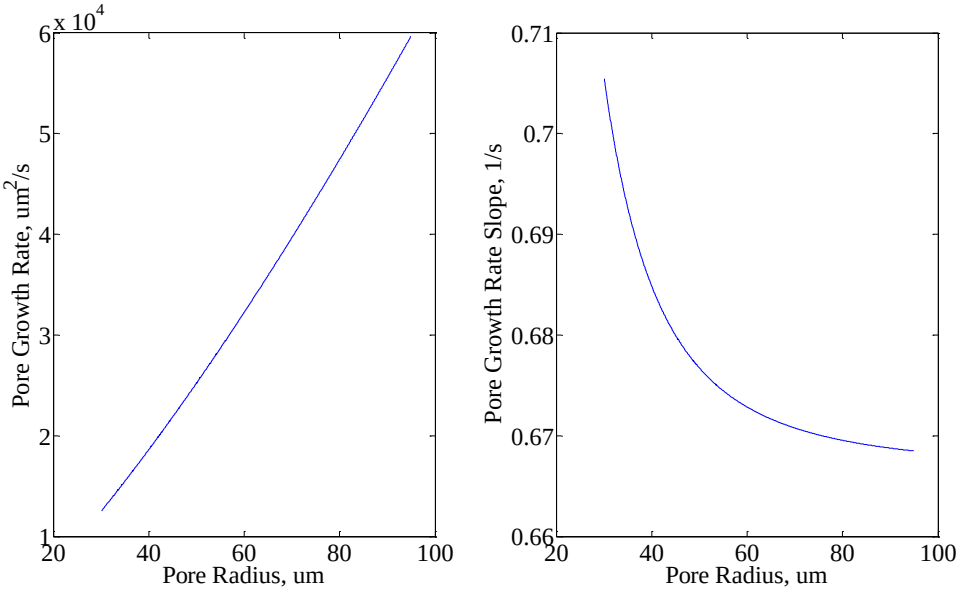

Fig. 2.6d Pore A_4 growth rate and its slope

Therefore for fast reactions, we can approximate the pore growth function as

$$\psi_{\text{fast-small}} = \frac{\varepsilon\chi A_p^2}{L_p} \tag{2-22}$$

$$\psi_{\text{fast-large}} = \frac{\varepsilon\chi A_p^2}{L_p}[1-(1-\frac{\kappa\Gamma_p L_p}{\varepsilon A_p^2})] = K\chi\Gamma_p = 1.2819(\frac{\varepsilon A_p}{r_p L_p})^{1/3} D^{2/3}\cdot\chi\cdot 2\sqrt{\pi}A_p^{1/2} \to A_p^{2/3} \tag{2-23}$$

In fact, for intermediate surface reaction kinetics, the pore growth function is similar to that for fast surface reaction. If written in a general form, we have the pore growth function below. The only difference is K is replaced by κ.

$$\psi_{\text{intermediate}} = \frac{\varepsilon\chi A_p^2}{L_p}[1-\exp(-\frac{\kappa\Gamma_p L_p}{\varepsilon A_p^2})] \tag{2-24}$$

$$\psi_{\text{intermediate-small}} = \frac{\varepsilon\chi A_p^2}{L_p} \tag{2-25}$$

$$\psi_{\text{intermediate-large}} = \kappa\chi\Gamma_p = \frac{4.544(\frac{\varepsilon A_p}{r_p L_p})^{1/3} D^{2/3} E_f C_0^{m-1}}{1.2819(\frac{\varepsilon A_p}{r_p L_p})^{1/3} D^{2/3} + E_f C_0^{m-1}}\chi A_p^{1/2} \tag{2-26}$$

In general, if the surface reaction is slow, both small pores and large pores grow based on $\psi\sim A^{1/2}$. If the surface reaction is intermediate to fast, small pores grow based on $\psi\sim A^2$ and large pores grow based on $\psi\sim A^{2/3}$. The forms of the pore growth functions for three different surface reaction rates are summarized in **Table 2.3**.

Table 2.3 Summary of pore growth functions

Slow surface reaction	small pore	$\psi = 2\sqrt{\pi} E_f C_0^{m-1} \chi A_p^{1/2}$
	large pore	$\psi = 2\sqrt{\pi} E_f C_0^{m-1} \chi A_p^{1/2}$
Intermediate surface reaction	small pore	$\psi = \frac{\varepsilon \chi A_p^2}{L_p}$
	large pore	$\psi = \frac{4.544(\frac{\varepsilon A_p}{r_p L_p})^{1/3} D^{2/3} E_f C_0^{m-1}}{1.2819(\frac{\varepsilon A_p}{r_p L_p})^{1/3} D^{2/3} + E_f C_0^{m-1}} \chi A_p^{1/2}$
Fast surface reaction	small pore	$\psi = \frac{\varepsilon \chi A_p^2}{L_p}$
	large pore	$\psi = 4.544(\frac{\varepsilon A_p}{r_p L_p})^{1/3} D^{2/3} \chi A_p^{1/2}$

Eq. 2-24, 2-25 and 2-26 are plotted in **Fig. 2.7**. While generating this plot, the magnitude of K and $E_f C_0^{m-1}$ are close, thus it is a mixed kinetics reaction (intermediate surface reaction). The input data are shown in **Table 2.4**.

Table 2.4 Input parameters for Eq. 2-24, 2-25 and 2-26

χ	0.082	volume $CaCO_3$ per volume 15 wt% HCl
L_p	300	μm
ε	1.00×10^{6}	$cm^{-1}s^{-1}$
$E_f C_0^{m-1}$	3.81×10^{-2}	cm/s
D	3.53×10^{-5}	cm^2/s

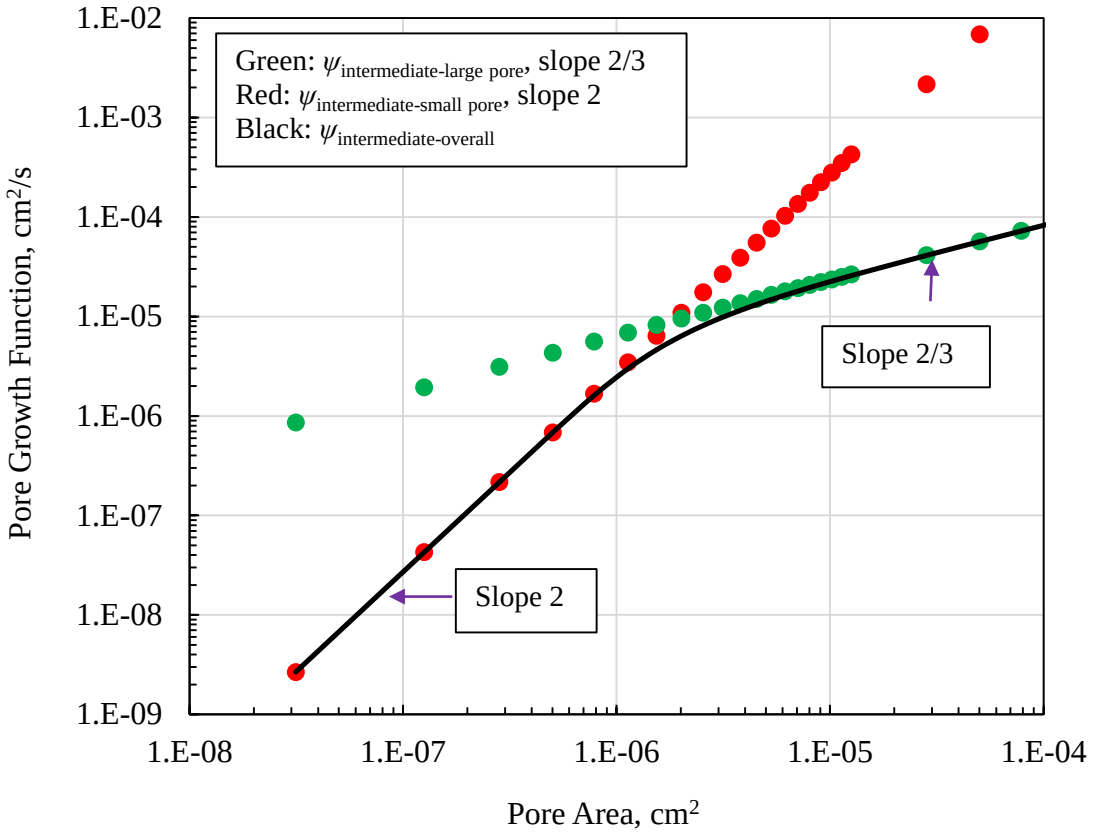

Fig. 2.7 Pore growth function for intermediate surface reaction

As indicated in Fig.2.7, pore growth rate increases with increasing pore area. A transition point exists that divides growth rate into two different regions, one with slope of 2 and the other one with slope of 2/3. Both slopes can make growth rate increase.

The analysis above shows that for slow surface reaction, the pore growth function is proportional to $A^{1/2}$; for intermediate to fast surface reaction, the pore growth function is proportional to $A^{2/3\sim2}$. However, it does not show which growth mechanism results in a

wormhole, nor best wormholing condition is discussed. The analysis below can help to determine which condition is most favorable for wormholing.

Wormholing occurs when larger pores tend to grow in cross-sectional area at a rate that greatly exceeds the growth rate of smaller pores (Schechter and Gidley, 1969). The rate of change of pore area A with time t can be written in the form

$$\frac{dA}{dt} = \alpha A^{1-n} \tag{2-27}$$

Analysis shows when n>0, smaller pores and larger pores tend to approach a same pore size ultimately. The dissolution is uniform and wormholes do not form. When n<0, larger pores grow much more rapidly than smaller pores, and wormhole forms.

In order to analyze the effect of n on pore growth rates, we choose three typical values of n as shown in Eq. 2-24, 2-25 and 2-26, and simulate the pore growth conditions. When n equals to 0.5, the pore growth rate is proportional to $A^{0.5}$. It corresponds to the pore growth function of slow surface reaction (Eq. 2-17). When n equals to 1/3, the pore growth rate is proportional to $A^{2/3}$. It corresponds to the pore growth function of larger pores with intermediate to fast surface reactions (Eq. 2-26 and Eq. 2-23). When n equals to -1, the pore growth rate is proportional to A^2. It corresponds to the pore growth function of smaller pores with intermediate to fast surface reactions (Eq. 2-25 and Eq. 2-22). The results are summarized In **Table 2.5** below. The simulation ends when the largest pore reaches 10 times its original area.

Table 2.5a. n=0.5 ($\psi \sim A^{1/2}$)

Initial pore area, μm^2	End pore area, μm^2	Increase times
900π	9000π	10
625π	8079π	13
100π	5606π	56.1
π	4335π	4335

Table 2.5b. n=1/3 ($\psi \sim A^{2/3}$)

Initial pore area, μm^2	End pore area, μm^2	Increase times
900π	9000π	10
625π	7641π	12.2
100π	3934π	39.3
π	1791π	1791

Table 2.5c. n=-1 ($\psi \sim A^2$)

Initial pore area, μm^2	End pore area, μm^2	Increase times
900π	9000π	10
625π	1670π	2.7
100π	111π	1.1
π	1.00π	1

In Table 2.5a, the pore growth function is proportional to $A^{1/2}$. When the largest pore reaches 10 times its original size due to acid/rock surface reaction, the smallest pore reaches 4335 times its original size. Smaller pores grow much faster than larger pores

relatively, and the sizes of the four pores are in the same order when the simulation finishes. We can see distinct growth difference from **Fig. 2.8a**. In this case, the dissolution is uniform and wormholes do not form.

In Table 2.5b, the pore growth function is proportional to $A^{2/3}$. When the largest pore reaches 10 times its original size, the smallest pore reaches 1791 times its original size, as plotted in **Fig. 2.8b**. Smaller pores also grow faster than larger pores. Compared with Table 2.5a, it shows the same trend. The only difference is smaller pores do not grow as fast as that in Table 2.5a.

In Table 2.5c, when the largest pore reaches 10 times its original size, the smallest pore size does not change. Larger pores grow much faster than smaller pores. When the simulation finishes, even the second largest pore grow only 2.7 times (as plotted in **Fig. 2.8c**), and the difference in pore areas among these four pores become significantly large. In this case, wormhole can form.

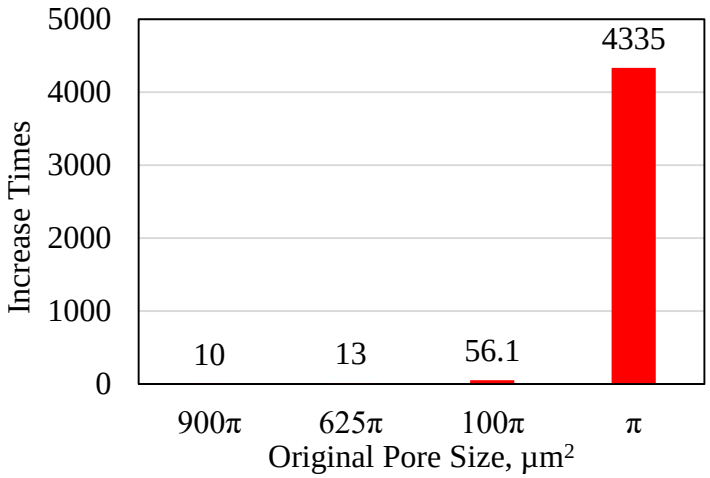

Fig. 2.8a Pore area increase times when n=0.5 ($\psi \sim A^{1/2}$)

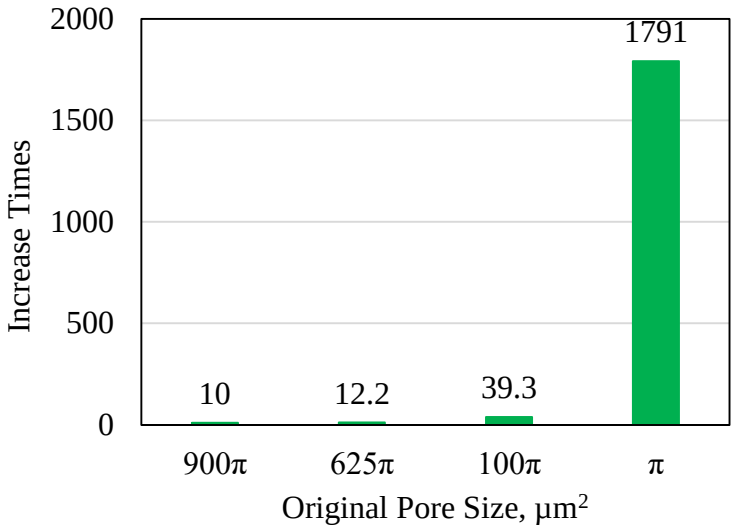

Fig. 2.8b Pore area increase times when n=1/3 ($\psi \sim A^{2/3}$)

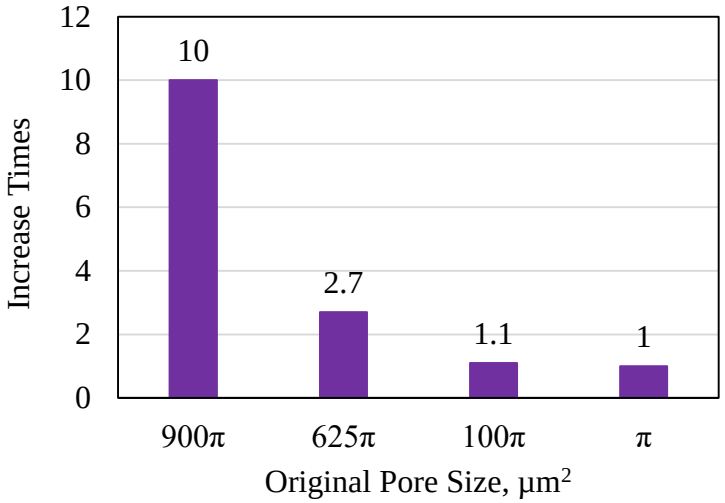

Fig. 2.8c Pore area increase times when n=-1 ($\psi \sim A^{2}$)

In fact, when -1<n<0, larger pores also grow faster than smaller pores. But it is not the most favorable condition compared with n=-1. Take the pore size 625π μm² for

example. When the largest pore reaches 10 times its initial size, the pores of size 625π μm^2 reaches 5.4 times, 3.4 times and 2.7 times of their initial sizes respectively for *n* equaling to -0.5, -0.8 and -1 (calculation results are shown in **Table 2.6**, and pore growth times are plotted in **Fig. 2.9**). We can see that *n* of -1 favors wormholing most because at this condition the largest pore grows fastest and other smaller pores grow slowest compared with other conditions.

Table 2.6a. n=-0.5 ($\psi \sim A^{1.5}$)

Initial pore area, μm^2	End pore area, μm^2	Increase times
900π	9000π	10
625π	3380π	5.4
100π	168π	1.7
π	1.00π	1

Table 2.6b. n=-0.8 ($\psi \sim A^{1.8}$)

Initial pore area, μm^2	End pore area, μm^2	Increase times
900π	9000π	10
625π	2156π	3.4
100π	122π	1.2
π	1.00π	1

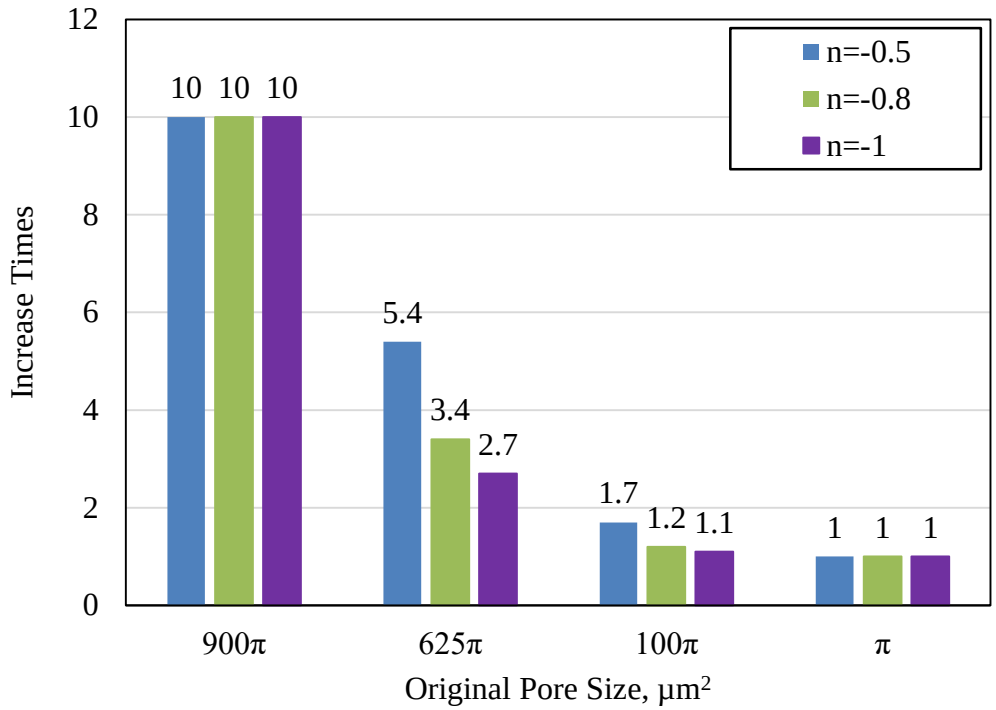

Fig. 2.9 Pore area increase times for n=-0.5, -0.8 and -1

2.2.3 Optimal Condition

Acid always tends to flow into larger pores on the surface due to their lower flow resistance. However, larger pores may not connect to another larger pore inside the rock, as can be seen from a set of Micro-CT images shown in **Fig. 2.10**. During wormhole propagation, such largest pore cannot always be expected at the wormhole tip. So in our model, we focus on the mode-size pore in a rock. It has the pore size with largest frequency on a pore size distribution curve. We call it mode pore size, denoted as $A_{p,mode}$. During wormhole propagation, wormhole tip is more likely to meet this pore size than any other pore sizes.

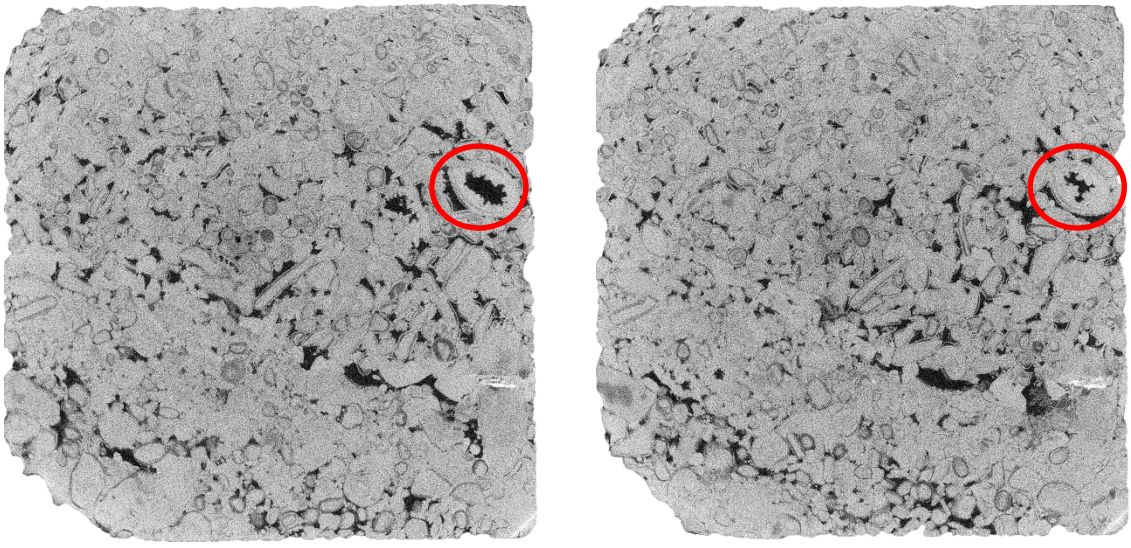

a. surface slice

b. 224 μm apart from a

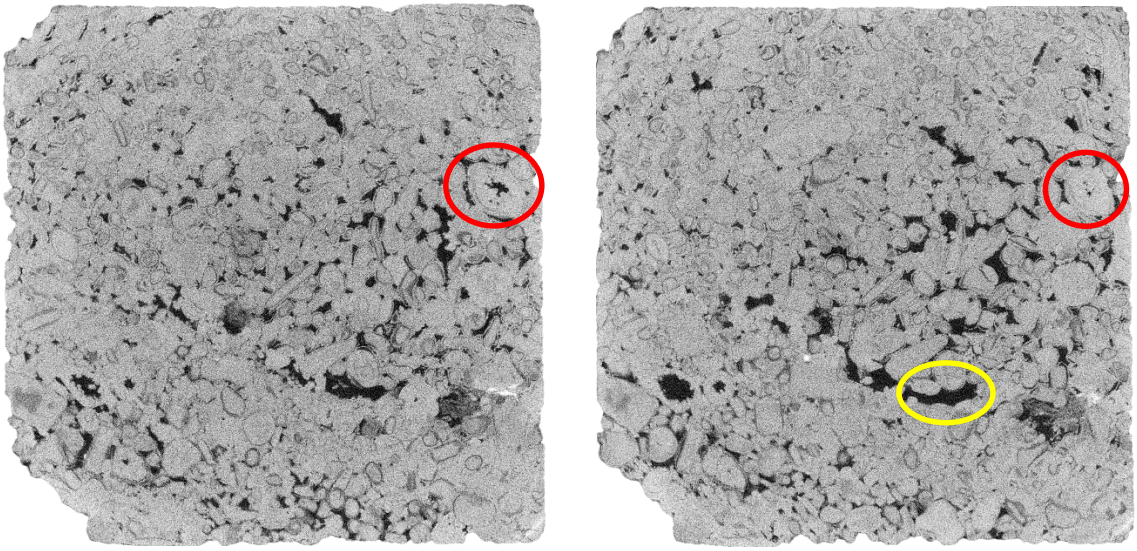

c. 232 μm apart from a

d. 480 μm apart from a

Fig. 2.10 Micro-CT slice images of Indiana limestone. The red circle in image (a) identifies the largest pore on the surface slice. The red circles in images (b), (c) and (d) show that the largest pore becomes smaller as it goes into the rock, and is not connected to the largest pore on another slice, which is identified by the yellow circle.

At each particular time and position, it is more likely that larger amounts of acid flows into the mode-size pores. In order to get the optimal condition, we need to make this mode-size pore grow much faster than other pores at the wormhole tip. As has been discussed, when pores grow based on $\psi \sim A^2$, the most favorable wormholing condition can be achieved. Therefore, the acid flow rate needs to be controlled to a particular value so that the mode-size pore grows based on $\psi \sim A^2$. Being such, all other smaller pores at this position also grow based on $\psi \sim A^2$ according to Fig. 2.7. But this mode-size pore grows significantly faster than other smaller pores, as discussed with the simulation results in Table 2.5c.

If acid flow rate is larger than this optimal rate, the mode-size pore and some portion of smaller pores at this position grow based on $\psi \sim A^{2/3}$. As discussed with the simulation results in Table 2.5b, these smaller pores are trying to get a same ultimate size as the mode-size pore does. This can finally become uniform dissolution in extreme cases.

In order to have this mode-size pore grow based on $\psi \sim A^2$, we need to set its area to be the transition area shown in Fig. 2.7. Note that the mode pore size is naturally existing in a particular rock which is a fixed value, but the transition pore size depends on the acid flow rate and it can be changed. **Fig. 2.11** below shows four different transition pore sizes at four different acid flow rates. The flow coefficient ε in Eq. 2-24, 2-25 and 2-26 are 10^8, 10^7, 10^6, 10^5 $cm^{-1}s^{-1}$ respectively for Fig. 2.11a, Fig. 2.11b, Fig. 2.11c and Fig. 2.11d, which mean the pressure gradient for these flows are decreasing. The transition pore areas are 12, 40, 180, 1000 μm^2 respectively.

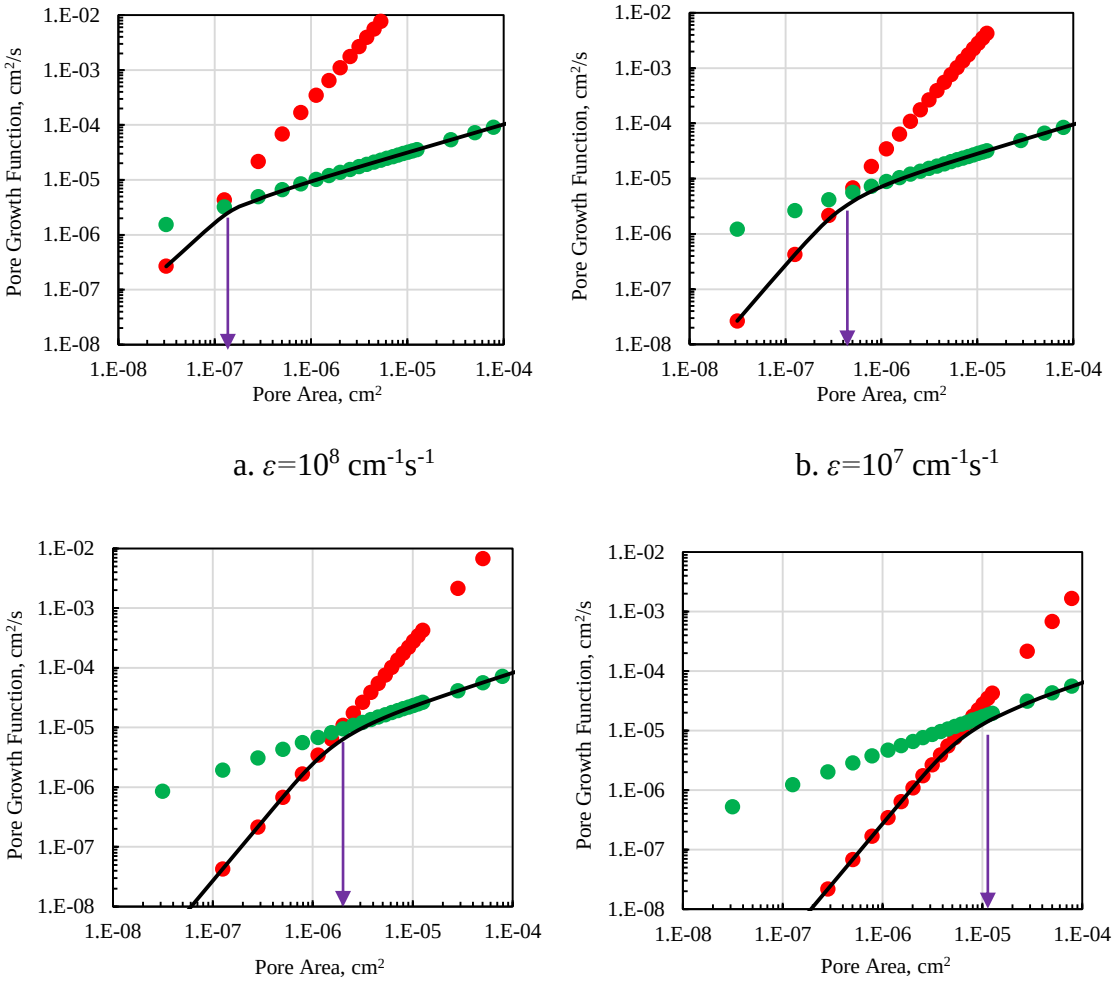

a. ε=10^8 $cm^{-1}s^{-1}$ b. ε=10^7 $cm^{-1}s^{-1}$

c. ε=10^6 $cm^{-1}s^{-1}$ d. ε=10^5 $cm^{-1}s^{-1}$

Fig. 2.11 Change of transition pore sizes with different acid flow velocities

Therefore, we can control the transition pore size by adjusting the acid flow rate. Specially, we can make the transition pore size equal to the mode pore size. We can substitute $A_{p,mode}$ into Eq. 2-25 and 2-26.

$$\psi_{intermediate-small} = \frac{\varepsilon \chi A_{p,mode}^2}{L_{p,mode}} = \frac{\chi A_{p,mode} \bar{v}_{p,mode}}{L_{p,mode}} \quad (2\text{-}28)$$

$$\psi_{\text{intermediate–large}} = \kappa\chi\Gamma_{p,\text{mode}} \tag{2-29}$$

At the transition point, $\Psi_{\text{small}}=\Psi_{\text{large}}$.

$$\frac{\chi A_{p,\text{mode}}\bar{v}_{p,\text{mode}}}{L_{p,\text{mode}}} = \kappa\chi\Gamma_{p,\text{mode}} \tag{2-30}$$

After arrangements, we can get the acid velocity in the mode-size pore.

$$\bar{v}_{p,\text{mode}} = \frac{\kappa\Gamma_{p,\text{mode}}L_{p,\text{mode}}}{A_{p,\text{mode}}} \tag{2-31}$$

The average acid velocity in the mode-size pore calculated through Eq. 2-31 is just large enough to make all the pores grow based on $\psi\sim A^2$ at a random position of a rock. This mode-size pore grows much faster than other smaller pores, like the case shown in Table 2.5c and Fig. 2.8c. This is the most favorable condition for wormholing, and is the optimal condition. Therefore, we can further write Eq. 2-31 into Eq. 2-32.

$$\bar{v}_{p,\text{mode},opt} = \frac{\kappa\Gamma_{p,\text{mode}}L_{p,\text{mode}}}{A_{p,\text{mode}}} \tag{2-32}$$

Note that with this optimal velocity in the mode-size pore, the ratio between the acid consumption rate and acid flow rate is 1, as shown by Eq. 2-33. It is another form of Eq. 2-32, with the numerator and denominator multiplied by C_0. The numerator denotes how much acid is reacted in gmole/s. The denominator denotes how much acid flows through the pore in gmole/s. With the ratio of 1, acid is just enough to enlarge the pore and no acid is wasted.

$$\frac{\kappa\Gamma_{p,\text{mode}}L_{p,\text{mode}}C_0}{A_{p,\text{mode}}\bar{v}_{p,\text{mode},opt}C_0} = 1 \tag{2-33}$$

The Damkohler number can describe Eq. 2-33. It is the ratio between reaction rate and convection rate. With C_0 reduced in Eq. 2-33, we have

$$Da = \frac{\kappa \Gamma_{p,\text{mode}} L_{p,\text{mode}}}{A_{p,\text{mode}} \bar{v}_{p,\text{mode},opt}} = 1 \tag{2-34}$$

2.3 Wormhole Tip Interstitial Velocity

Section 2.2 described the optimal acid velocity in the mode-size pore. In order to get the optimal acid injection rate for a particular rock, this velocity needs to be upscaled to the velocity at the wormhole tip. This section introduces a porous medium model with its properties represented by a pore size density function. The method for upscaling is presented.

2.3.1 Porous Medium Model

The porous medium model used in this study was first presented by Schechter and Gidley (1969). In this porous medium model, pores are described as randomly distributed capillaries in the rock, with an average pore length $\bar{L}_p$. Fluid can flow from one pore to another with a certain pressure drop. The sketch description of this model is shown in **Fig. 2.12**.

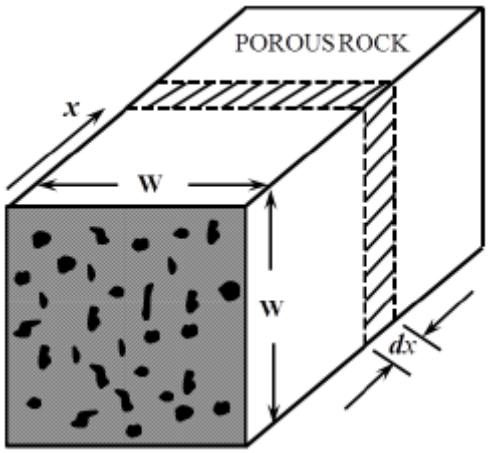

Fig. 2.12 Porous medium model (Schechter and Gidley, 1969)

From acidizing point of view, one of the most important properties to differentiate carbonate rocks is the pore size distribution. In this model, a pore size density function $\eta(A)$ is defined so that $\eta(A)\cdot V\cdot dA$ is the number of pores having an area between A and $A+dA$ with an average pore length $\bar{L}_p$ in the volume V. For example, if attention is focused on a certain group of pores, having an area between A_1 and A_2, then the number of pores in the group is

$$N_p = \int_{A_1}^{A_2} w^2 \Delta x \eta(A) dA \tag{2-35}$$

where w^2 is the flow area of the porous medium shown in Fig. 2.12.

An intuitive method to understand the pore size density function is through a histogram, as shown in **Fig. 2.13**. For example, the number of pores having a pore radius between 25 μm to 30 μm (pore area between 625π μm^2 and 900π μm^2) in a unit volume is

denoted by the green bin area. Note that when calculating this bin area, the pore radius should be converted to pore area.

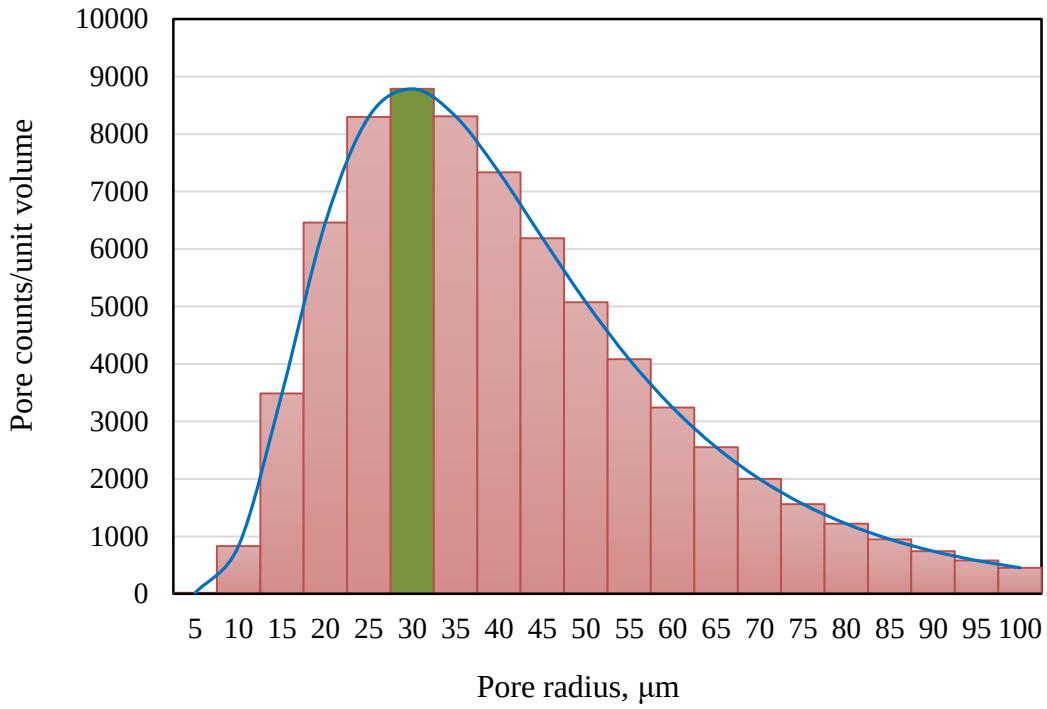

Fig. 2.13 Pore size density function and its histogram representation

Based on the pore size density function, porosity is the summation of each pore volume in a unit porous medium volume, and is described by Eq. 2-36.

$$\phi = \bar{L}_p \int_0^\infty A\eta(A)dA \tag{2-36}$$

The volumetric flow rate can be calculated by summing the volume flowing through each pore across the flow area w^2. It is shown by Eq. 2-37 as below (Schechter and Gidley, 1969).

$$q = \int_0^\infty \bar{v}_p A \bar{L}_p w^2 \eta(A) dA = \bar{L}_p w^2 \int_0^\infty \bar{v}_p A \eta(A) dA \tag{2-37}$$

In Eq. 2-37, $\int_0^\infty \bar{L}_p w^2 \eta(A) dA$ denotes the number of pores in the volume $\bar{L}_p w^2$. The flow rate in each single pore is $\bar{v}_p A$. So the total flow rate is the multiplication of the two terms.

The Poiseuille's law in Eq. 2-20 can be specifically written for the mode-size pore, as described by Eq. 2-38.

$$\bar{v}_{p,\text{mode}} = \varepsilon A_{p,\text{mode}} \tag{2-38}$$

The coefficient ε is a constant for every pore, and can be calculated below

$$\varepsilon = \frac{\bar{v}_{p,\text{mode}}}{A_{p,\text{mode}}} \tag{2-39}$$

Substituting Eq. 2-20 and 2-39 into Eq. 2-37, the flow rate through the porous medium can be written as

$$q = \frac{\bar{v}_{p,\text{mode}}}{A_{p,\text{mode}}} \bar{L}_p w^2 \int_0^\infty A^2 \eta(A) dA \tag{2-40}$$

The integrals of the pore size density function represents important properties of the porous medium. If we define the i th integral of the pore size density function as moments of the function, as shown in Eq. 2-41,

$$M_i = \int_0^\infty A^i \eta(A) dA \tag{2-41}$$

then we can get

$$M_0 = \int_0^\infty \eta(A) dA \tag{2-42}$$

$$M_1 = \int_0^\infty A\eta(A)dA \tag{2-43}$$

$$M_2 = \int_0^\infty A^2\eta(A)dA \tag{2-44}$$

M_0 represents the number of pores in a unit porous medium volume. M_1 is related to porosity of the porous medium and M_2 is related to its flow properties as shown in the following two relationships (from Eq. 2-36 and Eq. 2-40).

$$\phi = \bar{L}_p M_1 \tag{2-45}$$

$$q = \frac{\bar{v}_{p,\text{mode}}}{A_{p,\text{mode}}} \bar{L}_p w^2 M_2 \tag{2-46}$$

We can see once the pore size density function $\eta(A)$ is determined, the flow rate can be calculated through moment equations.

2.3.2 Pore Size Distribution

Experimental methods are needed to determine rock pore size distribution. Common methods include High Pressure Mercury Injection (HPMI) method, Nuclear Magnetic Resonance (NMR) method, and Micro-CT Scan method. In this section, we used Micro-CT Scanner to determine pore size distribution. The scanner model is Phoenix nanotom, and is shown in **Fig. 2.14**.

Fig. 2.14 Micro-CT scanner

Micro-CT Scanner utilizes the X-ray attenuation principle. Different CT numbers represent different densities inside the sample. The pore space has smaller density thus a smaller CT number, and the rock matrix has larger density thus a larger CT number. This can be used to distinguish the pore and solid.

Our sample is a cube with 1 cm side length. During scanning, images are sliced into squares with 1 cm side length and 8 μm thickness. On each slice, pores and solid can be identified by different CT numbers. We can import the data set produced by Micro-CT Scanner to an image analysis software (ImageJ is used in this study). ImageJ can help to count pores pixel by pixel and produce the pore area. Pixels with small CT numbers are counted as pores and pixels with large CT numbers are counted as solid. An example of the analysis results by ImageJ is illustrated in **Table 2.7** below. The sample is Indiana limestone with 6 mD.

Table 2.7 Example of analysis results produced by ImageJ

File	Pore #	Area (μm^2)
Indiana	1	1151.982
Indiana	2	895.986
Indiana	3	1087.983
Indiana	4	8447.865
Indiana	5	5823.907
Indiana	6	2943.953
⋮	⋮	⋮
Indiana	N	…

Our data show that the pore size distribution in each slice is close to the lognormal distribution. We can write η in the following form.

$$\eta(A) = \frac{N}{A\sigma\sqrt{2\pi}} \exp[-\frac{(\ln A - \mu)^2}{2\sigma^2}] \tag{2-47}$$

where μ is the mean value of ln(A), σ^2 is the variance of ln(A) and N is a multiplier. We can determine μ and σ^2 directly from the measurement. For this Indiana limestone sample, μ equals to -9.2, and σ^2 equals to 1.3. The mode of the lognormal distribution is calculated through Eq. 2-47.

$$Mode = \exp(\mu - \sigma^2) \tag{2-48}$$

Substituting μ and σ^2 into Eq. 2-48, we can get the mode pore area as 2.75×10^{-5} cm^2, and the mode pore radius is then calculated as 30 μm.

The moments of Eq. 2-47 can be calculated by substituting Eq. 2-47 into Eq. 2-42, 2-43 and 2-44 respectively.

$$M_0 = \int_0^\infty \frac{N}{A\sigma\sqrt{2\pi}} \exp[-\frac{(\ln A - \mu)^2}{2\sigma^2}]dA = N \tag{2-49}$$

$$M_1 = \int_0^\infty A \cdot \frac{N}{A\sigma\sqrt{2\pi}} \exp[-\frac{(\ln A - \mu)^2}{2\sigma^2}]dA = N \exp(\mu + \frac{\sigma^2}{2}) \tag{2-50}$$

$$M_2 = \int_0^\infty A^2 \cdot \frac{N}{A\sigma\sqrt{2\pi}} \exp[-\frac{(\ln A - \mu)^2}{2\sigma^2}]dA = N \exp[2(\mu + \sigma^2)] \tag{2-51}$$

The multiplier N is determined from Eq. 2-45. The parameters involved for this calculation is shown in **Table 2.8** below.

Table 2.8 Indiana limestone pore parameters

Mean value of ln(A), μ	-9.2
Variance of ln(A), σ^2	1.3
Porosity	15%
Average pore length, $\bar{L}_p$	300 μm

From Eq. 2-45, we can calculate M_1.

$$M_1 = \frac{\phi}{\bar{L}_p} = \frac{15\%}{300\mu\text{m}} = \frac{15\%}{0.03\text{cm}} = 5\text{cm}^{-1} \tag{2-52}$$

Substituting μ and σ^2 into Eq. 2-50, we can get Eq. 2-53.

$$M_1 = N \exp(\mu + \frac{\sigma^2}{2}) = N \exp(-9.2 + \frac{1.3}{2}) = 1.935 \times 10^{-4} N \tag{2-53}$$

By equaling Eq. 2-52 and Eq. 2-53, we can calculate the multiplier N=25834. Note that in Eq. 2-49, M_0 represents the number of pores per unit volume, which is calculated to be N. Therefore, the multiplier N can be treated as the number of pores per unit volume. Substituting μ, σ^2 and N into Eq. 2-47, we can get the pore size distribution shown with eq. 2-54. It is plotted as shown in **Fig. 2.15**.

$$\eta(A) = \frac{25834}{1.14\sqrt{2\pi}A}\exp[-\frac{1}{2.6}(\ln A + 9.2)^2] \tag{2-54}$$

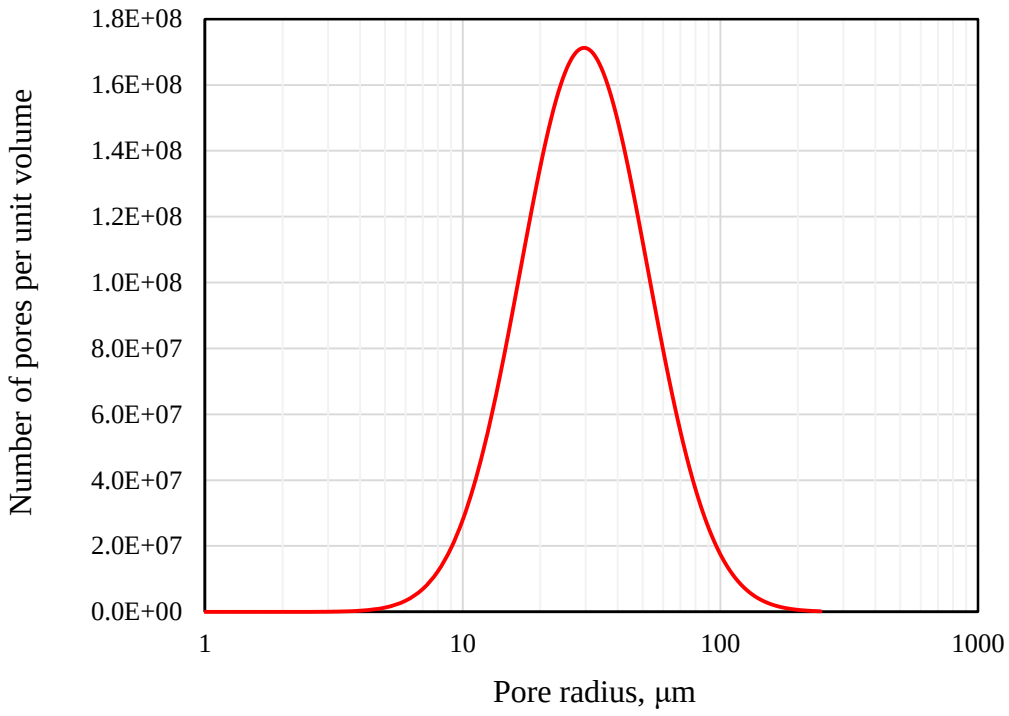

Fig. 2.15 Indiana limestone pore size distribution

2.3.3 Upscaling

In section 2.2, we have obtained the optimal acid velocity in the mode-size pore ($\bar{v}_{p,\mathrm{mode},opt}$). With this velocity, this particular pore grows much faster than other smaller pores and best wormholing condition is achieved. In order to get the optimal injection rate of the whole core, we need to correlate $\bar{v}_{p,\mathrm{mode},opt}$ to the flow rate in the porous medium.

Acid interstitial velocity at the tip of a dominant wormhole governs the wormhole propagation (Hung et al. 1989). This relationship is described by Eq. 2-55. In order to have the optimal wormhole propagation, an optimal interstitial velocity at the dominant wormhole tip $v_{i,tip,opt}$ needs to be maintained. Therefore, we need to consider correlating $\bar{v}_{p,\mathrm{mode},opt}$ to the flow rate at the wormhole tip region.

$$v_{wh} = \frac{dx}{dt} = v_{i,tip}\left(\frac{C_{tip}}{C_0}\right)N_{ac} \tag{2-55}$$

The red circle in **Fig. 2.16** shows the wormhole tip region to be investigated. It is a linear acidizing coreflood experiment with a dominant wormhole propagating.

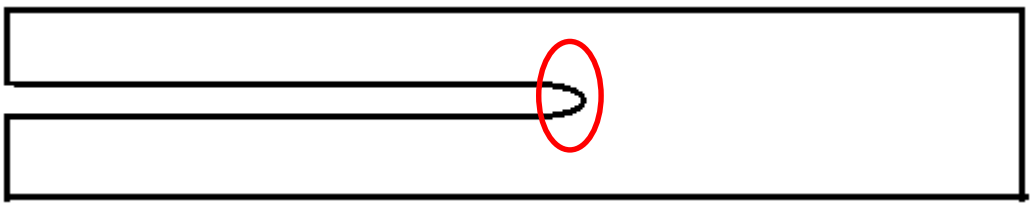

Fig. 2.16 Wormhole tip region during an acidizing coreflood experiment

Eq. 2-46 provides a general method to calculate flow rates based on our porous medium model. If w^2 is taken as the flow area at the wormhole tip, we can calculate the tip acid flow rate with Eq. 2-56 below. Acid interstitial velocity at the wormhole tip is then calculated as Eq. 2-57.

$$q_{tip} = \frac{\bar{v}_{p,\text{mode}}}{A_{p,\text{mode}}} \bar{L}_p A_{tip} M_2 \tag{2-56}$$

$$v_{i,tip} = \frac{q_{tip}}{A_{tip}\phi} = \frac{\bar{v}_{p,\text{mode}}}{A_{p,\text{mode}}} \cdot \frac{\bar{L}_p M_2}{\phi} \tag{2-57}$$

If we use the optimal acid velocity in the mode-size pore, the optimal wormhole tip interstitial velocity can be obtained as Eq. 2-58.

$$v_{i,tip,opt} = \frac{\bar{v}_{p,\text{mode},opt}}{A_{p,\text{mode}}} \cdot \frac{\bar{L}_p M_2}{\phi} \tag{2-58}$$

As can be seen, $v_{i,tip,opt}$ solely depends on the rock porosity, pore size distribution and acid/rock reaction. Flow geometry does not affect it. Therefore, it can be treated as the basis to select acid for a particular carbonate rock. And also, it is our starting point to upscale lab results to field.

Once the optimal tip interstitial velocity is known, the optimal acid injection rate can be obtained for different flow geometries. Take linear acidizing coreflood experiment for example. Furui et al. (2010) developed a linear flow correlation between core interstitial velocity and wormhole tip interstitial velocity, as shown in Eq. 2-59, together with breakthrough pore volume calculation (Eq.2-60).

$$v_i = \frac{d_{wh}}{d_{core}} v_{i,tip} \tag{2-59}$$

$$PV_{bt} = \frac{d_{wh}}{d_{core}} N_{ac} \tag{2-60}$$

In order to use this correlation, wormhole diameter is needed. The following section shows how to calculate wormhole diameter based on the fluid loss, and then get the optimal acid injection rate for linear acidizing coreflood experiments.

2.4 Fluid Loss and Wormhole Diameter

Fluid loss has an important effect on wormhole growth. For a given flow rate, the more acid that is lost through the wormhole walls, the less acid reaches the wormhole tip. During the "loss" process, acid enlarges the wormhole radially and eventually wormhole reaches a certain diameter until it breaks through the core.

2.4.1 Flow Correlation and Fluid Loss Profile

It is difficult to measure the amount of fluid loss during an experiment. However, it can be studied through numerical simulation. In this work, a 3D FEM model is set up to simulate linear acidizing coreflood experiments. **Fig. 2.17a** shows an example of the simulation domain. The core is 1.5-in. diameter by 8-in. long. A wormhole is represented by a tube at the center of the core and its tip is represented by a hemisphere (blue part). A 1000 psi backpressure is applied on the core outlet surface. No flow boundary condition is applied on the core wall. The wormhole wall and core inlet surface is treated as inlet in this simulation domain (**Fig. 2.17b**). A constant inlet pressure is applied. The flow rate is calculated through the velocity on the outlet surface. Not like a dynamic acidizing

coreflood experiment, this FEM model simulates the pressure and velocity field at a particular time when the wormhole reaches a particular location. From this point of view, it is static.

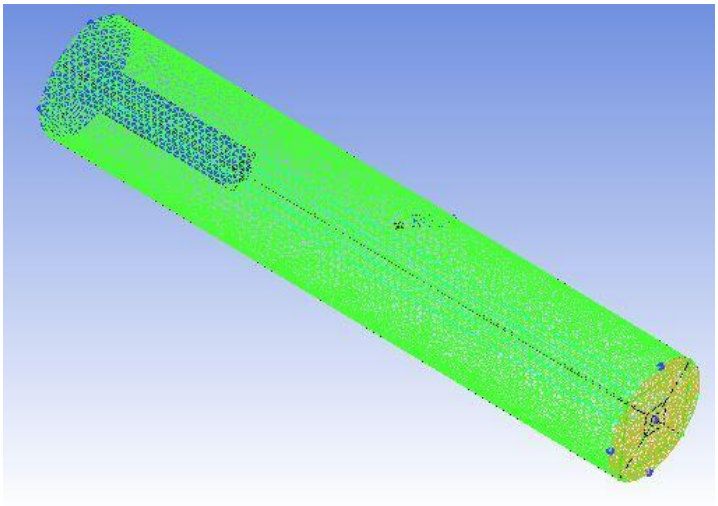

Fig. 2.17a Simulation domain

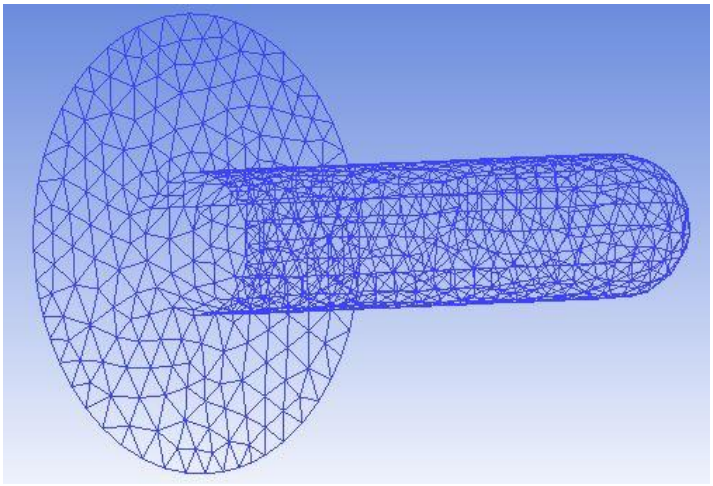

Fig. 2.17b Inlet boundary

There are two purposes for setting up this numerical model. The first one is to verify Eq. 2-59. The simulation study is carried out with the same core diameter but different wormhole diameters, which is supplemental to the previous study of the same wormhole diameter but different core diameters. The second purpose is to study the fluid loss profile along the dominant wormhole.

At a same injection rate, three sets of simulations are run with three different wormhole diameters, 6 mm, 8 mm and 12 mm. Each set of simulations includes 7 runs with 7 different wormhole lengths. The simulation results are shown in **Fig. 2.18**. As can be seen from the simulation results, the $v_{i,tip}$ in 6 mm wormhole diameter case is 4/3 times the 8 mm wormhole diameter case, and is 2 times that of the 12 mm wormhole diameter case. The $v_{i,tip}$ in 8 mm wormhole diameter case is 1.5 times the 12 mm wormhole diameter case. Therefore, further simulation results with the same core diameter but different wormhole diameters prove the validity of Eq. 2-59. It is used to upscale $v_{i,tip,opt}$ to $v_{i,opt}$.

The simulation results also show that when the wormhole penetration length reaches the value of the core diameter, the $v_{i,tip}$ remains constant until wormhole breakthrough. In other words, the amount of acid loss and the acid flow rate at the wormhole tip keep constant after this point. It is explained below.

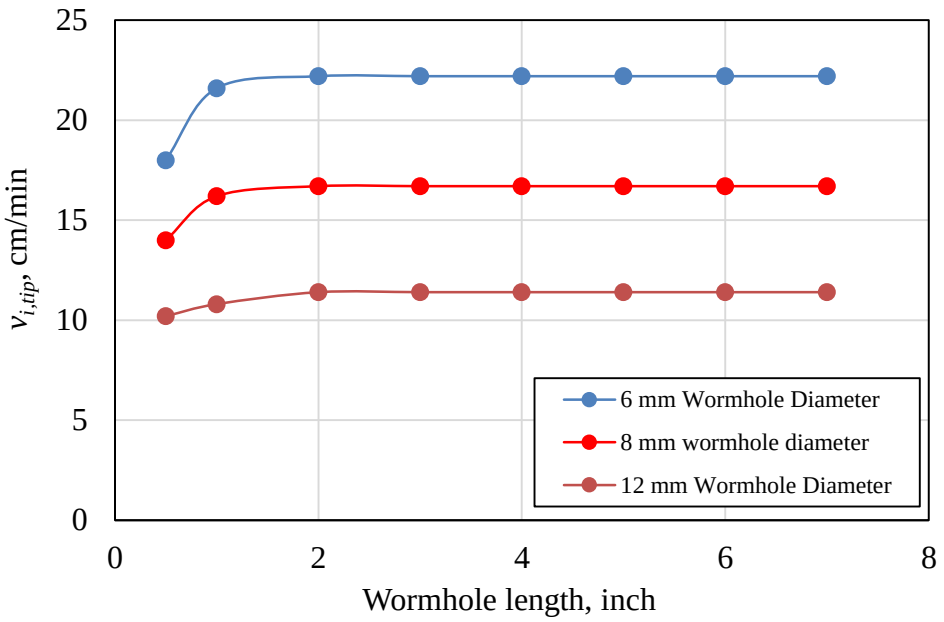

Fig. 2.18 Effect of wormhole diameter on $v_{i,tip}$

When the wormhole length is less than the core diameter, the spherical flow around the wormhole tip is not fully established, and there is still flow through the core surface, as can be seen from **Fig. 2.19**. It shows the velocity field on the inlet surface of a 0.5 inch long wormhole. The red color represents higher velocity and the blue color represents lower velocity.

Once the wormhole has penetrated beyond this length, the spherical flow around the wormhole tip is fully established, and there is no flow through the core surface. It can be seen from **Fig. 2.20**. It shows the velocity field on the inlet surface of a 5 inches long wormhole. The red color represents higher velocity and the blue color represents lower velocity. The pressure difference between the wormhole and surrounding porous medium

is balanced except the tip region. So there is a moving front of injection pressure and velocity. This can be seen in **Fig. 2.21**, which shows the pressure field during wormhole propagation. It further proves that in order to get the optimal condition, the optimal wormhole tip interstitial velocity needs to be maintained.

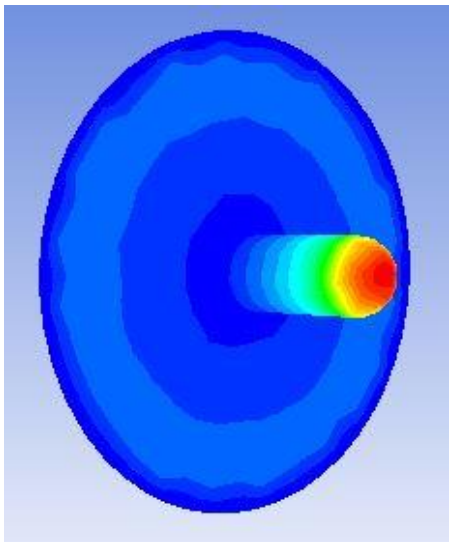

Fig. 2.19 Velocity field on the inlet surface of a 0.5 inch long wormhole

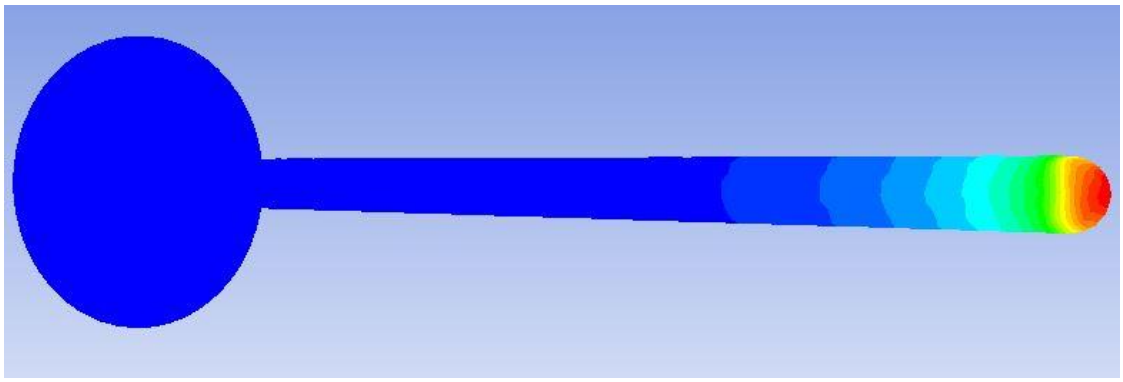

Fig. 2.20 Velocity field on the inlet surface of a 5 inches long wormhole

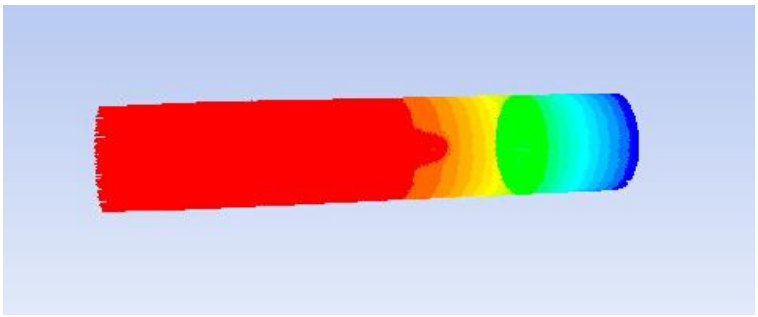

Fig. 2.21 Pressure profile of a core with a 5 inches long wormhole

From the simulated velocity field, the fluid loss profile along wormhole can be obtained, as shown in **Fig. 2.22**.

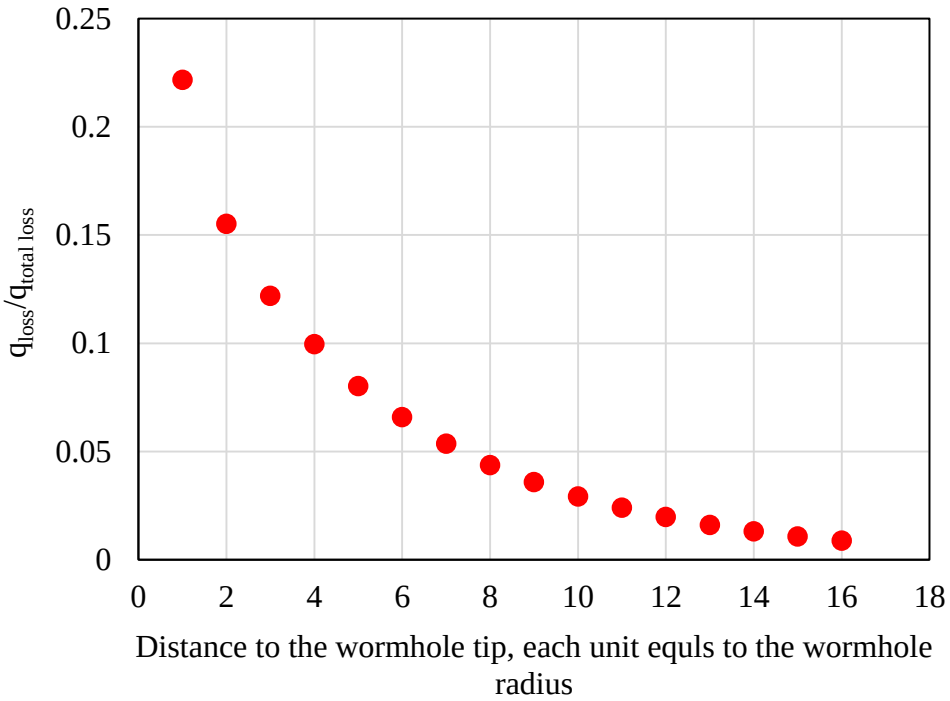

Fig. 2.22 Fluid loss profile along the dominant wormhole

As indicated in this figure, most of the fluid loss occurs near the wormhole tip. If we look at the first seven sections from the wormhole tip (each section length equals to the wormhole radius), about 95% of fluid loss happens in these sections.

2.4.2 Wormhole Diameter Calculation

Wormhole tip propagation velocity can be calculated through Hung's model with Eq. 2-55. Analogously, the growth rate of wormhole radius can be derived in a similar way. The amount of rock dissolved dm_r in the radial direction and the amount of acid consumed dm_a correspondingly can be written as Eq. 2-61 and Eq. 2-62.

$$dm_r = A_{wall}(1-\phi)\rho_r dr \tag{2-61}$$

$$dm_a = v_{i,loss}A_{wall}\phi\rho_a C_{wall}dt \tag{2-62}$$

where A_{wall} is the wormhole wall area of a certain length, $v_{i,loss}$ is the acid interstitial velocity through the wormhole wall, ρ_r is the rock density, ρ_a is the acid density, dr is the infinitesimal radial distance and dt is the corresponding time interval.

The acid gravimetric dissolving power β is defined as the mass of rock dissolved per mass of acid, as shown in Eq. 2-63. The wormhole radius growth rate $v_{wh\text{-}radial}$ can then be calculated with Eq. 2-64.

$$\beta = \frac{dm_r}{dm_a} = \frac{A_{wall}(1-\phi)\rho_r dr}{v_{i,loss}A_{wall}\phi\rho_a C_{wall}dt} \tag{2-63}$$

$$v_{wh-radial} = \frac{dr}{dt} = v_{i,loss}\frac{\beta\phi\rho_a C_{wall}}{(1-\phi)\rho_r} = v_{i,loss}(\frac{C_{wall}}{C_0})N_{ac} \tag{2-64}$$

The interstitial velocity of fluid loss can be calculated by Eq. 2-65, where q_{loss} is fluid loss rate per unit wormhole length. Substituting Eq. 2-65 into Eq. 2-64 and integrate, we can get Eq. 2-66.

$$v_{i,loss} = \frac{q_{loss}}{2\pi r_{wh}} \tag{2-65}$$

$$r_{wh}^2 - r_p^2 = \frac{q_{loss}}{\phi\pi}\left(\frac{C_{wall}}{C_0}\right)N_{ac}t \tag{2-66}$$

where r_p is the pore radius and t is the time for wormhole growth in radial direction. The fluid loss rate can be calculated through Darcy's law

$$q_{loss} = \frac{2\pi k\Delta p}{\mu \ln\left(\frac{r_{core}}{r_p}\right)} \tag{2-67}$$

where k is the rock permeability, μ is the acid viscosity, r_{core} is the core radius, and Δp is the pressure difference between core outer boundary and the wormhole.

Time t in Eq. 2-66 is calculated from fluid loss profile in Fig. 2.18. Here it is assumed that the first 95% fluid loss flux (in the distance of $7r_{wh}$ from the wormhole tip) can enlarge the wormhole radius while the rest 5% fluid loss does not due to low acid interstitial velocity. So for a particular place along the wormhole, the time of its enlargement is calculated below

$$t = \frac{7r_{wh}}{v_{wh}} = \frac{7r_{wh}}{v_{i,tip}N_{ac}} \tag{2-68}$$

Substituting Eq. 2-68, 2-67 into Eq. 2-66, the wormhole diameter can be calculated. A calculation example is shown in Section 2.5.

2.5 Optimal Condition Calculation

Based on the model developed above, we can see that once the rock porosity and pore size distribution are determined, the optimal acid injection rate of a particular acid can be calculated for linear acidizing coreflood experiments. This section shows an example of the optimal condition calculation.

2.5.1 Model Framework

A flow chart of this method is shown in **Fig. 2.23** below.

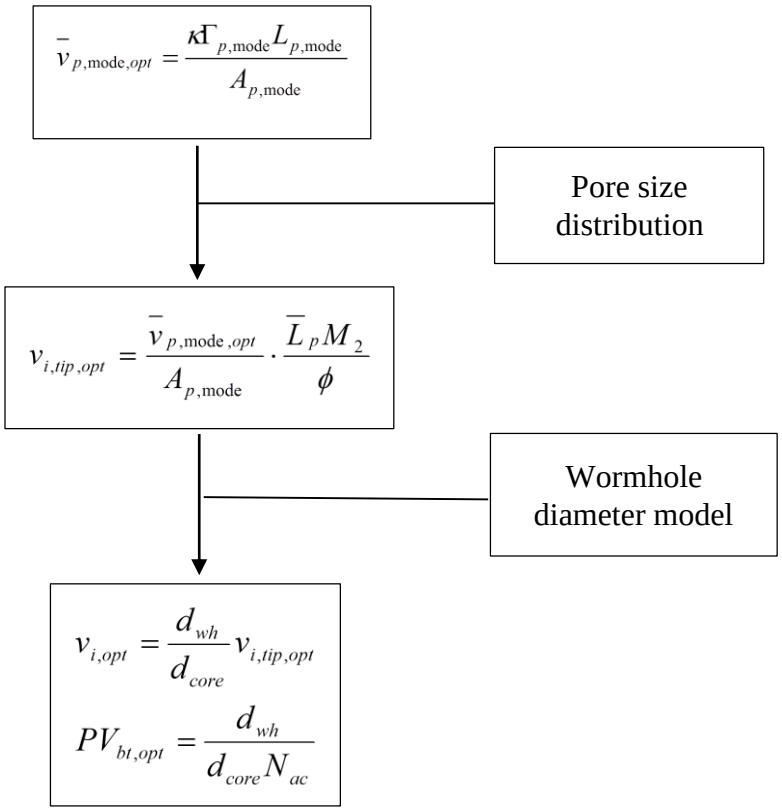

Fig. 2.23 Model calculation framework

One of the advantages of this model is that no cores are needed in order to use this model. The mode-size pore, pore size distribution and porosity can be measured using Micro-CT Scanner. The sample can be small pieces of rock with any shapes, like pieces from drill cuttings.

The following sequence describes how to use this model.

1. Collect rock samples. Samples can be drill cuttings of the pay zone.
2. Obtain pore size distribution from a Micro-CT Scanner. Identify the pore size that has largest frequency (mode-size pore).
3. Calculate the optimal average acid velocity in the mode-size pore $\bar{v}_{p,\mathrm{mode},opt}$.
4. Calculate M_2 function from the pore size density function.
5. Upscale acid velocity in the mode-size pore to the acid interstitial velocity at the wormhole tip $v_{i,tip,opt}$.
6. Calculate wormhole diameter.
7. Calculate the optimal acid injection rate and optimal breakthrough pore volume from the linear flow correlations.

2.5.2 Model Calculation Example

This section shows a calculation example for this model. The input data are from one set of our experiments, and are shown in **Table 2.9** below

Table 2.9 Input data for model application

Lithology	Indiana limestone	
Acid	15 wt% HCl	
Temperature	75	°F
Porosity	15%	
Permeability	5.9	mD
Mode of the pore radius	30	μm
Average Pore length	300	μm
Diffusion coefficient	3.5×10^{-5}	cm^2/s
$E_f C_0^{m-1}$	3.81×10^{-2}	cm/s

Step 1. Calculate optimal acid velocity in the mode-size pore.

In order to solve $\bar{v}_{p,\text{mode},opt}$, several iterates should be taken because the overall reaction rate coefficient also depends on this velocity. Assuming an initial $\bar{v}_p$ of 3 cm/s, the first iterate is shown through Eq. 2-69, Eq. 2-70 and Eq. 2-71.

$$K = 1.2819\left(\frac{\bar{v}_p}{r_{p,\text{mode}} L_{p,\text{mode}}}\right)^{1/3} D^{2/3}$$
$$= 1.2819\left(\frac{3\text{cm/s}}{30\times10^{-4}\text{cm}\cdot 300\times10^{-4}\text{cm}}\right)^{1/3}\cdot(3.5\times10^{-5}\text{cm}^2/\text{s})^{2/3} = 0.044\text{cm/s} \quad (2\text{-}69)$$

$$\kappa = \frac{KE_f C_0^{m-1}}{K + E_f C_0^{m-1}} = \frac{0.044\,\text{cm/s}\cdot 0.0381\,\text{cm/s}}{0.044\,\text{cm/s} + 0.0381\,\text{cm/s}} = 0.021\,\text{cm/s} \quad (2\text{-}70)$$

$$\bar{v}_{p,\text{mode},opt} = \frac{\kappa\Gamma_{p,\text{mode}} L_{p,\text{mode}}}{A_{p,\text{mode}}} = \frac{0.021\text{cm/s}\cdot(2\pi\cdot30\times10^{-4}\text{cm})\cdot300\times10^{-4}\text{cm}}{\pi(30\times10^{-4}\text{cm})^2} = 0.42\,\text{cm/s} \quad (2\text{-}71)$$

The second iterate starts from $\bar{v}_p$ of 0.42 cm/s.

$$K = 1.2819\left(\frac{\bar{v}_p}{r_{p,\text{mode}} L_{p,\text{mode}}}\right)^{1/3} D^{2/3}$$
$$= 1.2819\left(\frac{0.42\text{cm/s}}{30\times10^{-4}\text{cm}\cdot 300\times10^{-4}\text{cm}}\right)^{1/3}\cdot(3.5\times10^{-5}\text{cm}^2/\text{s})^{2/3} = 0.023\text{cm/s} \quad (2\text{-}72)$$

$$\kappa = \frac{KE_f C_0^{m-1}}{K + E_f C_0^{m-1}} = \frac{0.023\,\text{cm/s}\cdot 0.0381\,\text{cm/s}}{0.023\,\text{cm/s} + 0.0381\,\text{cm/s}} = 0.0144\,\text{cm/s} \quad (2\text{-}73)$$

$$\bar{v}_{p,\text{mode},opt} = \frac{\kappa\Gamma_{p,\text{mode}} L_{p,\text{mode}}}{A_{p,\text{mode}}} = \frac{0.0144\text{cm/s}\cdot(2\pi\cdot 30\times10^{-4}\text{cm})\cdot 300\times10^{-4}\text{cm}}{\pi(30\times10^{-4}\text{cm})^2} = 0.288\text{cm/s} \quad (2\text{-}74)$$

The third iterate starts from $\bar{v}_p$ of 0.288 cm/s.

$$K = 1.2819\left(\frac{\bar{v}_p}{r_{p,\text{mode}} L_{p,\text{mode}}}\right)^{1/3} D^{2/3}$$
$$= 1.2819\left(\frac{0.288\text{cm/s}}{30\times10^{-4}\text{cm}\cdot 300\times10^{-4}\text{cm}}\right)^{1/3}\cdot(3.5\times10^{-5}\text{cm}^2/\text{s})^{2/3} = 0.020\text{cm/s} \quad (2\text{-}75)$$

$$\kappa = \frac{KE_f C_0^{m-1}}{K + E_f C_0^{m-1}} = \frac{0.020\,\text{cm/s}\cdot 0.0381\,\text{cm/s}}{0.020\,\text{cm/s} + 0.0381\,\text{cm/s}} = 0.0133\,\text{cm/s} \quad (2\text{-}76)$$

$$\bar{v}_{p,\text{mode},opt} = \frac{\kappa\Gamma_{p,\text{mode}} L_{p,\text{mode}}}{A_{p,\text{mode}}} = \frac{0.0133\text{cm/s}\cdot(2\pi\cdot 30\times10^{-4}\text{cm})\cdot 300\times10^{-4}\text{cm}}{\pi(30\times10^{-4}\text{cm})^2} = 0.266\text{cm/s} \quad (2\text{-}77)$$

The fourth iterate starts from $\bar{v}_p$ of 0.266 cm/s, and the final $\bar{v}_{p,mode,opt}$ is calculated as 0.26 cm/s. It is close to the third iterate and the loop finishes.

Step 2. Calculate M_2 based on the pore size density function.

The pore size distribution of this Indiana limestone has been obtained in section 2.3, and we bring it here.

$$\eta(A) = \frac{25834}{1.14\sqrt{2\pi}A}\exp[-\frac{1}{2.6}(\ln A + 9.2)^2] \tag{2-78}$$

M_2 is calculated through Eq. 2-50, and is shown below.

$$M_2 = N\exp[2(\mu+\sigma^2)] = 25834 \times \exp[2(-9.2+1.3)] = 3.55\times10^{-3}\,\text{cm} \tag{2-79}$$

Step 3. Upscale $\bar{v}_{p,\text{mode},opt}$ to $v_{i,tip,opt}$ through Eq. 2-57.

$$v_{i,tip,opt} = \frac{\bar{v}_{p,\text{mode},opt}}{A_{p,\text{mode}}}\frac{\bar{L}_p M_2}{\phi} = \frac{0.26\,\text{cm/s}}{2.827\times10^{-5}\,\text{cm}^2}\cdot\frac{0.03\text{cm}\times3.55\times10^{-3}\,\text{cm}}{0.15} = 6.68\,\text{cm/s} \tag{2-80}$$

Step 4. Wormhole diameter calculation

Table 2.10 shows parameters that are used for wormhole diameter calculation.

Table 2.10 Input data for wormhole diameter calculation

Permeability, k	5.9	md
Porosity, ϕ	0.15	
Viscosity, μ	1	cp
Pore radius, r_p	30	μm
Δp to the core wall	1	psi
Core radius, r_{core}	0.75	inch
Acid capacity number, N_{ac}	0.0144	
$v_{i,tip}$	6.68	cm/s

In the table above, Δp to the core wall is taken as 1 psi (Hung et al. 1989). The calculation is shown below.

$$v_{wh} = v_{i,tip,opt} N_{ac} = 6.68\text{cm/s} \times 0.0144 = 9.6 \times 10^{-2}\ \text{cm/s} \tag{2-81}$$

$$q_{loss} = \frac{2\pi k \Delta p}{\mu \ln(\frac{r_{core}}{r_p})} = \frac{2\pi \times 5.9 \times 10^{-15} \times 10 \times 6894.76}{1 \times 10^{-3} \ln(\frac{0.75 \times 2.54}{30 \times 10^{-4}})} = 3.96 \times 10^{-7}\ \text{m}^2/\text{s} = 0.00396\text{cm}^2/\text{s}$$

(2-82)

Substituting Eq. 2-81 and Eq. 2-82 into Eq. 2-66,

$$r_{wh}^2 - r_p^2 = \frac{0.00396}{0.15\pi} \times 0.0144 \frac{7 r_{wh}}{9.6 \times 10^{-2}} \tag{2-83}$$

We can get wormhole diameter by solving equation above, r_{wh}=8.82×10^{-3}cm.

Step 5. Optimal acid interstitial velocity and optimal breakthrough pore volume

$$v_{i,opt} = \frac{d_{wh}}{d_{core}} v_{i,tip,opt} = \frac{2 \times 8.82 \times 10^{-3}}{1.5 \times 2.54} \times 6.68 = 0.031\text{cm/s} = 1.86\text{cm/min} \tag{2-84}$$

$$PV_{bt,opt} = \frac{d_{wh}}{d_{core} N_{ac}} = \frac{2 \times 8.82 \times 10^{-3}}{1.5 \times 2.54 \times 0.0144} = 0.321 \tag{2-85}$$

The experimental data for this case is shown in **Fig. 2.24**. The optimal conditions for this set of experiments are $v_{i,opt}$=1.98 cm/min, $PV_{bt,opt}$=0.367. We can see the model-predicted results and experimental results are close.

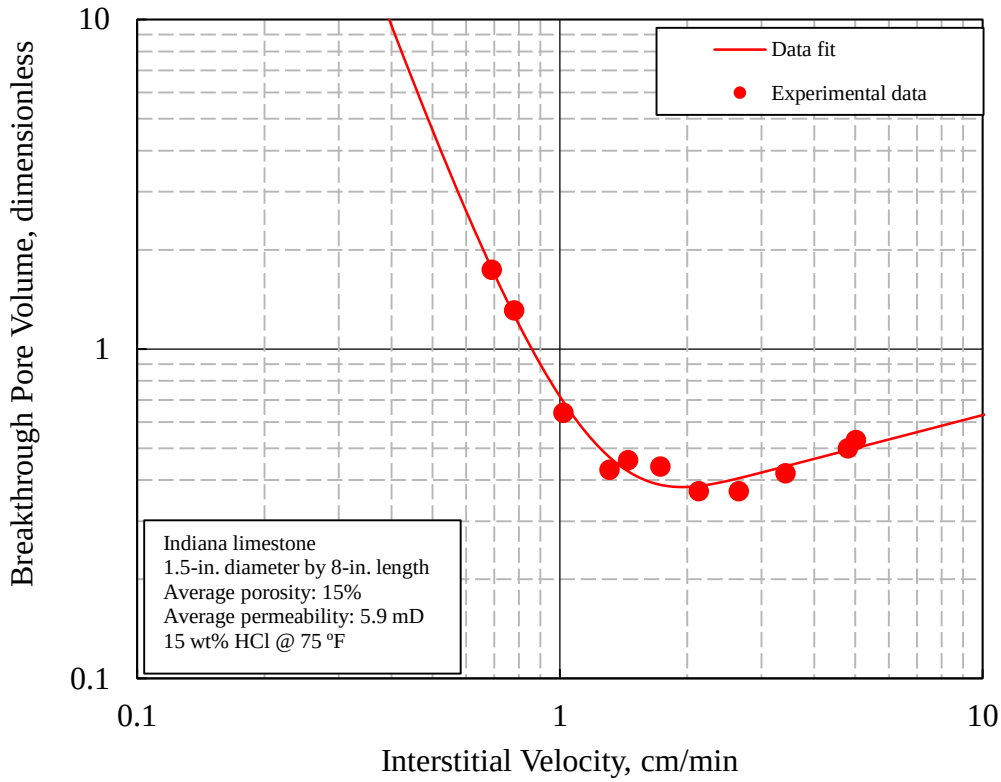

Fig. 2.24 Wormhole efficiency relationship for Indiana limestone at 75 °F (Dong, 2012)

3 SENSITIVITY ANALYSIS OF WORMHOLE PROPAGATION

3.1 Introduction

Acidizing is a reactive transport process that depends on temperature, acid type/concentration, mineralogy and pore size distribution. Previous experimental studies show qualitative effects of these factors. Among these factors, we use the model developed in Section 2 to study the effects of temperature and acid concentration quantitatively in this section. Acidizing coreflood experiments were carried out to verify these effects. In addition, all previous experimental data are gathered and analyzed in this section.

At the end of this section, the effect of pore-scale heterogeneity on optimal conditions is briefly discussed. Thin section images for different types of limestone are also presented.

3.2 Surface Reaction and Diffusion

As discussed in Section 2, the overall reaction in acidizing consists of acid diffusion to the pore surface and acid/pore surface reaction. Both of these two processes are affected by temperature and acid concentration. In order to quantify their effects, reliable correlations are needed. This is discussed below.

3.2.1 Surface Reaction Rates between HCl and Carbonate Rocks

Surface reactions rates for both calcite and dolomite with HCl have been investigated and are summarized below (Lund et al. 1973, Lund et al. 1975).

HCl + Calcite:

$$r = E_f C_s^{0.63} \tag{3-1}$$

$$E_f = E_{f0} \exp(-\frac{\Delta E}{RT}) \tag{3-2}$$

where E_f is the surface reaction rate constant, E_{f0} is the frequency factor, C_s is the surface acid concentration, r is the surface reaction rate, T is temperature, R is the gas constant and ΔE is the activation energy.

HCl + Dolomite:

$$r = E_f C_s^n \tag{3-3}$$

$$E_f = E_{f0} \exp(-\frac{\Delta E}{RT}) \tag{3-4}$$

$$n = \frac{6.21\times10^{-4}T}{1-2\times10^{-3}T} \tag{3-5}$$

where n is the reaction order, which depends on the temperature for HCl/dolomite reaction.

Table 3.1 shows values and units of these parameters.

Table 3.1 Surface reaction parameters for HCl/calcite and HCl/dolomite

	Calcite	Dolomite	Units
E_{f0}	5.581×10^{8}	9.4×10^{10}	$gmole^{1-n}\ cm^{3n-2}\ s^{-1}$
ΔE	15000	22500	cal/gmole
n	0.63	Temperature dependent	dimensionless
R	1.987	1.987	cal/K/gmole

While using these equations above, the unit of temperature is Kevin; the unit of acid concentration is gmole/ml, and the unit of reaction rate is gmole/cm^2/s. Calculation examples of surface reaction rates for 15 wt% HCl and calcite, 15 wt% HCl and dolomite are illustrated below. The reaction temperature is room temperature, 75 °F.

$$T = 75F = 297.1K \tag{3-6}$$

$$C_s = 15\text{wt}\% = 4.4\times10^{-3}\,\text{gmole/ml} \tag{3-7}$$

Calcite:

$$E_f = 5.581\times10^{8}\exp(-\frac{15000}{1.987\times297.1}) = 5.122\times10^{-3}\,\text{gmole}^{1-n}\cdot\text{cm}^{3n-2}\cdot\text{s}^{-1} \tag{3-8}$$

$$r = 5.122\times10^{-3}\times(4.4\times10^{-3})^{0.63} = 1.678\times10^{-4}\,\text{gmole/cm}^2\text{/s} \tag{3-9}$$

Dolomite:

$$n = \frac{6.21\times10^{-4}\times297.1}{1-0.002\times297.1} = 0.44 \tag{3-10}$$

$$E_f = 9.4\times10^{10}\exp(-\frac{22500}{1.987\times297.1}) = 2.63\times10^{-6}\,\text{gmole}^{1-n}\cdot\text{cm}^{3n-2}\cdot\text{s}^{-1} \tag{3-11}$$

$$r = 2.63\times10^{-6}\times(4.4\times10^{-3})^{0.44} = 2.45\times10^{-7}\,\text{gmole/cm}^2\text{/s} \tag{3-12}$$

As shown in the calculation, with 15 wt% HCl, the surface reaction rate of dolomite is around three orders of magnitude lower than that of calcite at room temperature. The significant difference in surface reaction rates between HCl/calcite and HCl/dolomite results in different acidizing design methods for these two different formations.

3.2.2 Acid Diffusion Rate

Diffusion happens where concentration gradients exist. When acid is flowing inside a single pore, the diffusion process is also affected by the axial flow velocity. The rate of the diffusion process for the flowing acid in a pore is described by the mass transfer coefficient, *K*. It can be calculated with Eq. 3-13 (Levich, Veniamin G, 1962).

$$K = 1.2819(\frac{\bar{v}_p}{r_p L_p})^{1/3} D^{2/3} \tag{3-13}$$

In this equation, the diffusion coefficient *D* needs to be measured for each application. Conway et al. (1999) studied the diffusion coefficients using a diaphragm cell and a rotating disk for straight, gelled and emulsified HCl. Based on their experimental results, they developed correlations to calculate diffusivity of H^+, Ca^{2+} and Mg^{2+}. For straight HCl, the correlations are shown by Eq. 3-14.

$$D(H^+) = \exp(-\frac{2918.54}{T} - 0.589\sqrt{\frac{[Ca^{2+}]}{[H^+]}} - 0.789\sqrt{\frac{[Mg^{2+}]}{[H^+]}} + 0.0452[H^+] - 4.995) \tag{3-14}$$

For dilute HCl, we can ignore the effect of calcium and magnesium ions, and the diffusivity of H^+ can be approximated as below.

$$D(H^+) = \exp(-\frac{2918.54}{T} + 0.0452[H^+] - 4.995) \tag{3-15}$$

In Eq. 3-14 and Eq. 3-15, the unit of the diffusion coefficient is cm^2/s, and the unit of the ion concentration is gmole/L (molar).

3.3 Effect of Temperature

Temperature affects both the surface reaction process and the mass transfer process. Generally, increasing temperature leads to increases of surface reaction rate and mass transfer rate exponentially. However, analysis shows surface reactivity has a much stronger dependence on temperature than diffusivity. **Fig. 3.1** shows the plot of Eq. 3-1 and **Fig. 3.2** shows the plot of Eq. 3-15 for the same temperature range. The case is for 15 wt% HCl and calcite.

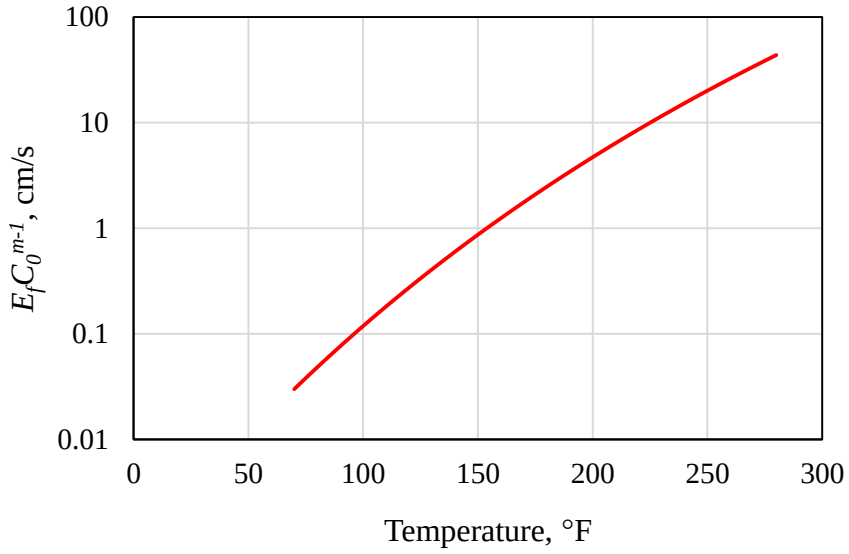

Fig. 3.1 Temperature effect on surface reactivity of 15 wt% HCl and calcite

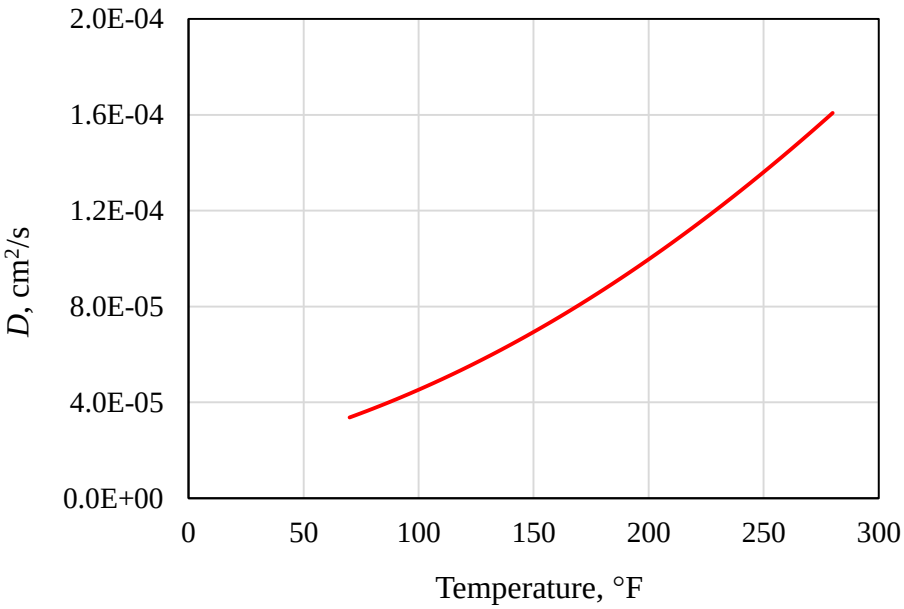

Fig. 3.2 Temperature effect on 15 wt% HCl diffusivity

As temperature increases from 70 °F to 280 °F, the surface reactivity increases 1456 times while acid diffusivity increases only 4.8 times.

3.3.1 Model-Based Prediction

Provided rock pore properties and pore size distribution, the model developed in Section 2 can be used to calculate optimal conditions. In the meanwhile, for the same rock, this model can also be used to study the sensitivity of different parameters. In this section, we derive a correlation that describes the temperature effect on the optimal conditions. In order to have a clear derivation, Eq. 3-16, 3-17, 3-18 and 3-19 are brought from Section 2 and shown below.

$$v_{i,opt} = \frac{d_{wh}}{d_{core}} v_{i,tip,opt} \tag{3-16}$$

$$d_{wh} = d_{core} PV_{bt,opt} N_{ac} \tag{3-17}$$

$$v_{i,tip,opt} = \frac{\bar{v}_{p,\text{mode,opt}}}{A_{p,\text{mode}}} \cdot \frac{\bar{L}_p M_2}{\phi} \tag{3-18}$$

$$\bar{v}_{p,\text{mode},opt} = \frac{\kappa \Gamma_{p,\text{mode}} L_{p,\text{mode}}}{A_{p,\text{mode}}} \tag{3-19}$$

The ratio between two different optimal acid fluxes at two different temperatures can be derived, and are shown by Eq. 3-20.

$$\begin{aligned} \frac{v_{i,opt1}}{v_{i,opt2}} &= \frac{d_{wh1}}{d_{core1}} v_{i,tip,opt1} \Big/ \frac{d_{wh2}}{d_{core2}} v_{i,tip,opt2} = \frac{d_{wh1}}{d_{wh2}} \cdot \frac{v_{i,tip,opt1}}{v_{i,tip,opt2}} \cdot \frac{d_{core2}}{d_{core1}} \\ &= \frac{d_{core1} PV_{bt,opt1} N_{ac1}}{d_{core2} PV_{bt,opt2} N_{ac2}} \cdot \frac{v_{i,tip,opt1}}{v_{i,tip,opt2}} \cdot \frac{d_{core2}}{d_{core1}} = \frac{\bar{v}_{p,\text{mode1}}}{\bar{v}_{p,\text{mode2}}} \cdot \frac{PV_{bt,opt1}}{PV_{bt,opt2}} \\ &= \frac{\kappa_1}{\kappa_2} \cdot \frac{PV_{bt,opt1}}{PV_{bt,opt2}} \end{aligned} \tag{3-20}$$

For a fully diffusion limited reaction,

$$\kappa = K = 1.2819 \left(\frac{\bar{v}_{p,\text{mode},opt}}{r_{p,\text{mode}} L_{p,\text{mode}}} \right)^{1/3} D^{2/3} \tag{3-21}$$

Substituting Eq. 3-21 into Eq. 3-20, we can get

$$\frac{v_{i,opt1}}{v_{i,opt2}} = \frac{D_1}{D_2} \cdot \frac{PV_{bt,opt1}}{PV_{bt,opt2}} \tag{3-22}$$

Eq. 3-22 describes the temperature effect on optimal conditions for diffusion limited acidizing coreflood experiments. Note that Eq. 3-16 and Eq. 3-17 are only valid for linear acidizing coreflood experiments, so till now Eq. 3-22 is also only valid for the

optimal conditions of linear acidizing coreflood experiments. The application of Eq. 3-22 to other flow geometries is discussed at the end of this section. Before that, experimental results are used to verify its validity.

3.3.2 Experimental Study

Acidizing coreflood experimental studies have been carried out for different temperatures by several authors. Wang et al. (1993) found increasing temperature results in an increase of $v_{i,opt}$. The same trend was also found by other investigators (Fredd and Fogler, 1999, Bazin, 2001, and Furui et al., 2010). However, previous research did not quantify this temperature effect. This section compares the experimental results with those calculated from Eq. 3-22. It is found that Eq. 3-22 can describe the temperature effect on the optimal conditions for diffusion limited reactions.

The experimental data from Wang et al. (1993) are plotted and summarized in **Fig. 3.3** and **Table 3.2**.

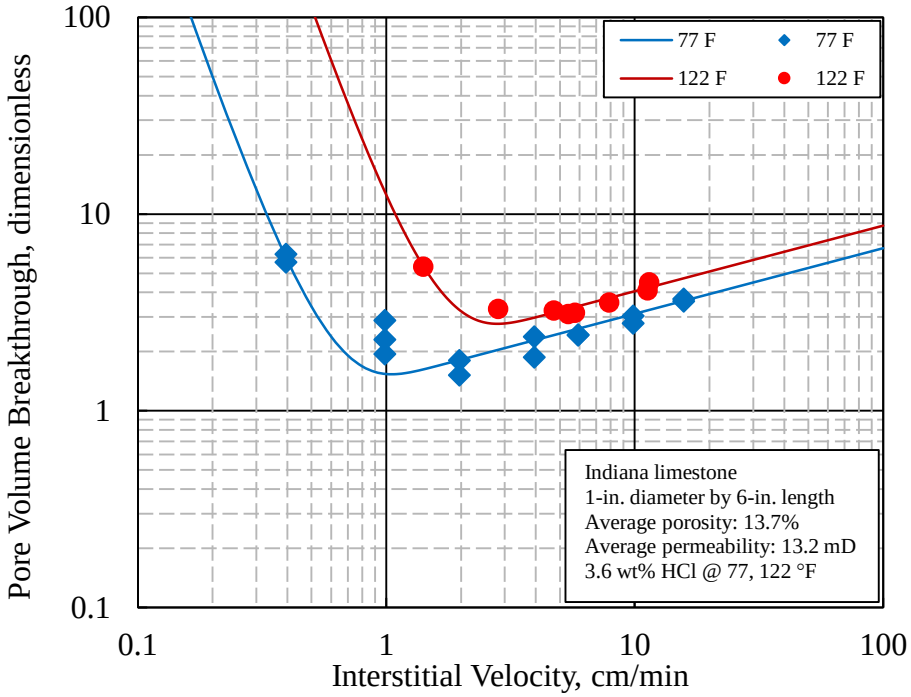

Fig. 3.3 Wormhole efficiency relationships at 77 °F and 122 °F (Wang et al. 1993)

Table 3.2 Optimal conditions in Fig. 3.3

Temperature	$v_{i,opt}$	$PV_{bt,opt}$	D
°F	cm/min		cm^2/s
77	1.07	1.48	3.10×10^{-5}
122	2.81	2.67	4.72×10^{-5}

The yellow columns are experimental results and the green column is calculated through Eq. 3-15. From experimental results

$$\frac{v_{i,opt,122F}}{v_{i,opt,77F}} = 2.63 \tag{3-23}$$

The ratio of $v_{i,opt}$ from Eq. 3-22 is

$$\frac{v_{i,opt,122F}}{v_{i,opt,77F}} = \frac{PV_{bt,opt,122F}}{PV_{bt,opt,77F}} \cdot \frac{D_{122F}}{D_{77F}} = 2.74 \tag{3-24}$$

We can see that the ratios from both experiments and our model are satisfactorily close. We may infer that it is the diffusion that governs the acidizing process between HCl and calcite. Further comparison is made based on other experimental results.

Bazin (2001) conducted acidizing coreflood experiments for three different temperatures. The experimental data and results are summarized and presented in **Fig. 3.4** and **Table 3.3**.

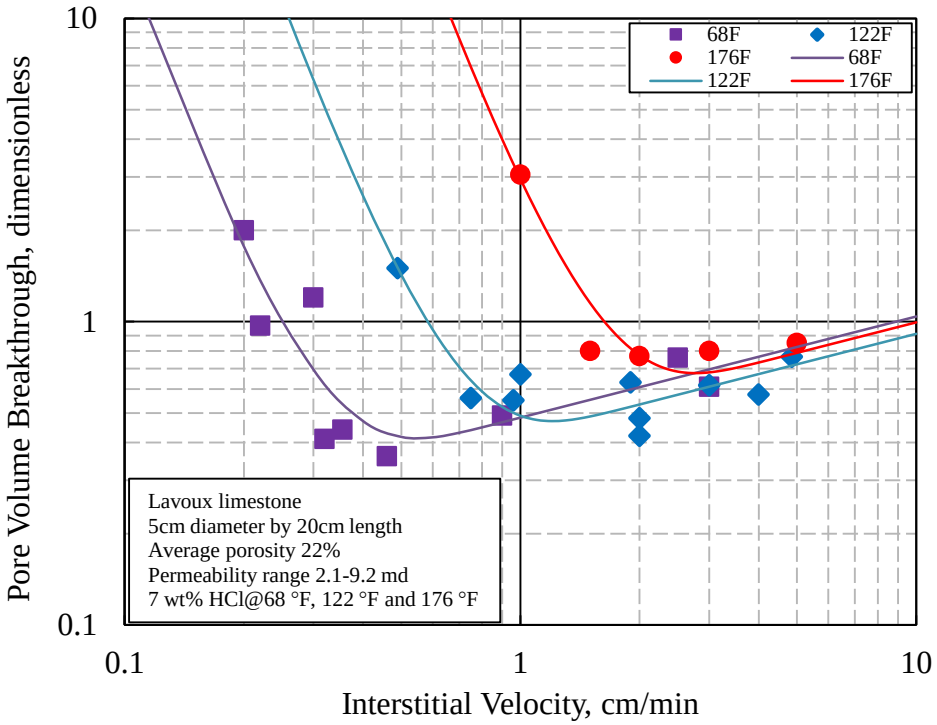

Fig. 3.4 Wormhole efficiency relationships at 68 °F, 122 °F and 176 °F (Bazin, 2001)

Table 3.3 Optimal conditions in Fig. 3.4

Bazin	$v_{i,opt}$	$PV_{bt,opt}$	D
°F	cm/min		cm^2/s
68	0.56	0.40	2.95×10^{-5}
122	1.23	0.45	4.93×10^{-5}
176	2.82	0.65	7.55×10^{-5}

If we compare the optimal conditions between 122 °F and 176 °F, we can see the experimental results are close to model-calculated results, as shown below.

The ratio from experimental results is

$$\frac{v_{i,opt,176F}}{v_{i,opt,122F}} = 2.29 \tag{3-25}$$

The ratio of $v_{i,opt}$ from Eq. 3-22 is

$$\frac{v_{i,opt,176F}}{v_{i,opt,122F}} = \frac{PV_{bt,opt,176F}}{PV_{bt,opt,122F}} \cdot \frac{D_{176F}}{D_{122F}} = 2.20 \tag{3-26}$$

However, if we compare the optimal conditions between 68 °F and 122 °F, we can see that the ratio from experimental results is larger than the model-calculated one.

The ratio of $v_{i,opt}$ from experimental results is:

$$\frac{v_{i,opt,122F}}{v_{i,opt,68F}} = 2.2 \tag{3-27}$$

The ratio of $v_{i,opt}$ from Eq. 3-22 is:

$$\frac{v_{i,opt,122F}}{v_{i,opt,68F}} = \frac{PV_{bt,opt,122F}}{PV_{bt,opt,68F}} \cdot \frac{D_{122F}}{D_{68F}} = 1.88 \tag{3-28}$$

This indicates that the experiments at 68 °F are not fully diffusion limited. From Fig. 2.3 we can see, if the surface reaction rate is within around 100 times larger than the mass transfer rate, both of the two processes affect the overall reaction rate. In this case, the overall reaction rate is smaller than each of the surface reaction rate and mass transfer rate due to the nature of Eq. 2-9. When the temperature increases, the overall reaction rate eventually equals to the mass transfer rate. Compared with fully diffusion limited reaction, the overall reaction rate coefficient increases more than the increase of the diffusion coefficient. Therefore, the value calculated in Eq. 3-28 is less than the value through experiments in Eq. 3-27.

Similar analysis are carried out for the data from Fredd and Fogler (1999). The experimental data and results are summarized and presented in **Fig. 3.5** and **Table 3.4**.

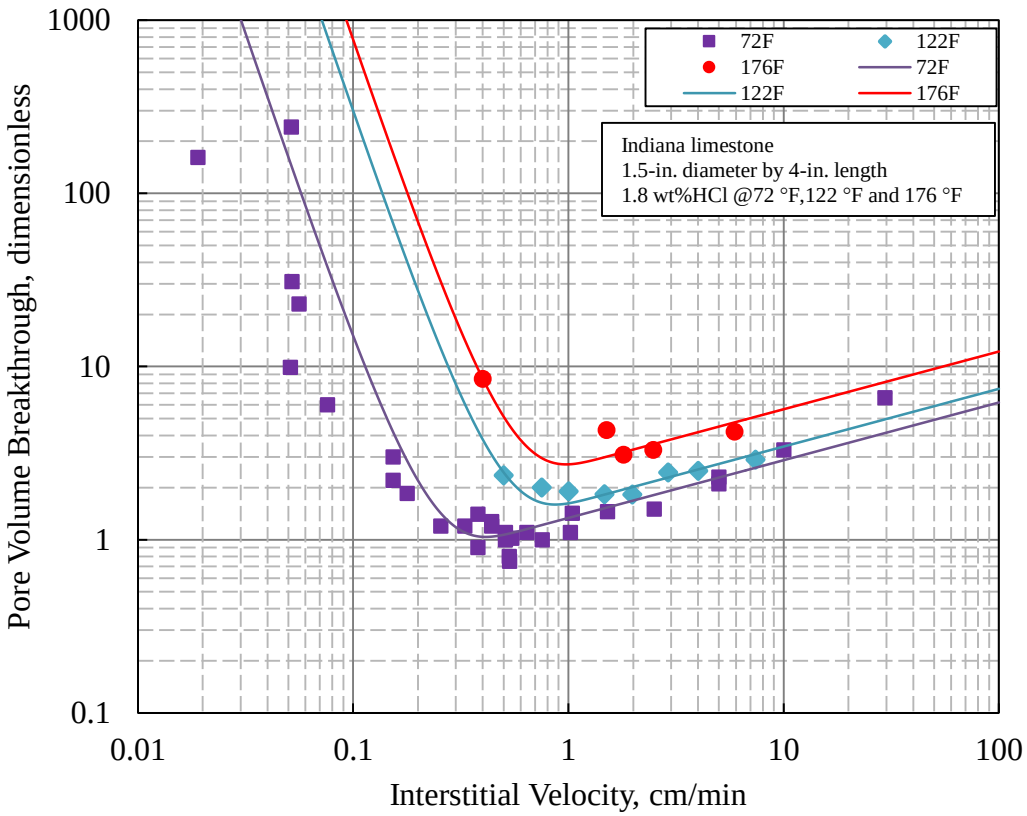

Fig. 3.5 Wormhole efficiency relationships at 72 °F, 122 °F and 176 °F

(Fredd and Fogler, 1999)

Table 3.4 Optimal conditions in Fig. 3.5

Fredd	$v_{i,opt}$	$PV_{bt,opt}$	D
°F	cm/min		cm^2/s
72	0.4	1.1	2.87×10^{-5}
122	0.89	1.54	4.61×10^{-5}
176	0.99	2.62	7.05×10^{-5}

If we compare $v_{i,opt}$ at the three different temperatures, the ratios of $v_{i,opt}$ from experimental results are:

$$\frac{v_{i,opt,122F}}{v_{i,opt,72F}} = 2.23 \tag{3-29}$$

$$\frac{v_{i,opt,176F}}{v_{i,opt,122F}} = 1.11 \tag{3-30}$$

The ratios of $v_{i,opt}$ from Eq. 3-22 are

$$\frac{v_{i,opt,122F}}{v_{i,opt,72F}} = \frac{PV_{bt,opt,122F}}{PV_{bt,opt,72F}} \cdot \frac{D_{122F}}{D_{72F}} = 2.25 \tag{3-31}$$

$$\frac{v_{i,opt,176F}}{v_{i,opt,122F}} = \frac{PV_{bt,opt,176F}}{PV_{bt,opt,122F}} \cdot \frac{D_{176F}}{D_{122F}} = 2.60 \tag{3-32}$$

We can see the comparison between 72 °F and 122 °F is satisfactory. However, the comparison between 122 °F and 176 °F is not.

The last set of experimental data comes from Furui et al. (2010). Acidizing coreflood experiments with Kansas chalk were carried out at 150 °F and 200 °F. Their experimental data and results are presented and summarized in **Fig. 3.6** and **Table 3.5**.

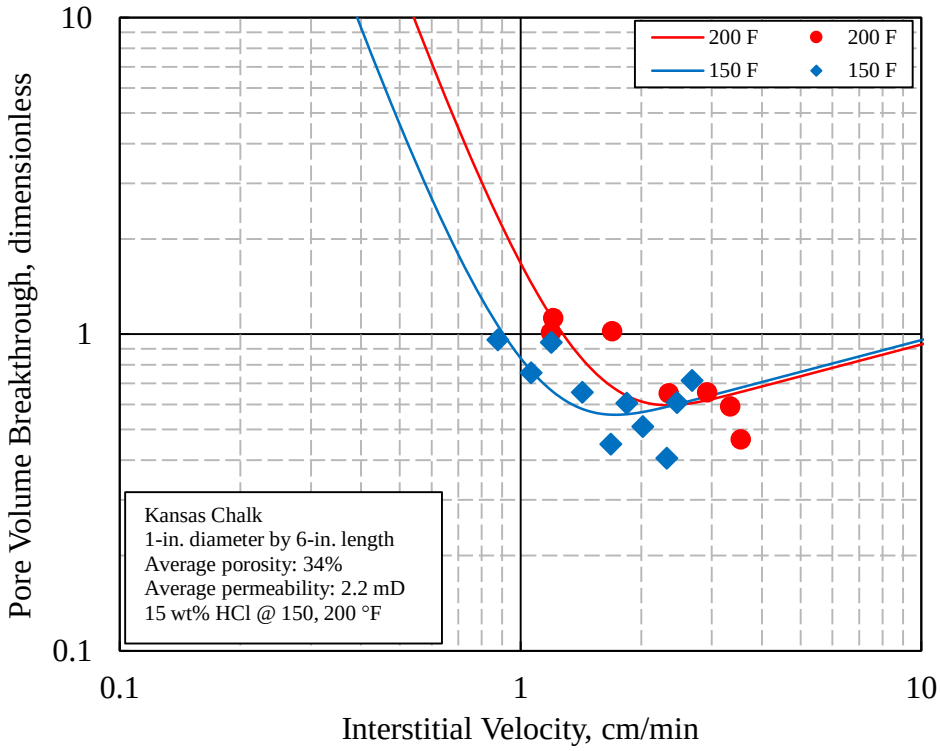

Fig. 3.6 Wormhole efficiency relationships at 150 °F and 200 °F (Furui et al. 2010)

Table 3.5 Optimal conditions in Fig. 3.6

Temperature	$v_{i,opt}$	$PV_{bt,opt}$	D
°F	cm/min		cm^2/s
150	1.76	0.54	6.91×10^{-5}
200	2.38	0.58	9.93×10^{-5}

Experimentally,

$$\frac{v_{i,opt,200F}}{v_{i,opt,150F}} = 1.35 \tag{3-33}$$

Model calculated results are

$$\frac{v_{i,opt,200F}}{v_{i,opt,150F}} = \frac{PV_{bt,opt,200F}}{PV_{bt,opt,150F}} \cdot \frac{D_{200F}}{D_{150F}} = 1.54 \tag{3-34}$$

We can see that the ratio from experimental results are close to the ratio calculated from Eq. 3-22.

In summary, Eq. 3-22 is able to describe the effect of temperature on the optimal conditions for HCl and calcite. And also, we can see how acid diffusion coefficient affects the optimal conditions. If the overall reaction is diffusion limited, we can decrease the optimal injection rate by lowering acid diffusion rates. In this way, acid can penetrate to greater distances into formation, and more stimulation results can be achieved (Hoefner and Fogler, 1987).

Eq. 3-22 can be written in another form. In a linear coreflood acidizing experiment, the average wormhole propagation velocity equals to the ratio between acid interstitial velocity and breakthrough pore volume, as denoted by Eq. 3-35.

$$\bar{v}_{wh} = \frac{v_i}{PV_{bt}} \tag{3-35}$$

Substituting Eq. 3-35 into Eq. 3-22, another relationship (Eq. 3-36) can be obtained as shown below. At optimal conditions, average wormhole propagation velocity is linearly proportional to the diffusion coefficient.

$$\frac{\bar{v}_{wh,opt1}}{\bar{v}_{wh,opt2}} = \frac{D_1}{D_2} \tag{3-36}$$

Both Eq. 3-22 and Eq. 3-36 are derived based on correlations of linear coreflood acidizing experiments, and their effectiveness have been verified by experimental results.

However, they actually have general applications and can be used for other flow geometries, like radial flow and spherical flow. This can be proved as following.

Hung's model (Hung et al. 1989) shows that the instantaneous wormhole propagation velocity is proportional to the wormhole tip interstitial velocity, acid capacity number and the ratio between acid concentration at the wormhole tip and the original bulk acid concentration. It can be described by Eq. 3-37.

$$v_{wh} = v_{i,tip}(\frac{C_{tip}}{C_0})N_{ac} \tag{3-37}$$

Based on Eq. 3-37, the wormhole propagation velocity at the optimal condition with full acid strength (C_{tip} equals to C_0) can be described by Eq. 3-38.

$$v_{wh,opt} = v_{i,tip,opt}N_{ac} \tag{3-38}$$

From Eq. 3-38, for the same rock and acid concentration, the ratio between two different optimal wormhole propagation velocities at two different temperatures is

$$\frac{v_{wh,opt1}}{v_{wh,opt2}} = \frac{v_{i,tip,opt1}}{v_{i,tip,opt2}} \tag{3-39}$$

Substituting Eq. 3-18 and Eq. 3-19 into Eq. 3-39, we can get Eq. 3-40 as shown below. It describes the instantaneous wormhole propagation velocity at the optimal condition is linearly proportional to the overall reaction rate coefficient.

$$\frac{v_{wh,opt1}}{v_{wh,opt2}} = \frac{\kappa_1}{\kappa_2} \tag{3-40}$$

For the diffusion limited reaction, the overall reaction rate coefficient equals to the mass transfer coefficient.

$$\kappa = K = 1.2819\left(\frac{\bar{v}_{p,\mathrm{mode},opt}}{r_{p,\mathrm{mode}} L_{p,\mathrm{mode}}}\right)^{1/3} D^{2/3} \tag{3-41}$$

Substituting Eq. 3-41 and Eq. 2-32 into Eq. 3-40, we can get Eq. 3-42. At optimal conditions, the instantaneous wormhole propagation velocity is proportional to the acid diffusion coefficient.

$$\frac{v_{wh,opt1}}{v_{wh,opt2}} = \frac{D_1}{D_2} \tag{3-42}$$

Eq. 3-42 has the same form as Eq. 3-36. However, Eq. 3-42 is derived based on Hung's model and the model developed in Section 2, both of which describe the instantaneous wormholing and have no limitations on flow geometries. Therefore, Eq. 3-42 also has general applications without flow geometry limitations.

The effectiveness of Eq. 3-22 has been verified by coreflood experimental data as discussed before. So its transformed form, Eq. 3-36, is also valid. In linear acidizing coreflood experiments, the wormhole competition disappears very soon and the fluid loss along the dominant wormhole is stable after a certain penetration length, so we can approximate the instantaneous wormhole propagation velocity as the average wormhole propagation velocity. In this way, the effectiveness of Eq. 3-42 is verified indirectly.

Therefore, in general, Eq. 3-22 and Eq. 3-42 are able to describe the temperature effect on optimal conditions for a diffusion limited reaction.

3.4 Effect of Acid Concentration

Acid concentration is another factor that affects optimal conditions. This section presents the experimental studies, and discusses the reason for its effect based on our model. In order to have detailed analysis, original experimental results are summarized and listed in this section.

3.4.1 Experimental Results

Bazin (2001) studied the acid concentration effect with four different acid concentrations, 0.7 wt%, 3.5 wt%, 7 wt% and 17.5 wt%. Her results are plotted and summarized in **Fig. 3.7** and **Table 3.6**. It shows that $v_{i,opt}$ increases with increasing acid concentration, and $PV_{bt,opt}$ decreases. In Table 3.6, yellow columns are experimental results and green columns are calculated results. In the green columns, the optimal wormhole propagation velocity, acid capacity number and optimal wormhole tip interstitial velocity are calculated through Eq. 3-43, 3-44 and 3-45 below.

$$v_{wh,opt} = \frac{v_{i,opt}}{PV_{bt,opt}} \tag{3-43}$$

$$N_{ac} = \frac{\phi \beta_{wt\%} \rho_a}{(1-\phi)\rho_r} \tag{3-44}$$

$$v_{i,tip,opt} = \frac{v_{wh,opt}}{N_{ac}} \tag{3-45}$$

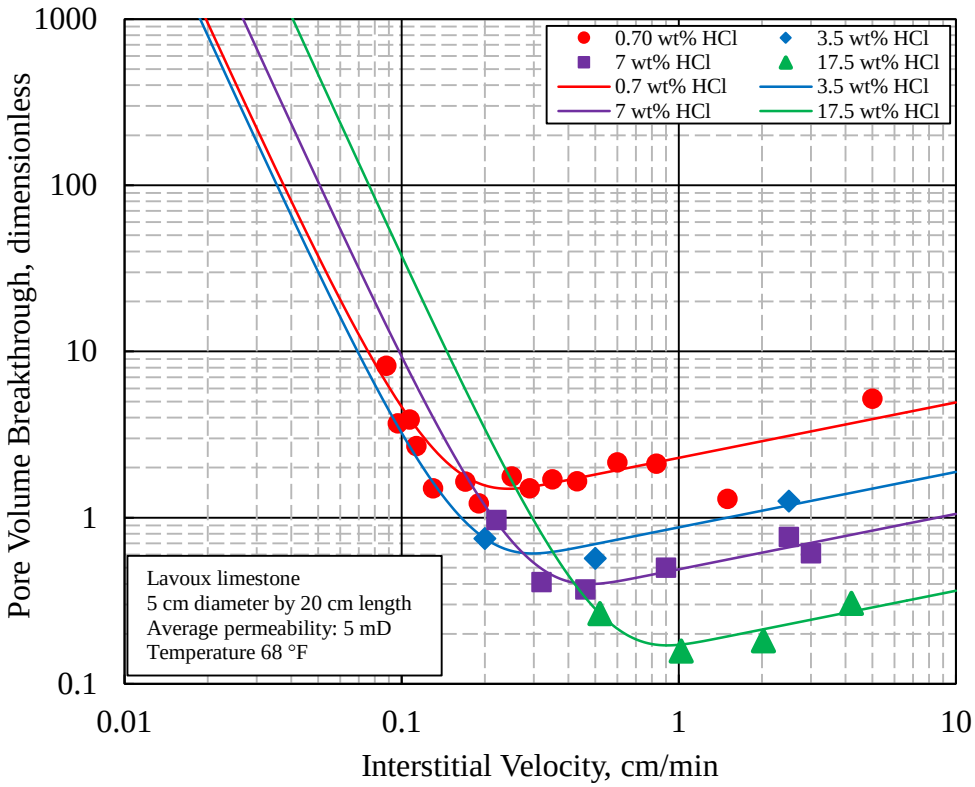

Fig. 3.7 Wormhole efficiency relationships of 0.7 wt%, 3.5 wt%, 7 wt% and 17.5 wt% HCl (Bazin, 2001)

Table 3.6 Optimal conditions in Fig. 3.7

C	$v_{i,opt}$	$PV_{bt,opt}$	$v_{wh,opt}$	N_{ac}	$v_{i,tip,opt}$
wt%	cm/min		cm/min		cm/min
0.7%	0.25	1.44	0.174	0.001	173.749
3.5%	0.3	0.58	0.517	0.005	102.103
7.0%	0.49	0.38	1.289	0.010	125.113
17.5%	0.93	0.16	5.813	0.027	214.672

Similar trend is observed by Wang et al. (1993). She investigated the concentration effect with three acid concentrations, 0.5 wt%, 3.6 wt% and 15 wt%. Generally, increasing acid concentration results in increasing $v_{i,opt}$ and decreasing $PV_{bt,opt}$. Her experimental results are summarized in **Fig. 3.8** and **Table 3.7**.

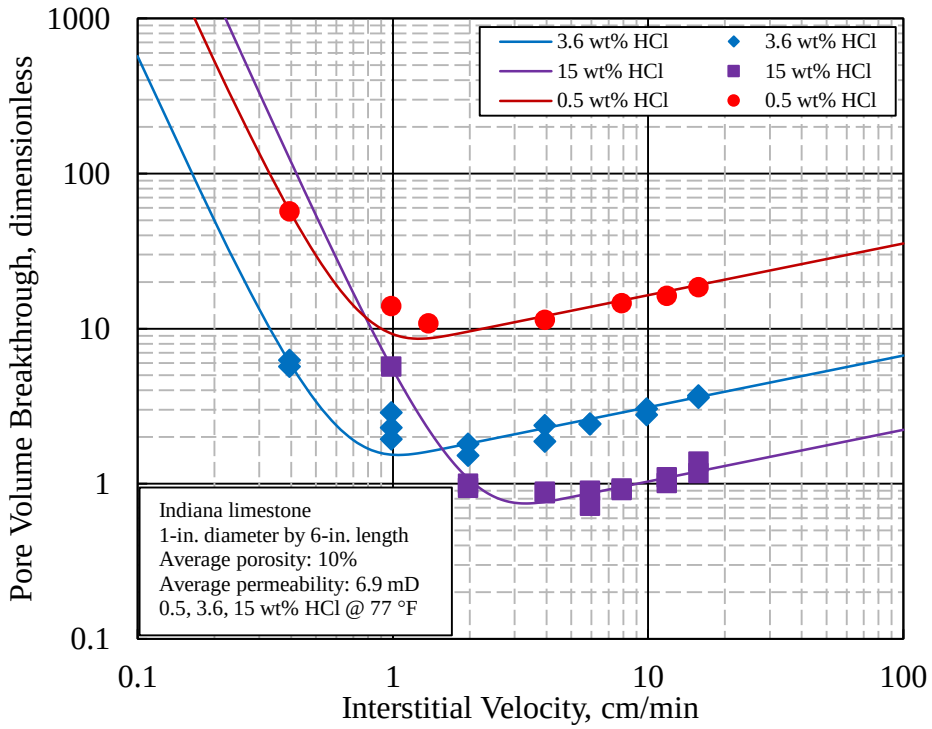

Fig. 3.8 Wormhole efficiency relationships of 0.5 wt%, 3.6 wt% and 15 wt% HCl (Wang et al. 1993)

Table 3.7 Optimal conditions in Fig. 3.8

C	$v_{i,opt}$	$PV_{bt,opt}$	$v_{wh,opt}$	N_{ac}	$v_{i,tip,opt}$
wt%	cm/min		cm/min		cm/min
0.5%	1.29	8.3	0.16	0.0003	553.34
3.6%	1.07	1.48	0.72	0.002	352.04
15.0%	3.37	0.72	4.68	0.009	517.92

However, experiments carried out in this study show a reversed concentration effect on the optimal interstitial velocity. We acidized Desert Pink limestone with 15 wt% and 28 wt% HCl at room temperature. The experimental results are plotted and summarized in **Fig. 3.9** and **Table 3.8**. The raw experimental data for 15 wt% HCl are from Etten (2015). The raw experimental data for 28 wt% HCl (this study) are shown in Appendix B.

We can see the $v_{i,opt}$ of 28 wt% HCl is less than that of 15 wt% HCl. The $PV_{bt,opt}$ keeps the same trend.

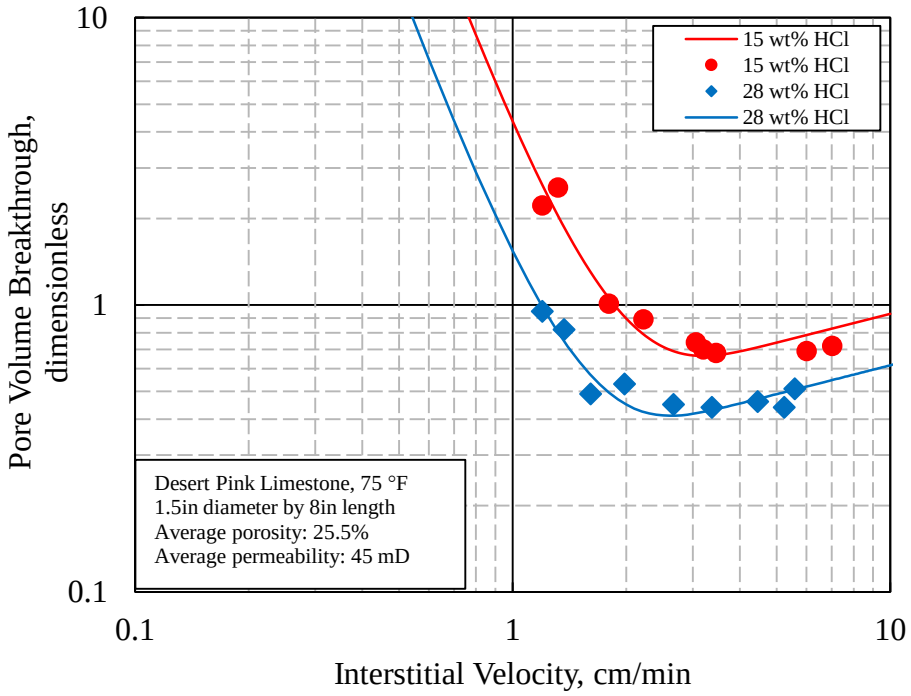

Fig. 3.9 Wormhole efficiency relationships of Desert Pink limestone for 15 wt% and 28 wt% HCl

Table 3.8 Optimal conditions in Fig. 3.9

C	$v_{i,opt}$	$PV_{bt,opt}$	$v_{wh,opt}$	N_{ac}	$v_{i,tip,opt}$
wt%	cm/min		cm/min		cm/min
15%	3.25	0.64	5.08	0.027	187.30
28%	2.67	0.4	6.68	0.054	124.36

In order to further verify this phenomenon, we acidized Indiana limestone with 15 wt% and 28 wt% HCl. The experimental results are plotted and summarized in

Fig. 3.10 and **Table 3.9**. The raw experimental data for 15 wt% HCl are from Etten (2015). The raw experimental data for 28 wt% HCl (this study) are shown in Appendix B. The $v_{i,opt}$ of 28 wt% HCl is also less than that of 15 wt% HCl.

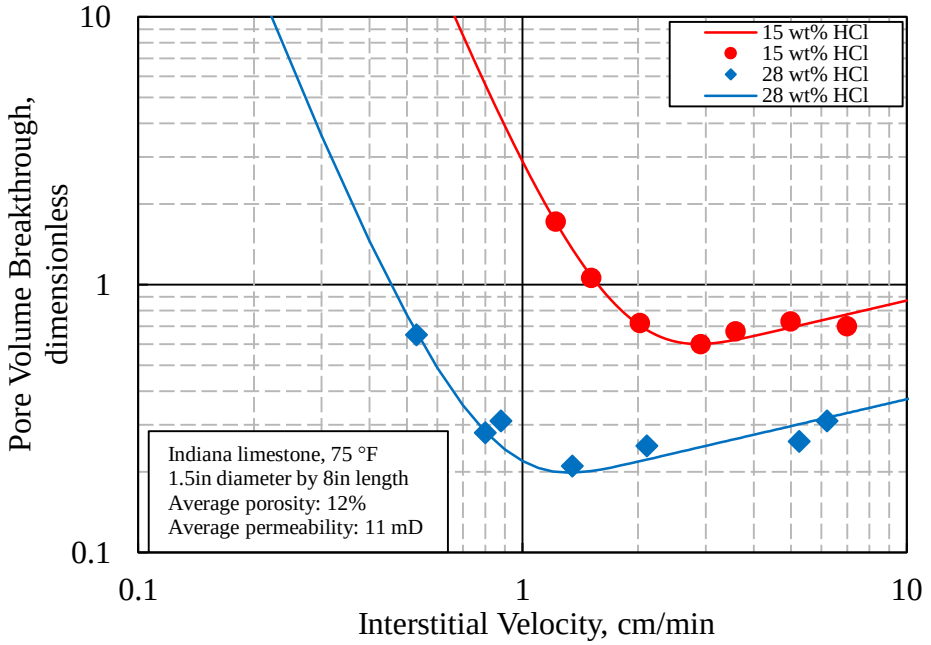

Fig. 3.10 Wormhole efficiency relationships of Indiana limestone for 15 wt% and 28 wt% HCl

Table 3.9 Optimal conditions in Fig. 3.10

C	$v_{i,opt}$	$PV_{bt,opt}$	$v_{wh,opt}$	N_{ac}	$v_{i,tip,opt}$
wt%	cm/min		cm/min		cm/min
15%	2.92	0.58	5.03	0.012	414.24
28%	1.35	0.19	7.11	0.024	295.30

A similar trend is also observed at high temperature. Furui et al. (2010) acidized Kansas Chalk using 15 wt% HCl and 28 wt% HCl at 150 °F and 200 °F respectively. As shown in both **Fig. 3.11** and **Fig. 3.12**, the $v_{i,opt}$ of 28 wt% HCl is less than that of 15 wt% HCl at both temperatures. The optimal conditions are shown in **Table 3.10** and **Table 3.11**.

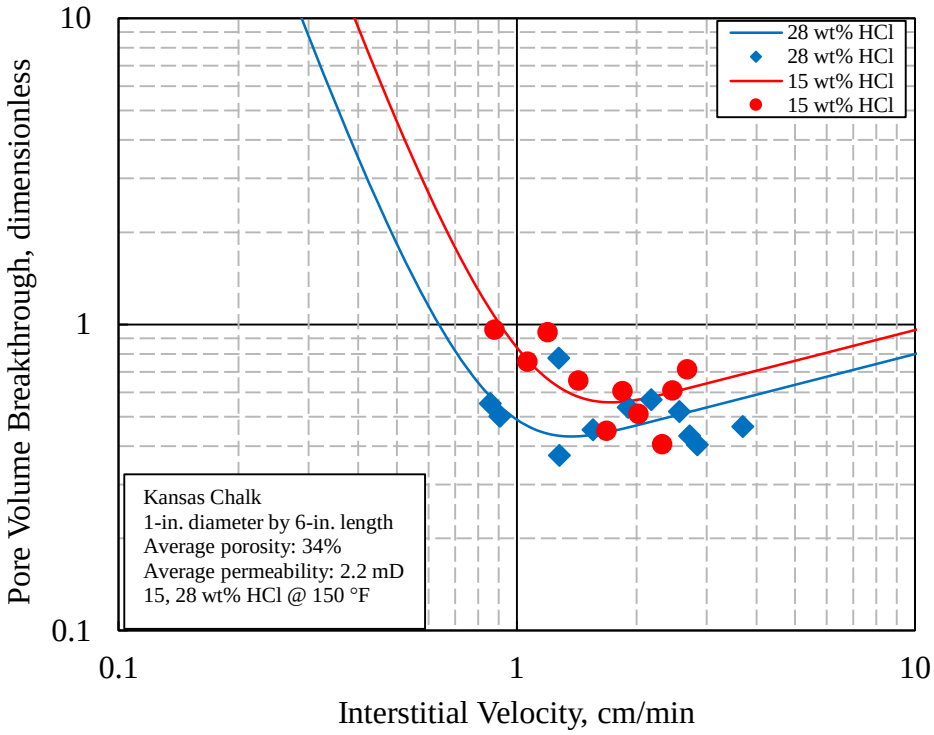

Fig. 3.11 Wormhole efficiency relationships of 15 wt% and 28 wt% HCl at 150 °F (Furui et al. 2010)

Table 3.10 Optimal conditions in Fig. 3.11

C	$v_{i,opt}$	$PV_{bt,opt}$	$v_{wh,opt}$	N_{ac}	$v_{i,tip,opt}$
wt%	cm/min		cm/min		cm/min
15%	1.76	0.54	3.26	0.042	77.79
28%	1.4	0.41	3.42	0.083	41.16

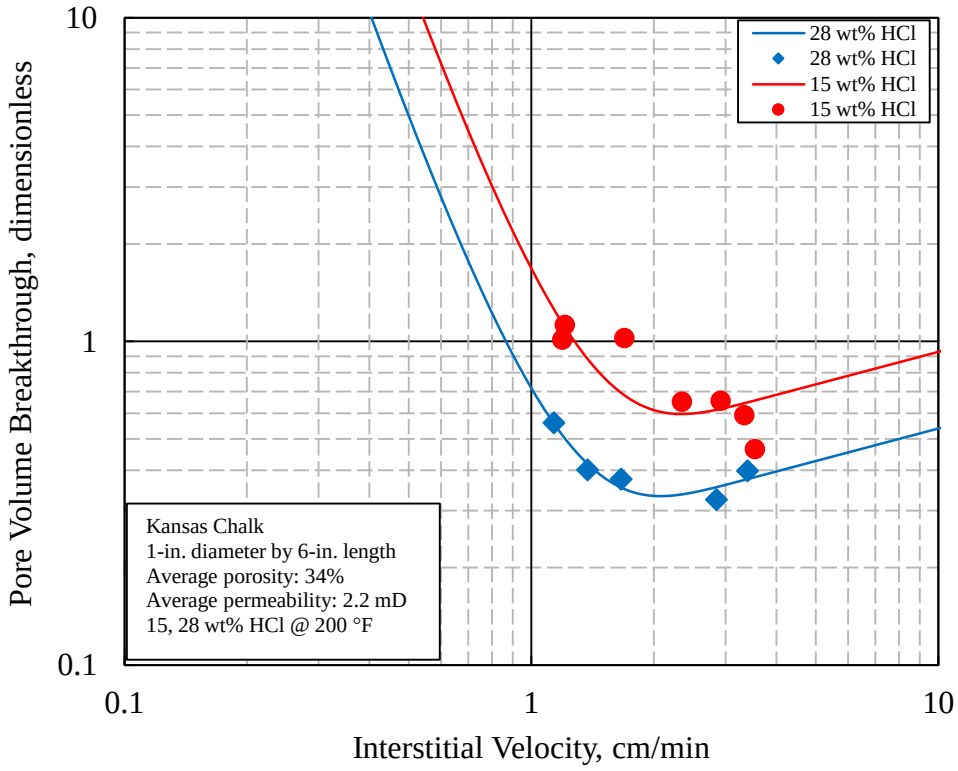

Fig. 3.12 Wormhole efficiency relationships of 15 wt% and 28 wt% HCl at 200 °F

(Furui et al. 2010)

Table 3.11 Optimal conditions in Fig. 3.12

C	$v_{i,opt}$	$PV_{bt,opt}$	$v_{wh,opt}$	N_{ac}	$v_{i,tip,opt}$
wt%	cm/min			cm/min	
15%	2.38	0.58	4.10	0.042	97.93
28%	2.12	0.32	6.63	0.083	79.86

As observed from the experimental results in the yellow columns above, if acid concentration is below 17.5 wt%, increasing acid concentration results in an increase of $v_{i,opt}$. If acid concentration is larger than 17.5 wt%, $v_{i,opt}$ decreases with increasing acid concentration. In the meanwhile, $PV_{bt,opt}$ always decreases with increasing acid concentration. From the calculated results in the green columns, we can see that the acid concentration has the same effect on $v_{i,tip,opt}$ as it does on $v_{i,opt}$. However, $v_{wh,opt}$ always increases with an increasing acid concentration.

3.4.2 Model-Based Explanation

In order to explain the concentration effect shown above, we focus on the wormhole tip interstitial velocity $v_{i,tip,opt}$. Through Eq. 3-46 below we can see, for a particular rock (fixed pore size distribution), the $v_{i,tip,opt}$ is linearly proportional to $\bar{v}_{p,\mathrm{mode},opt}$, with the proportional factor only related to rock pore properties. So we can conclude that at optimal conditions the $\bar{v}_{p,mode,opt}$ also increases with increasing acid concentration up to a certain concentration and then decreases.

$$v_{i,tip,opt} = \frac{\bar{v}_{p,\mathrm{mode},opt}}{A_{p,\mathrm{mode}}} \cdot \frac{\bar{L}_p M_2}{\phi} \tag{3-46}$$

In the meanwhile, the $\bar{v}_{p,\mathrm{mode},opt}$ is linearly proportional to the overall reaction rate coefficient for a particular rock through Eq. 3-47, and its proportional factor also depends only on rock pore properties. In this way, we can explain the acid concentration effect based on the overall acid/rock reaction in the mode-size pore.

$$\bar{v}_{p,\mathrm{mode},opt} = \frac{\kappa \bar{\Gamma}_{p,\mathrm{mode}} L_{p,\mathrm{mode}}}{A_{p,\mathrm{mode}}} \tag{3-47}$$

Harris et al. (1966) measured the overall HCl reaction rate with limestone for different concentrations. They found that the overall reaction rate is highest at concentration of 24 wt%. Beyond that, the overall reaction rate decreases due to high calcium ions concentration. These concentrated calcium ions decrease the diffusion rate of H^+. **Fig. 3.13** shows their experimental results.

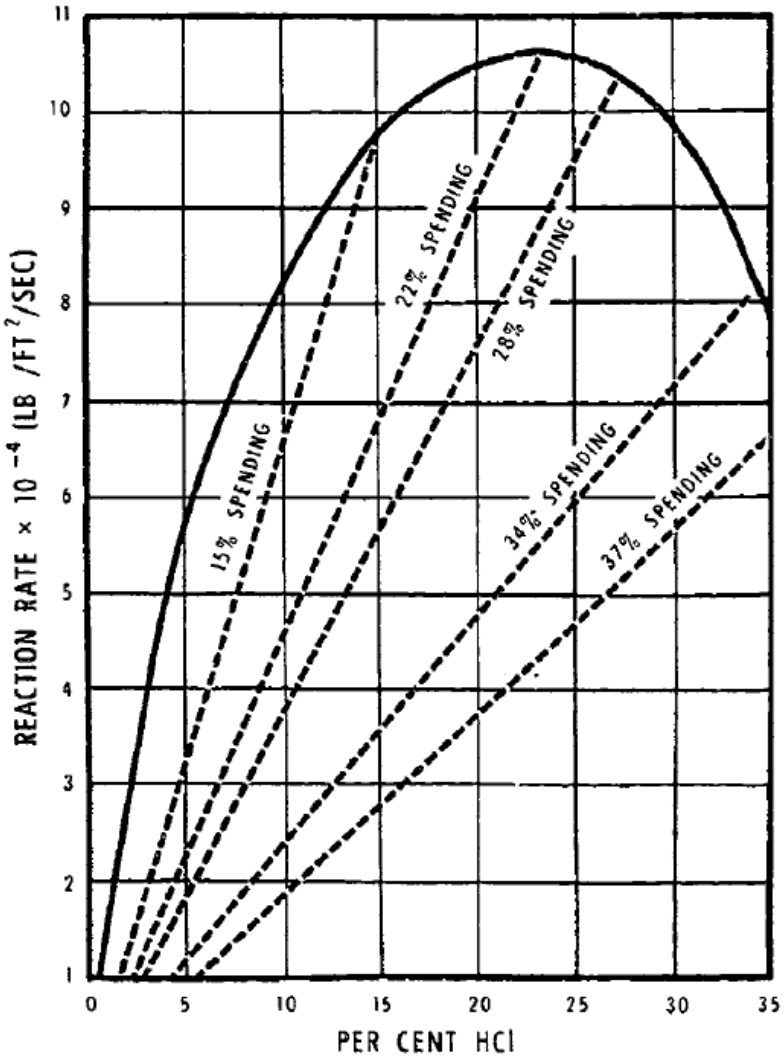

Fig. 3.13 Overall reaction rates for different HCl concentrations (Harris et al. 1966)

The overall reaction rate is calculated through $r = \kappa C_0$, which is linearly proportional to the bulk acid concentration. We can conclude that overall reaction rate coefficient κ has the highest value at 24 wt% concentration. From this experimental result and linear relationships of Eq. 3-46 and Eq. 3-47, we can explain the acid concentration

effect on the optimal conditions of acidizing coreflood experiments. The explanation procedure can be summarized in **Fig. 3.14** below.

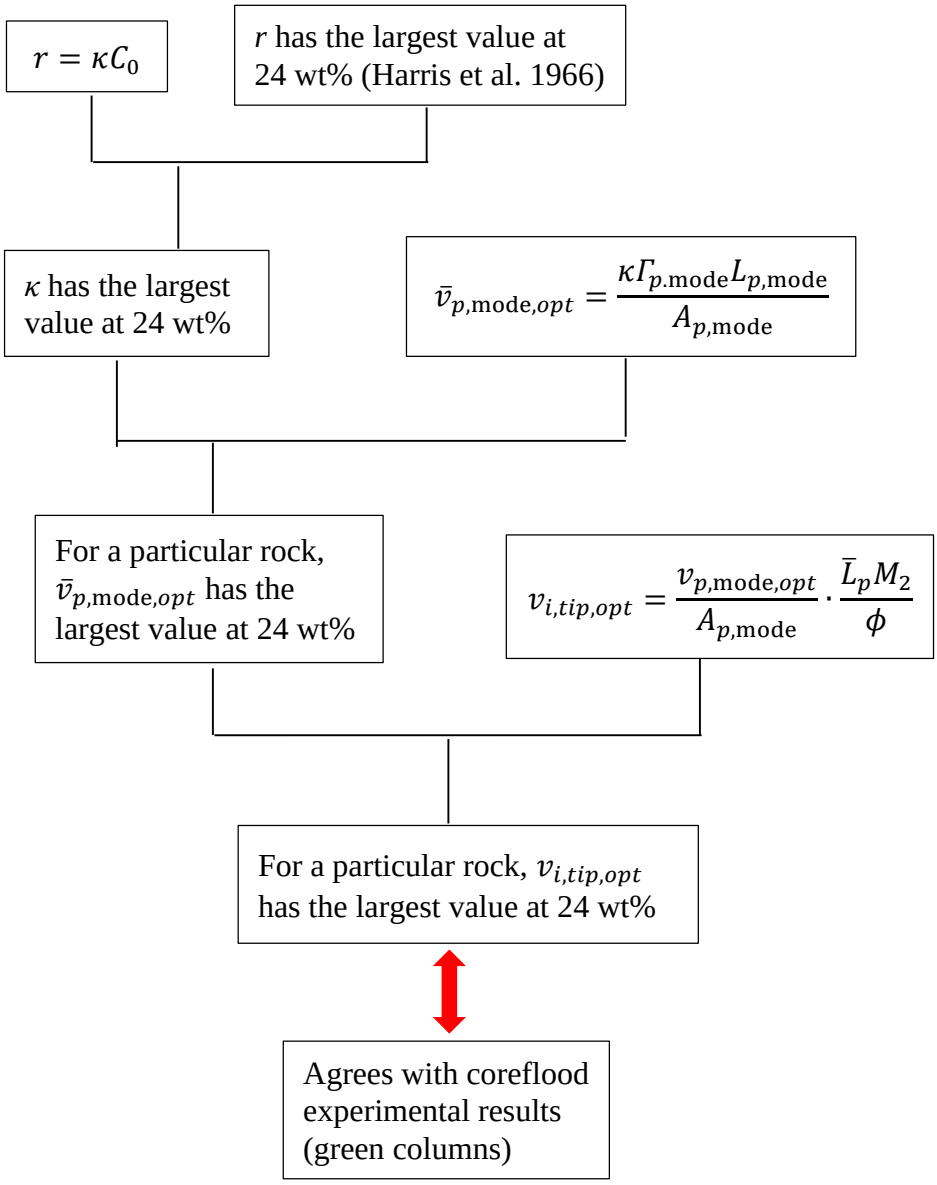

Fig. 3.14 Schematic description of acid concentration effect

In summary, if acid concentration is less than 24 wt%, increasing acid concentration results in an increase of $v_{i,opt}$. If acid concentration is larger than 24 wt%, it results in a decrease of $v_{i,opt}$. These can be explained based on our model. However, in order to fully quantify the concentration effect, the diffusion rates of both reactants and products need to be further investigated.

The $PV_{bt,opt}$ always decreases with increasing acid concentration, due to the increase of acid capacity number. If we plot the $PV_{bt,opt}$ with acid concentration in Table 3.6 and Table 3.7, we can find that the $PV_{bt,opt}$ decreases with a negative fraction order as acid concentration increases, as shown in **Fig. 3.15** and **Fig. 3.16**. Our model cannot explain this fraction order currently. Recent experimental study shows that $PV_{bt,opt}$ is related to the acid flow fraction of a rock (Zakaria et al. 2015), which is directly determined by the rock pore size distribution. The $PV_{bt,opt}$ calculation in our model is based on the linear flow relationship, and has nothing to do with flow fraction. Therefore, in order to have a correct prediction for $PV_{bt,opt}$, a relationship between flow fraction and pore size distribution needs to be developed.

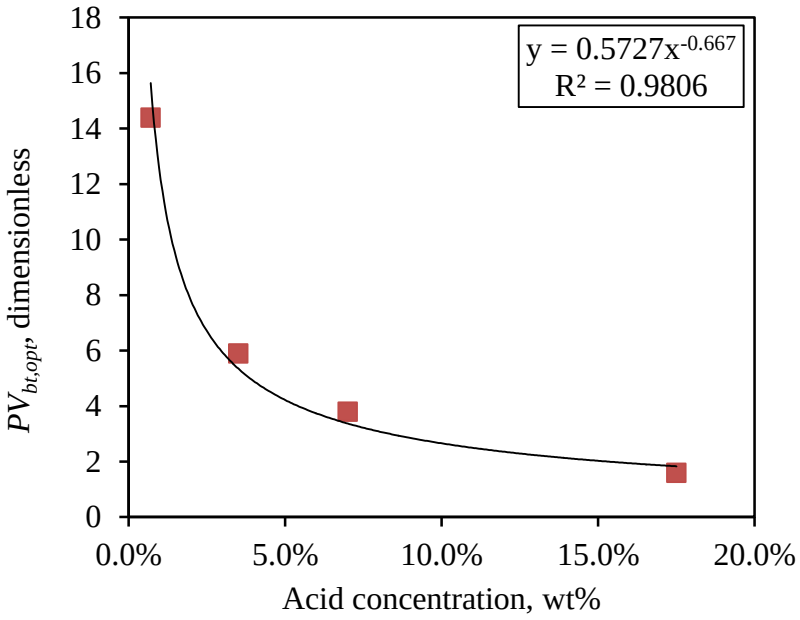

Fig. 3.15 Optimal breakthrough pore volume with acid concentration (Data of Table 3.6)

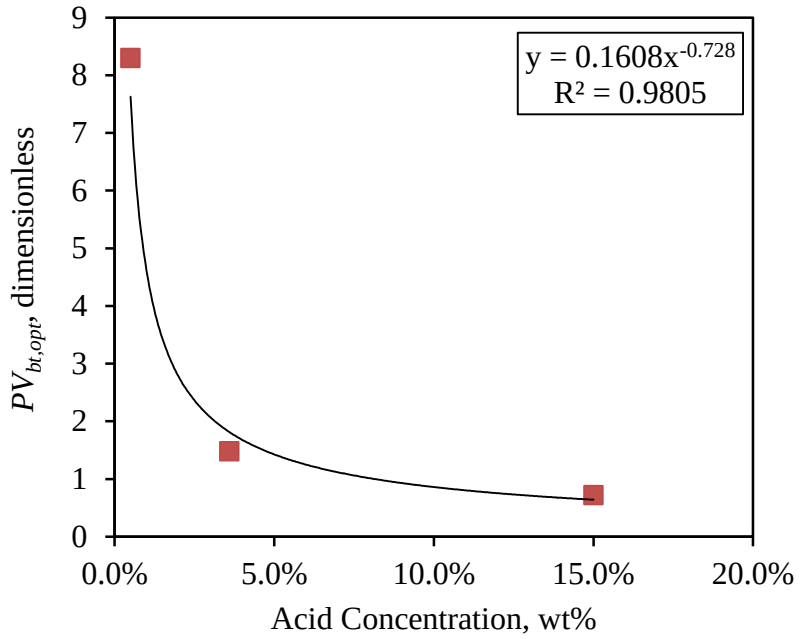

Fig. 3.16 Optimal breakthrough pore volume with acid concentration (Data of Table 3.7)

3.5 Effect of Pore-scale Heterogeneity

From previous experimental results, we can see that at the same experimental conditions, different types of limestone have different optimum conditions, although they have the same mineral composition. They differ with each other due to the difference of pore-scale heterogeneities (Ziauddin and Bize 2007).

An intuitive method to examine the pore-scale heterogeneity is through Thin Section Analysis. In this work, we examined the pore sizes and structures through thin sections for 11 different types of carbonate rocks, including 10 types of limestone and 1 type of dolomite. This section presents thin section images for three types of limestone that are commonly used in the lab experiments. **Fig. 3.17**, **3.18** and **3.19** show the thin section images for Indiana limestone (13 mD), Desert Pink limestone and Winterset limestone respectively. Other thin section images are presented in Appendix A.

From Fig. 3.17 we can see that Indiana limestone is a type of skeletal grainstone with distinctive calcitic vadose cements. Inter-granular pores are commonly seen with varying shapes and sizes. Some intra-granular porosity is also observed.

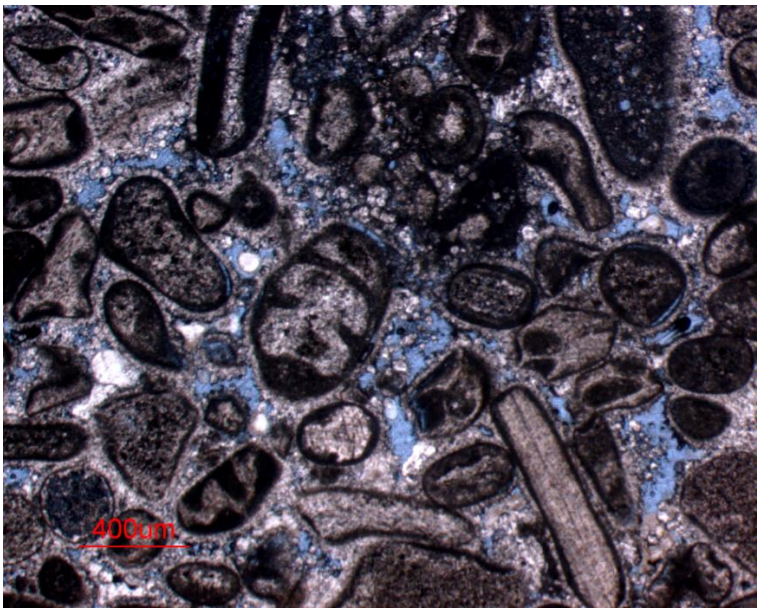

Fig. 3.17a Thin Section image for Indiana limestone (13 mD) with 10×Magnification

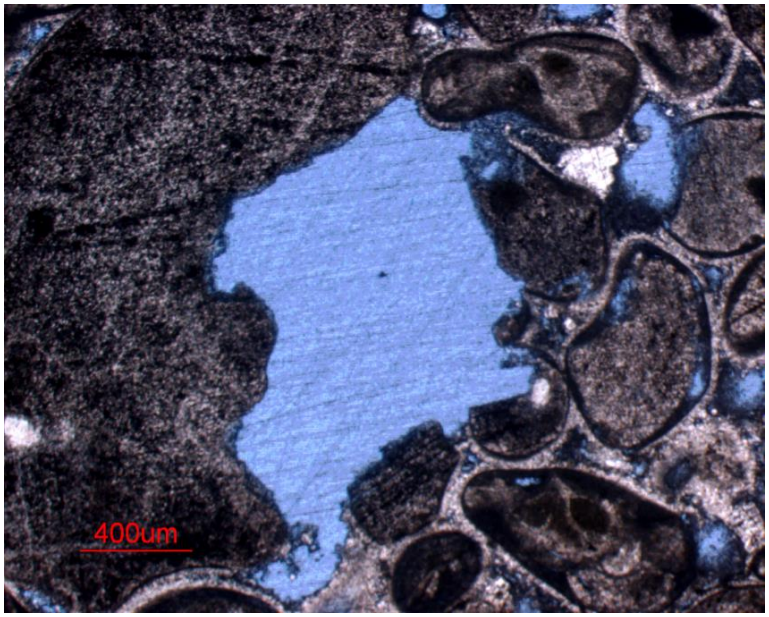

Fig. 3.17b Thin Section image for Indiana limestone (13 mD) with 20×Magnification

Fig. 3.18 shows that Desert Pink limestone is a type of calcitic grainstone with poorly developed intercrystal porosity of irregular shapes.

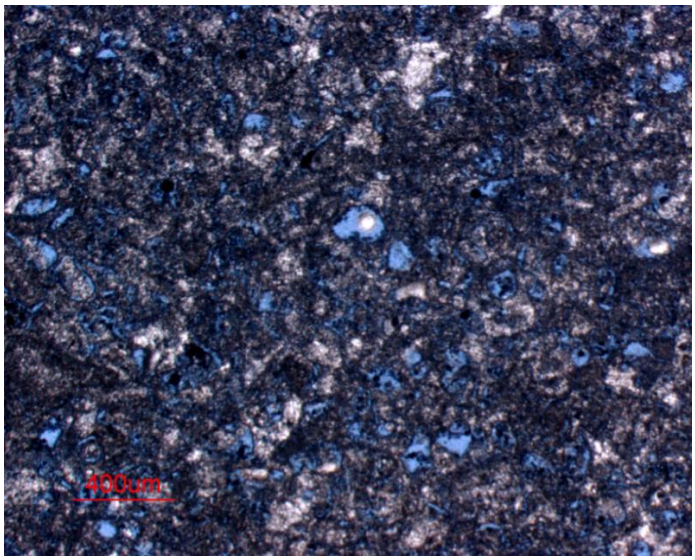

Fig. 3.18a Thin Section image for Desert Pink limestone with 10×Magnification

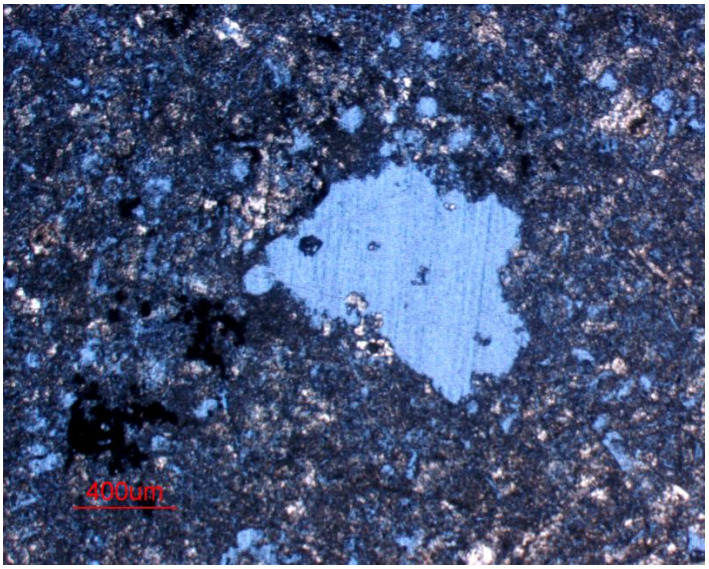

Fig. 3.18b Thin Section image for Desert Pink limestone with 20×Magnification

Fig. 3.19 shows that Winterset limestone is a type of oolitic grainstone that has undergone essentially complete porosity inversion during meteoric diagenesis. Primary porosity has been completely cemented by blocky calcite. Moldic pores are the dominant pore types but they are poorly connected.

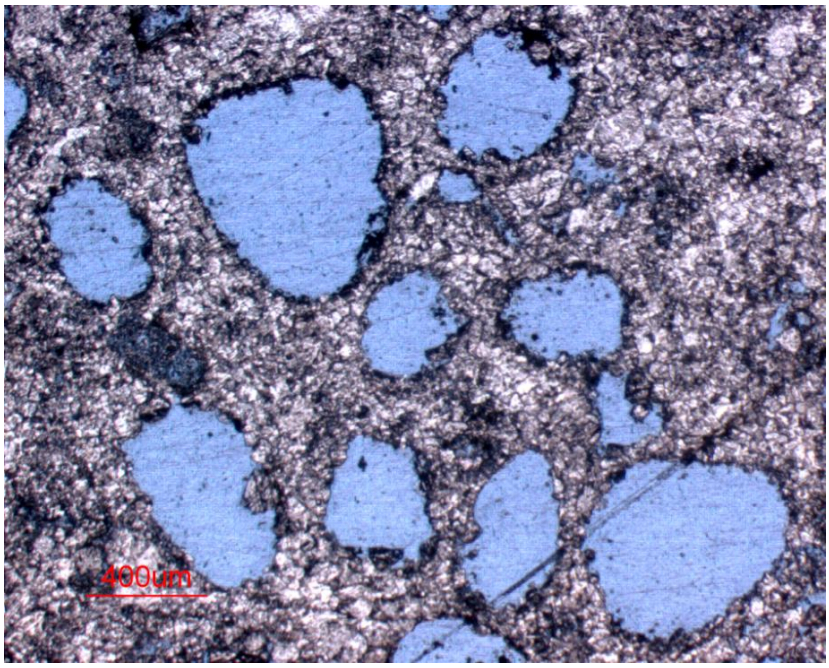

Fig. 3.19 Thin Section image for Winterset limestone with 10×Magnification

From the thin section images shown above, we can see the pore structures and sizes are different for each type of rock. Besides, for each individual type of rock, the pores also present varying sizes and connections. It is the difference of these pores that governs how acid flows inside the rock.

Thin Section Analysis provides a way for visual examination, but cannot quantify the heterogeneity of the rock. Pore size distribution measurement can give quantified analysis. The more homogeneous of the rock, the narrower of the distribution curve. In this case, the optimal breakthrough pore volume is larger. This is because the pore sizes for a homogeneous rock are close, and acid tends to flow into most pores with close ease at the wormhole tip. The heterogeneous rocks have wider distribution curves. It is easier for acid to flow into larger pores at the wormhole tip, leaving other small pores unattacked by acid. Therefore, the optimal breakthrough pore volume is small. This has been validated experimentally by Zakaria et al. (2015). He also used a flow fraction to describe the heterogeneity effect on acid breakthrough pore volume.

The effect of pore size distribution on the optimal acid interstitial velocity has not been clearly identified. From the model developed in Section 2, we can see the pore size distribution is involved in M_2 calculation. Different rocks produce different M_2, resulting in different optimal interstitial velocities at the wormhole tip. The sensitivity study on the pore size distribution are not carried out for this study. However, once the Micro-CT scan data are available for each type of rock, we can carry out detailed analysis for the pore size distribution effect.

4 UPSCALING LAB RESULTS TO FIELD SCALE

4.1 Introduction

Acidizing coreflood experiments with linear core plugs currently serve as a guide for field acidizing treatment design. However, scale effects should be taken into consideration while using lab results (Dong et al. 2014). Fundamentally, the scale effect comes from difference of flow geometries. The flow geometries in the field are typically radial flow and spherical flow during acidizing treatments, which cause fluid loss characteristics to be different with linear flow coreflood experiments.

As stated in Section 2, in order to propagate wormhole most efficiently, an optimal wormhole tip interstitial velocity with full acid strength needs to be maintained. This optimal wormhole tip interstitial velocity depends on acid/rock properties only, so it is believed to be general for both core scale and field scale.

4.2 Review of Field Treatments

Recently, horizontal wells with multiple isolated completion zones are widely used in carbonate reservoirs. In each isolated completion zone, matrix acidizing is used to stimulate the well. This section reviews two case studies and discusses their designs of the acid pumping schedule.

Kent et al. (2013) described the design and execution of a matrix acidizing job for an horizontal well in an offshore chalk reservoir. The well sketch is shown in **Fig. 4.1**. It is completed with uncemented liners. There are multiple stages, and neighboring stages

are isolated through packers. These packers provide effective hydraulic isolation during acid stimulation and future production. **Fig. 4.2** shows the sketch of a single stage. During the treatment, acids are pumped through the tubing to the tubing-liner annulus. Then, the acids dissolves the ports located on the liner and flows into the liner-wellbore annulus. From this annulus, the acids flow into the formation and create wormholes. For each stage being treated, the acids dos not flow into other stages due to the control valves located on the tubing. Therefore, the pumping schedule solely depends on the zone properties that is being treated.

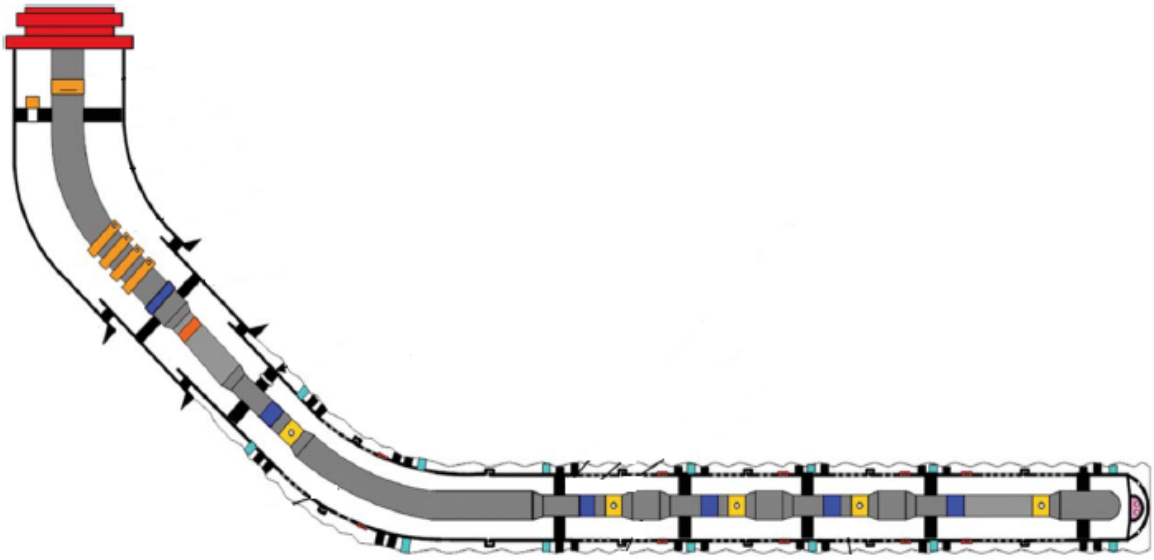

Fig. 4.1 Sketch of the well with multiple stages isolated by packers

(Kent et al., 2013)

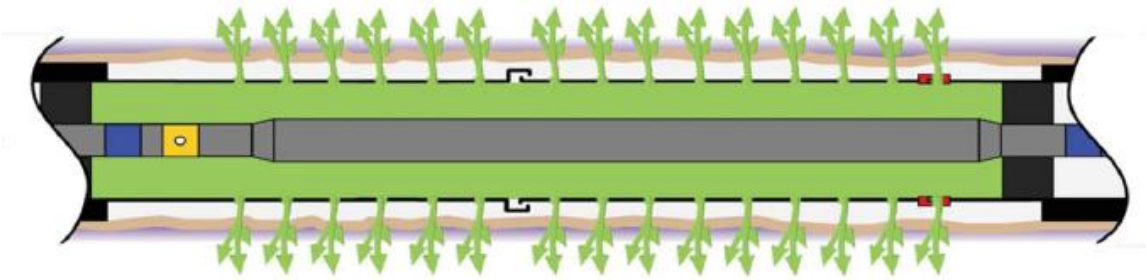

Fig. 4.2 Sketch of a single treatment stage (Kent et al., 2013)

Fig. 4.3 shows the acid treatment data with time for a particular zone. The red curve is the acid pumping rate with time. In the time interval between 515 min and 535 min, the acid pumping rate continuously increases, from around 30 bpm to 60 bpm. The pumping pressure at the reservoir face is kept below the fracture closure pressure.

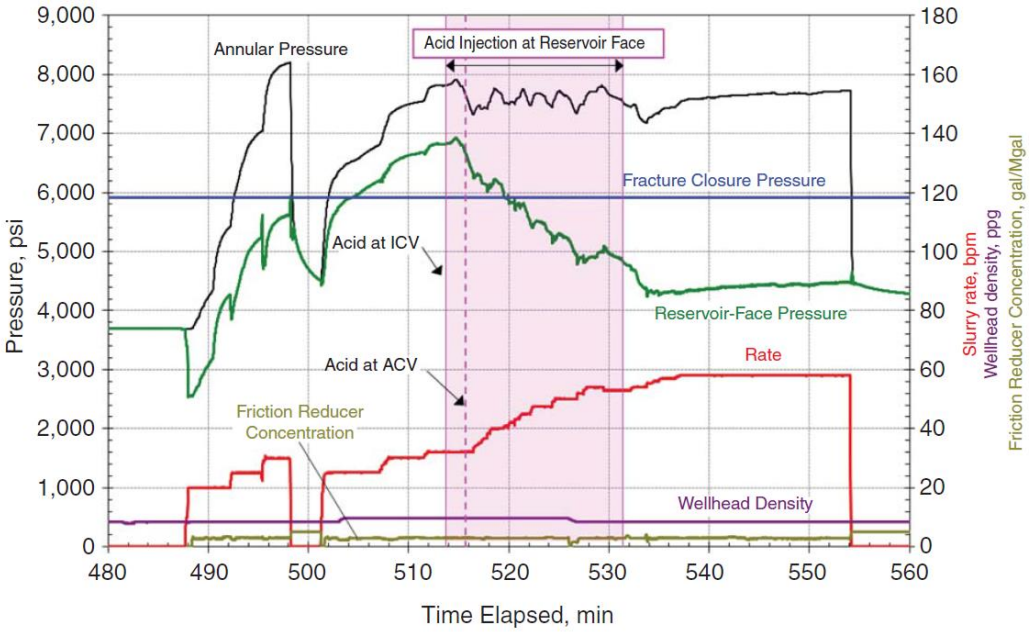

Fig. 4.3 Acid pumping schedule for a particular zone (Kent et al., 2013)

In this work, they did not show acidizing coreflood experimental tests, so we cannot see if there is any upscaling procedure involved. However, they reported that their target acid pumping rate is 60 bpm. Before that, the acid pumping rate needs to continuously increase up to the target rate. The treatment finishes when the pre-designed acid volume is reached.

Another treatment study was carried out by Domelen et al. (2011). A horizontal well was drilled in an offshore chalk reservoir, penetrating through three zones, as shown in **Fig. 4.4**. Each zone was treated separately with acid.

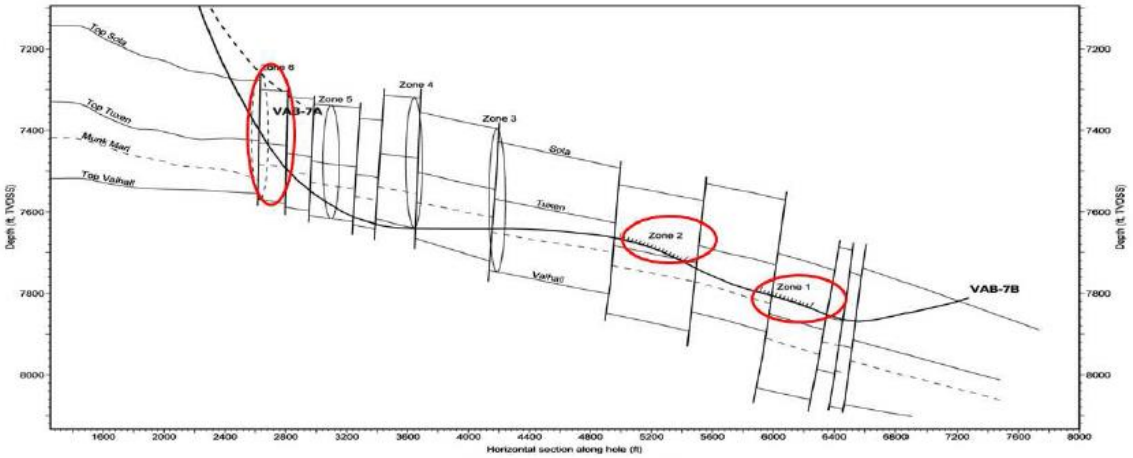

Fig. 4.4 Horizontal wellbore sketch with three zones penetrated

(Domelen et al. 2011)

Fig. 4.5 below shows the main acid treatment data with time. The blue curve is the acid pumping rate, and the black curve is the treatment pressure at the formation face. The

main acid treatment lasts about three and a half hours (from around 16:30 to 20:00). During the treatment, the acid pumping rate continuously increases.

Before the treatment, they did acidizing coreflood experiments with downhole core plugs. Their purpose is to find the proper type of acid. They did not upscale the lab optimal acid injection rate to the field scale.

In this treatment, they pumped the acid at the maximum allowable pumping rate, and the treating pressure is kept below the formation fracturing pressure. Before the treatment, they did formation step rate test to get the formation fracturing pressure, which is 7000 psi in their study. As we can see in Fig. 4.5, the black curve is always maintained below and close to the formation fracturing pressure (7000 psi).

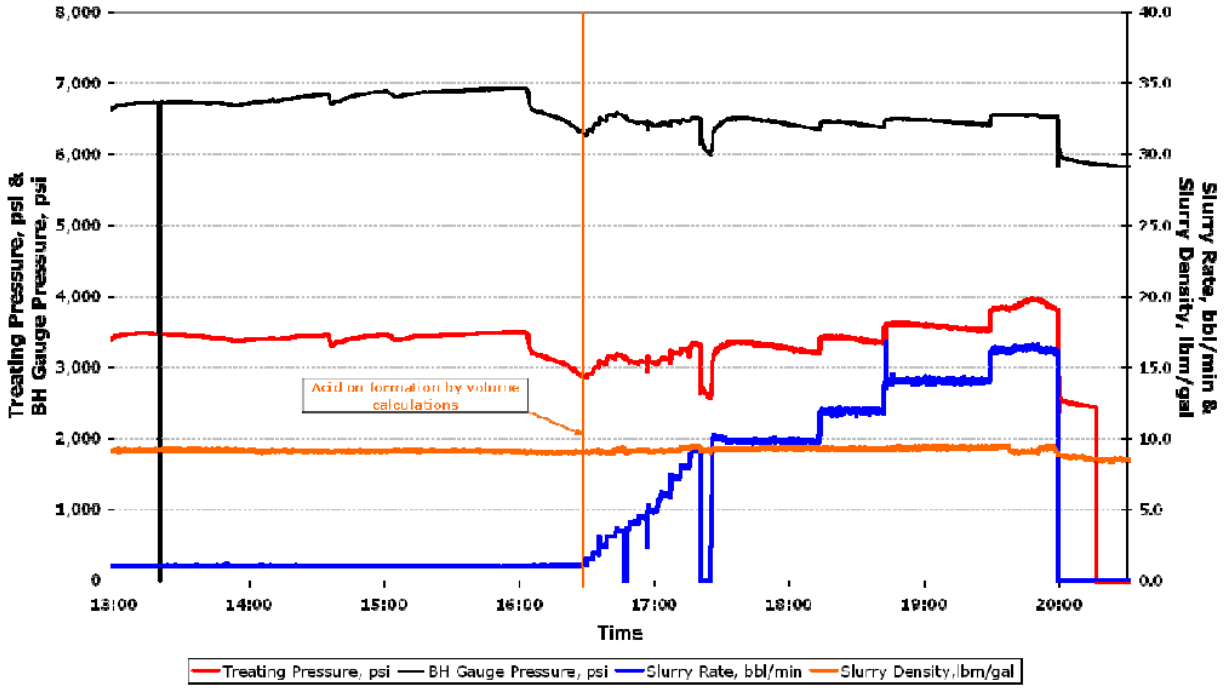

Fig. 4.5 Main acid treatment data with time for a particular zone (Domelen et al. 2011)

From the two case studies, we can see that the acid pumping rate generally increases during the treatment. However, the maximal pumping rate is usually used instead of the optimal pumping rate. This causes more horsepower requirement and waste of acid.

4.3 Upscaling Methods

The method developed in this study first calculates the optimal wormhole tip interstitial velocity. Then, a semi-empirical flow correlation previously developed is utilized to correlate the acid pumping rate with the optimal wormhole tip interstitial velocity.

There are two methods available to calculate the optimal wormhole tip interstitial velocity. The first method is through our model developed in Section 2. Once rock pore size distribution and acid type are determined, $v_{i,tip,opt}$ can be calculated through Eq. 2-57. Another method is based on the linear acidizing coreflood experimental results. In this section, we focus on the second method.

This method is through linear acidizing coreflood experiments. Optimal conditions are obtained by curve fitting experimental data with Buijse and Glasbergen's model. The average wormhole propagation velocity is the ratio of $v_{i,opt}$ and $PV_{bt,opt}$. With Hung's model, the optimal wormhole tip interstitial velocity can then be calculated. A calculation example is shown below. The input optimal parameters come from one set of our acidizing coreflood experiments with Desert Pink limestone. The experimental results are shown in **Fig. 4.6**.

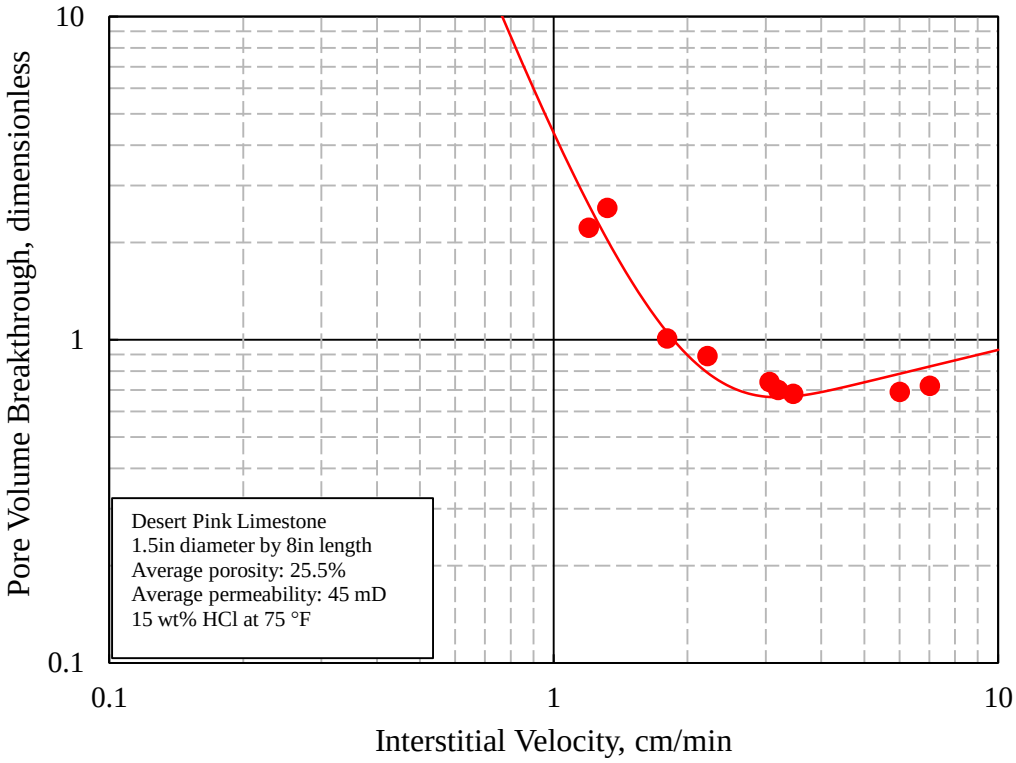

Fig. 4.6 Wormhole efficiency relationship of Desert Pink limestone at 75 °F

(Etten, 2015)

From the experiments, the $v_{i,opt}$ is 3.25 cm/min and the $PV_{bt,opt}$ is 0.64. The average wormhole propagation velocity is calculated below.

$$\bar{v}_{wh,opt}\big|_{75F} = \frac{v_{i,opt}}{PV_{bt,opt}} = \frac{3.25\text{cm/min}}{0.64} = 5.08\text{cm/min} \tag{4-1}$$

The acid capacity number for Desert Pink limestone is calculated as

$$N_{ac} = \frac{\phi\beta_{wt\%}\rho_a}{(1-\phi)\rho_r} = \frac{25.5\% \cdot (1.37 \cdot 15\%) \cdot (1.07\text{g/cm}^3)}{(1-25.5\%) \cdot (2.71\text{g/cm}^3)} = 0.0278 \tag{4-2}$$

Assuming the average wormhole propagation velocity equals to the instantaneous wormhole propagation velocity, the optimal wormhole tip interstitial velocity is calculated.

$$v_{i,tip,opt}\big|_{75F} = \frac{v_{wh,opt}\big|_{75F}}{N_{ac}} = \frac{5.08\text{cm/min}}{0.0278} = 182.73\text{cm/min} = 3.05\text{cm/s} \quad (4\text{-}3)$$

Note that the experiments shown in Fig. 4.6 were carried out at room temperature. So the $v_{wh,opt}$ and $v_{i,tip,opt}$ are also for room temperature. In order to upscale the lab results to field scale, the temperature effect on the optimal conditions needs to be adjusted first. Eq. 4-4 (Eq. 3-42 in Section 3) can be used for this.

$$\frac{v_{wh,opt1}}{v_{wh,opt2}} = \frac{D_1}{D_2} \quad (4\text{-}4)$$

The temperature of the reservoir to be studied is 200 °F. The diffusion coefficients for 75 °F and 200 °F are 3.53×10^{-5} cm^2/s and 9.93×10^{-5} cm^2/s respectively. So the $v_{wh,opt}$ and $v_{i,tip,opt}$ at the reservoir condition are

$$v_{wh,opt}\Big|_{200F} = \frac{D_{200F}}{D_{75F}} v_{wh,opt}\Big|_{75F} = \frac{9.93\times10^{-5}\text{cm}^2/\text{s}}{3.53\times10^{-5}\text{cm}^2/\text{s}} \times 5.08\text{cm/min} = 14.29\text{cm/min} \quad (4\text{-}5)$$

$$v_{i,tip,opt}\Big|_{200F} = \frac{v_{wh,opt}\big|_{200F}}{N_{ac}} = \frac{14.29\text{cm/min}}{0.0278} = 514.03\text{cm/min} = 8.57\text{cm/s} \quad (4\text{-}6)$$

During the acid treatment in the field, we need to maintain this optimal wormhole tip interstitial velocity with full acid strength. However, the acid concentration decreases along the wormhole due to the reaction between the acid and wormhole wall. So in order to make the wormhole propagate at the optimal condition, additional flow rate is needed to compensate for the acid concentration loss. Assuming the effective reaction surface area

is proportional to the wormhole length, the instantaneous optimal wormhole tip interstitial velocity is calculated by Eq. 4-7 (Furui et al. 2010).

$$v_{i,tip}(t) = v_{i,tip,opt} \cdot \frac{L_{wh}(t)}{L_{core}} \tag{4-7}$$

where L_{wh} is wormhole penetration length, and L_{core} is the core length. L_{core} is taken as 6 inches here to eliminate the core length effect (Dong et al. 2014).

In this way, the acid concentration loss can be approximated as

$$\frac{C_{tip}}{C_0} \approx \frac{L_{core}}{L_{wh}(t)} \tag{4-8}$$

The optimal wormhole propagation velocity is calculated by Eq. 4-9.

$$v_{wh} = v_{i,tip}(t)(\frac{C_{tip}}{C_0})N_{ac} = v_{i,tip}(t)(\frac{L_{core}}{L_{wh}(t)})N_{ac} \tag{4-9}$$

An example is illustrated to show the calculated pumping schedule.

A horizontal well is drilled in the center of a pay zone. The pay zone thickness is 50 ft. The well is cased and cemented. Five stimulation stages are identified based on the well logging data. Each stage is perforated at one shot per 10 ft. The perforations are orientated to the same direction. The stage length in this calculation example is 100 ft. The well sketch is shown in **Fig. 4.7**. The parameters related to the treatment are shown in **Table 4.1**.

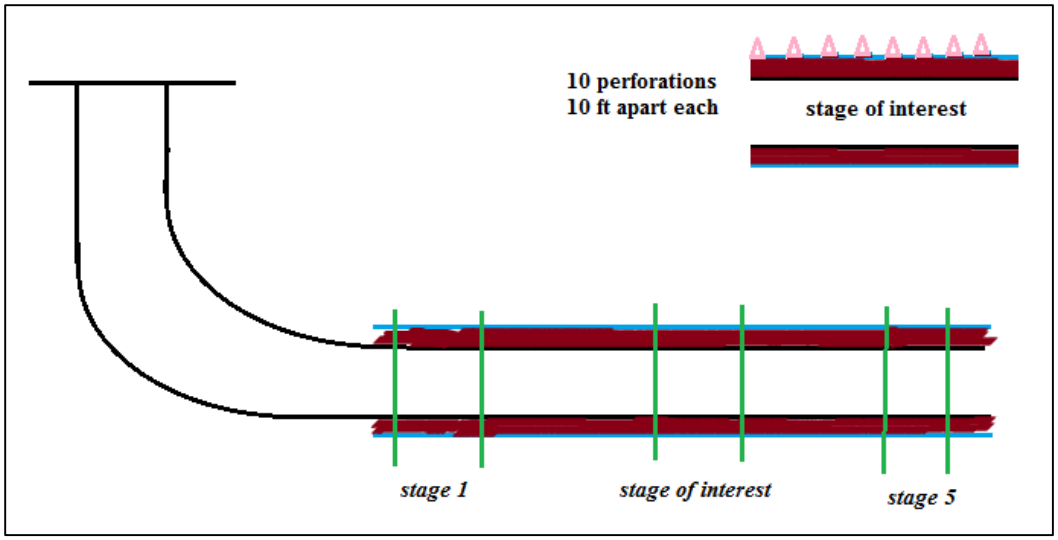

Fig. 4.7 Multi-stage limited entry completion of a horizontal well

Table 4.1 Reservoir and acid properties

Reservoir temperature	200	°F
Porosity	25.5%	
HCl concentration	15	wt%
Optimal wormhole tip interstitial velocity with full acid strength	8.57	cm/s
Acid capacity number	0.0278	
Wellbore radius	0.328	ft
Perforation depth	0.5	ft
Stage length	100	ft
Wormhole numbers per plane	6	
Wormhole diameter	2.5	mm

A semi-empirical flow equation is used to correlate wormhole tip interstitial velocity and acid pumping rate, shown as Eq. 4-10 (Furui et al. 2010).

$$v_{i,tip} = \frac{q}{\phi h\sqrt{\pi m_{wh}}}[(1-\alpha_z)\frac{1}{\sqrt{d_{e,wh}r_{wh}}} + \alpha_z(\frac{1}{d_{e,wh}}) \tag{4-10}$$

where m_{wh} is wormhole numbers in a horizontal plane; α_z denotes wormhole axial spacing, and is taken as 0.75 in this case. The calculation procedure is shown below.

At the beginning of the acid injection, acid flows through the perforation and arrives at the formation. At this time, the wormhole is not created. L_{wh} equals to the perforation length and r_{wh} equals to the wellbore radius plus the perforation length. The acid pumping rate is calculated as follows.

$$L_{wh}(t_1) = L_{perf} = 0.5\text{ft} \tag{4-11}$$

$$v_{i,tip,opt}(t_1) = v_{i,tip,opt}\frac{L_{wh}(t_1)}{L_{core}} = 8.57\text{cm/s}\,\frac{0.5\text{ft}}{0.5\text{ft}} = 8.57\text{cm/s} = 16.87\text{ft/min} \tag{4-12}$$

$$v_{wh,opt}(t_1) = v_{i,tip,opt}(t_1)(\frac{L_{core}}{L_{wh}(t_1)})N_{ac} = 16.87\text{ft/min}\times 1\times 0.0278 = 0.469\text{ft/min} \tag{4-13}$$

$$r_{wh}(t_1) = r_{well} + L_{wh}(t_1) = 0.328\,\text{ft} + 0.5\text{ft} = 0.828\,\text{ft} \tag{4-14}$$

$$q = \frac{\frac{1\text{bbl}}{5.615\text{ft}^3}\cdot 16.87\text{ft/min}\cdot 25.5\%\cdot 100\text{ft}\cdot\sqrt{6\pi}}{[(1-0.75)\frac{1}{\sqrt{2.5\text{mm}\,\frac{0.00328\text{ft}}{1\text{mm}}\cdot 0.828\text{ft}}} + 0.75\frac{1}{2.5\text{mm}\,\frac{0.00328\text{ft}}{1\text{mm}}}]} = 3.52\text{bpm} \tag{4-15}$$

In the next time step, the wormhole penetrated into the formation for a certain distance, Δr_{wh}. It is calculated as wormhole propagation velocity multiply by the time interval.

$$\Delta r_{wh}(t_1) = v_{wh,opt}(t_1)\Delta t = 0.469\text{ft/min} \times 1\text{min} = 0.469\text{ft} \tag{4-16}$$

The wormhole penetration radius and length in this time interval are

$$r_{wh}(t_2) = r_{wh}(t_1) + \Delta r_{wh}(t_1) = 0.828\,\text{ft} + 0.469\,\text{ft} = 1.297\,\text{ft} \tag{4-17}$$

$$L_{wh}(t_2) = L_{wh}(t_1) + \Delta r_{wh}(t_1) = 0.5\text{ft} + 0.469\,\text{ft} = 0.969\,\text{ft} \tag{4-18}$$

The wormhole tip interstitial velocity and wormhole propagation velocity are

$$v_{i,tip,opt}(t_2) = v_{i,tip,opt}\frac{L_{wh}(t_2)}{L_{core}} = 16.87\text{ft/min}\ \frac{0.969\text{ft}}{0.5\text{ft}} = 32.69\text{ft/min} \tag{4-19}$$

$$v_{wh,opt}(t_2) = v_{i,tip,opt}(t_2)(\frac{L_{core}}{L_{wh}(t_2)})N_{ac} = 32.69\text{ft/min} \times (\frac{0.5\text{ft}}{0.969\text{ft}}) \times 0.0278 = 0.469\text{ft/min} \tag{4-20}$$

The optimal acid pumping rate for the second time interval is

$$q = \frac{\frac{1\text{bbl}}{5.615\text{ft}^3} \cdot 32.69\text{ft/min} \cdot 25.5\% \cdot 100\text{ft} \cdot \sqrt{6\pi}}{[(1-0.75)\frac{1}{\sqrt{2.5\text{mm}\,\frac{0.00328\text{ft}}{1\text{mm}} \cdot 1.297\text{ft}}} + 0.75\frac{1}{2.5\text{mm}\,\frac{0.00328\text{ft}}{1\text{mm}}}]} = 6.87\text{bpm} \tag{4-21}$$

This process is repeated until the target acid volume is reached. **Table 4.2** shows the calculated treatment data with time. The acid pumping schedule is plotted in **Fig. 4.8**.

Table 4.2 Calculated treatment data with time

Time	r_{wh}	$v_{i,tip,opt}$	$v_{wh,opt}$	q
min	ft	cm/min	cm/min	bpm
2	1.30	32.72	0.47	6.87
4	2.24	64.41	0.47	13.61
6	3.18	96.10	0.47	20.38
8	4.12	127.79	0.47	27.15
10	5.05	159.49	0.47	33.93
12	5.99	191.18	0.47	40.72
14	6.93	222.87	0.47	47.51
16	7.87	222.87	0.47	47.51
18	8.81	222.87	0.47	47.51
20	8.81	0.00	0.00	0.00
22	8.81	0.00	0.00	0.00
25	8.81	0.00	0.00	0.00

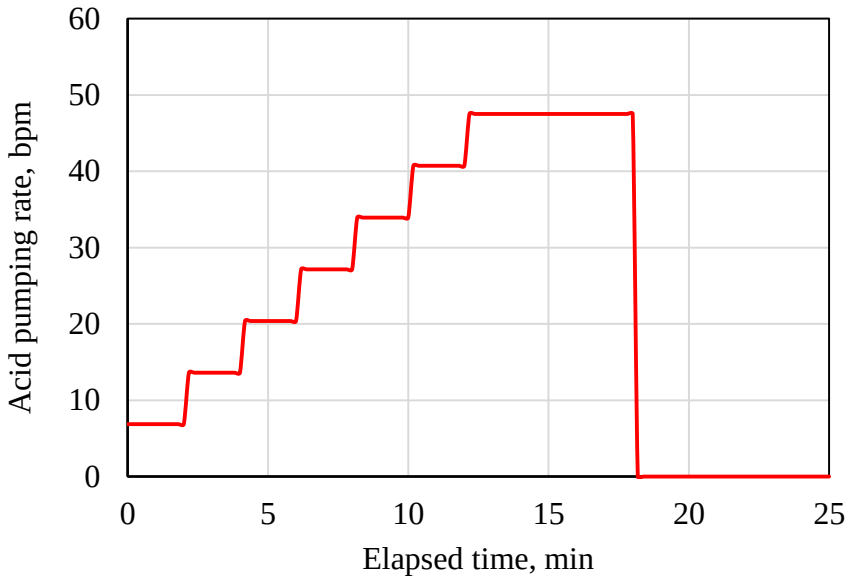

Fig. 4.8 Treatment schedule from our model

Compared with other design methods, the optimal wormhole tip interstitial velocity with full acid strength is the basis for an optimal field treatment design. This optimal wormhole tip interstitial velocity can be obtained both through our model developed in Section 2 and the acidizing coreflood experimental results.

4.4 Design Method for Limestone Reservoir

As we have seen from the field treatment example above, the acid pumping rate needs to be increased continuously through the whole treatment. So there is no a fixed optimal pumping rate for a particular treatment. The design method in this section focuses on the optimal wormhole tip interstitial velocity. When it is used for field treatment, we can use the upscaling technique described in this section to upscale the particular optimal wormhole tip interstitial velocity.

Eq. 3-42 describes the instantaneous wormhole propagation velocity is proportional to the acid diffusion coefficient, and is brought here as Eq. 4-22.

$$\frac{v_{wh,opt1}}{v_{wh,opt2}} = \frac{D_1}{D_2} \tag{4-22}$$

Hung's model is used to correlate the instantaneous wormhole propagation velocity and the wormhole tip interstitial velocity. For acid with full strength, Eq. 4-23 is used.

$$v_{wh,opt} = v_{i,tip,opt} N_{ac} \tag{4-23}$$

Substituting Eq. 4-23 into Eq. 4-22, we can get Eq. 4-24.

$$\frac{v_{i,tip,opt-T1}}{v_{i,tip,opt-T2}} = \frac{D_{T1}}{D_{T2}} \tag{4-24}$$

Eq. 4-24 is the basis for our treatment design method. Take the Desert Pink for example. The optimal wormhole tip interstitial velocity is 3.05 cm/s at 75 °F for 15 wt% HCl. The diffusion coefficient for 15 wt% HCl at 75 °F is 3.53×10^{-5} cm^2/s. Substituting the corresponding values into Eq. 4-24, we can have Eq. 4-25, and furthermore Eq. 4-26.

$$\frac{v_{i,tip,opt-T1}}{3.05\text{cm/s}} = \frac{D_{T1}}{3.53\times10^{-5}\text{cm}^2/\text{s}} \tag{4-25}$$

$$v_{i,tip,opt} = 8.6\times10^{4} D \tag{4-26}$$

where $v_{i,tip,opt}$ is in cm/s and D is in cm^2/s. If $v_{i,tip,opt}$ is in ft/min, Eq. 4-26 becomes Eq. 4-27.

$$v_{i,tip,opt} = 1.69\times10^{5} D \tag{4-27}$$

Eq. 3-15 for diffusion coefficient is brought here as Eq. 4-28 below.

$$D(H^+) = \exp(-\frac{2918.54}{T} + 0.0452[H^+] - 4.995) \tag{4-28}$$

Based on Eq. 4-27 and Eq. 4-28, we can generate a treatment design chart for Desert Pink limestone with 15 wt% HCl, as shown in **Fig. 4.9**.

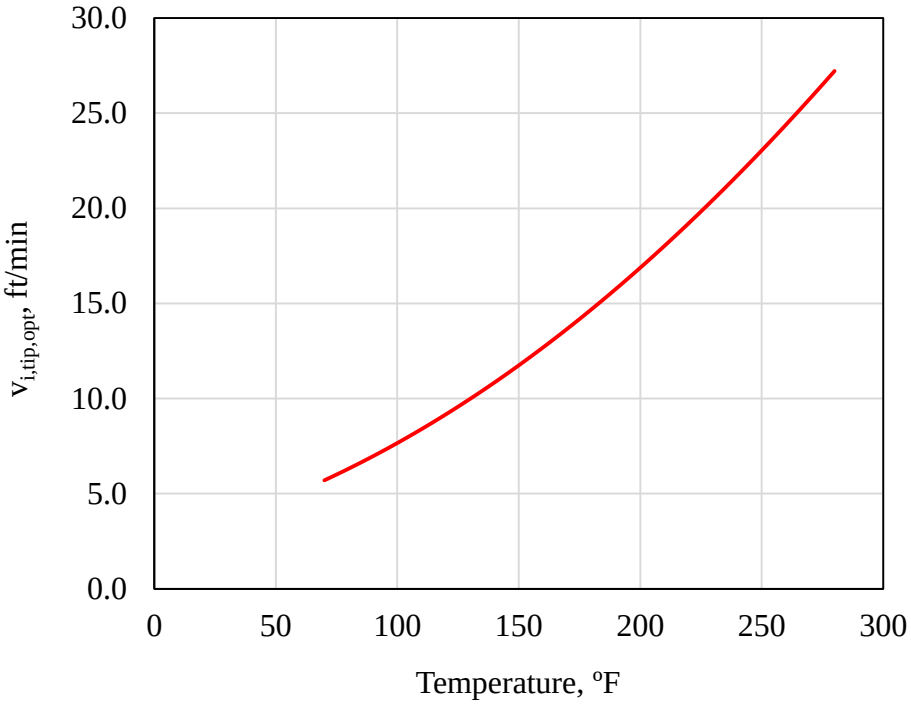

Fig. 4.9 Field treatment design chart for Desert Pink limestone of 15 wt% HCl

From Fig. 4.9, we can look up the optimal wormhole tip interstitial velocity with full acid strength. Then, we can use the upscaling technique described in this section for the field treatment design.

5 MODEL APPLICATION: ACIDIZING DESIGN FOR DOLOMITE FORMATIONS

5.1 Introduction

In previous sections, we have developed a comprehensive model to predict the optimal acid injection condition for both core scale and field scale. Sensitivity analysis was also studied based on this model. However, while analyzing temperature effect, we focused on the reaction between HCl and limestone, which in most cases is diffusion limited. Wormhole can also form when the overall reaction is mixed kinetics. Acidizing in dolomite formations is one example of mixed kinetics.

Very few acidizing coreflood experimental data of dolomite are reported in previous literatures, which makes it difficult to understand its behavior towards matrix acidizing. This is the reason we want to initiate the research in this section.

In this work, we cut a dolomite block from Silurian Formation in Thornton Quarry, Illinois. This block was drilled into core samples with dimensions of 1.5-in. diameter by 8-in long. We first measured the mineralogy of the rock samples to ensure the lithology to be studied. The test shows that more than 99% of the rock mineral is dolomite. In order to study the effectiveness of acidizing, we then did acidizing coreflood experiments with 15 wt% HCl at different temperatures. These temperatures are 72 °F, 122 °F, 185 °F and 260 °F. Wormhole efficiency relationships were generated and the optimal acid injection conditions were determined respectively from these experiments. The dissolution patterns created during each experiment was found by CT-scanning each

core after acid injection. The pore size distributions of the samples were measured using Nuclear Magnetic Resonance to help understand the optimal breakthrough pore volume.

Experimental results show that wormholes cannot be created at room temperature for dolomite rocks with a reasonable amount of acid. With an increase of temperature, wormholes can be formed with ease. The optimal acid interstitial velocity increases with increasing temperature. However, the rate of increase between 122 °F and 185 °F is significantly larger than the rate of increase between 185 °F and 260 °F. It is due to the difference of increase for acid diffusion rate and surface reaction rate, which is discussed in this section. Interestingly, unlike limestone, the corresponding optimal breakthrough pore volume decreases with increasing temperature between 122 °F and 185 °F, and increases slightly between 185 °F and 260 °F. This indicates if the reservoir temperature is low, more volume of acid is needed. Based on the experimental results and the upscaling method, a treatment design method is presented for dolomite formations at varying temperatures, which can be used for future references.

5.2 Pore Size Distribution

Before measuring the pore size distribution, we did the mineralogy test for the samples. The test results show that that more than 99% of the rock mineral is dolomite. The raw measurement data is shown in Appendix B. The thin section image show that the dolomite studied has a medium to course crystalline replacement, as shown in **Fig. 5.1**.

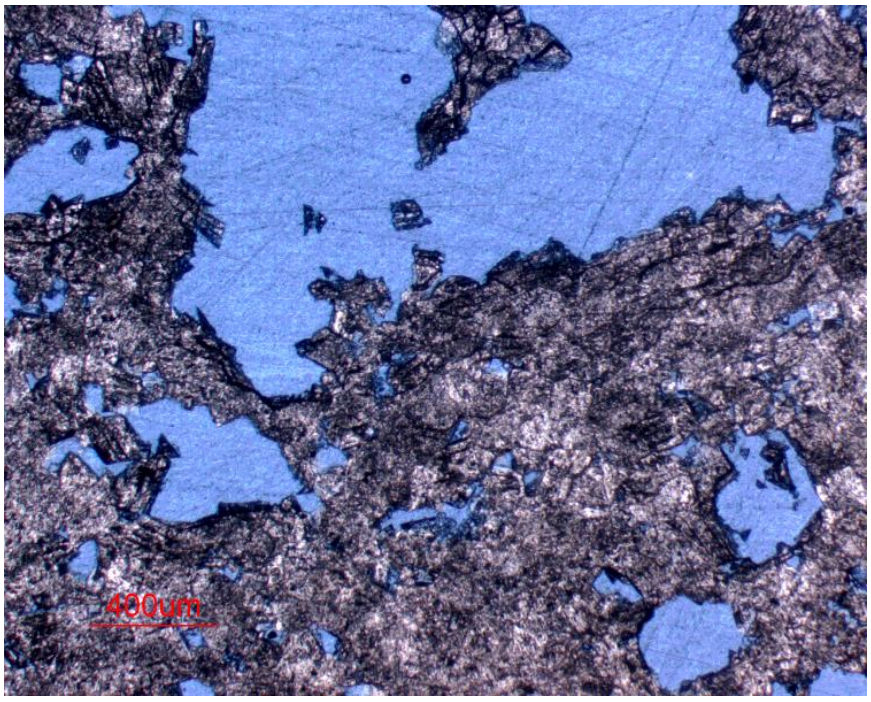

Fig. 5.1 Thin section image for dolomite

The pore size distribution is measured through Nuclear Magnetic Resonance (NMR). The apparatus used in this study is GeoSpec2 Core Analyzer, shown in **Fig. 5.2**. The measurements were conducted using a 2 MHz benchtop NMR spectrometer. The T_2 relaxation measurements were carried out using a CPMG (Carr-Purcell-Meiboom-Gill) pulse sequence. We set the inter-echo spacing time (TE) of the CPMG pulse sequence to 100 µsec. The signal-to-noise ratio (SNR) of the measurement was more than 200. The number of scans (NSA) depends on the total volume of fluid in the sample being measured.

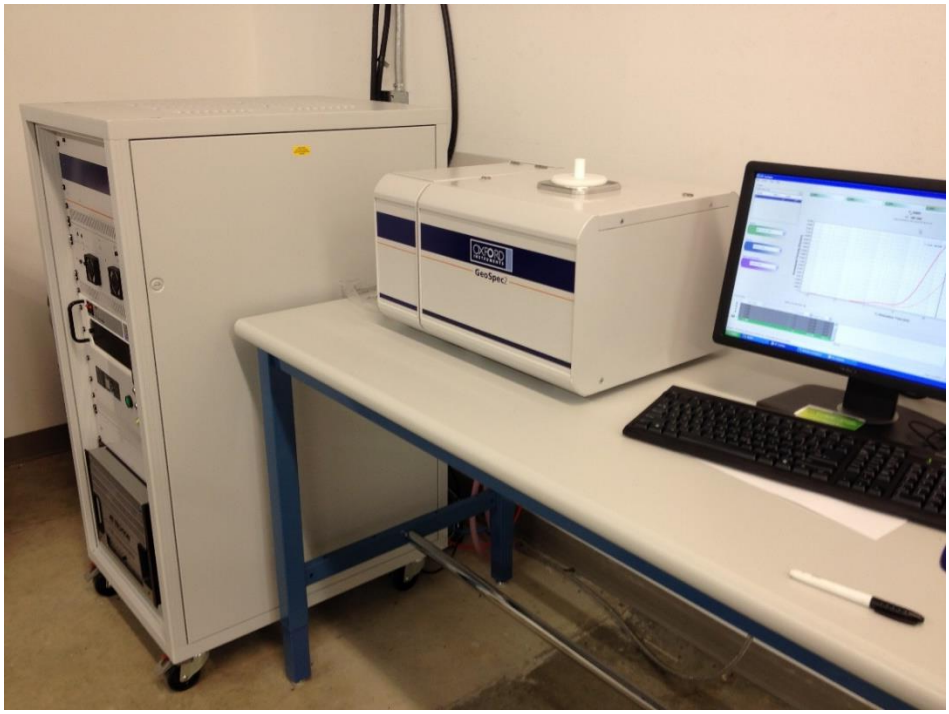

Fig. 5.2 Nuclear Magnetic Resonance apparatus

The dimension of the core samples for the NMR measurement are 1.5-in diameter by 1.5-in. long, and are fully water saturated through a vacuum pump before the measurement. The relationship between incremental porosity and transverse-relaxation-time (T_2) distribution was measured. For a rock fully saturated with water, the T_2 value of a single pore is proportional to the surface-to-volume ratio of the pore (George R. Coates, Lizhi Xiao and Manfred G. Prammer), as shown by Eq. 5-1.

$$\frac{1}{T_2} = \rho_2 \left(\frac{S}{V}\right)_{pore} \tag{5-1}$$

where ρ_2 is the surface relaxivity of T_2, which can be looked up for different minerals. For dolomite, it is 5.35 μm/s. S and V are the pore surface area and pore volume respectively.

Assuming the pores are cylindrical, the pore surface area and pore volume are calculated through Eq. 5-2 and Eq. 5-3.

$$S_p = 2\pi r_p L_p \tag{5-2}$$

$$V_p = \pi r_p^2 L_p \tag{5-3}$$

Substituting Eq. 5-2 and 5-3 into Eq. 5-1, we can see the T_2 is linearly proportional to the pore radius, as shown by Eq. 5-4.

$$\frac{1}{T_2} = \rho_2 \frac{2\pi r_p L_p}{\pi r_p^2 L_p} = \frac{2\rho_2}{r_p} \tag{5-4}$$

Therefore, for a particular rock, the distribution of T_2 is essentially the distribution of the pore radius.

In this study, we measured the pore size distribution for four different samples. These four samples are cut from the four corners of the dolomite block, as shown in **Fig. 5.3**. In this way, we can see if the change of the pore size distribution with position in the whole block is significant or not.

Fig. 5.4 shows the results generated by the NMR. We can see the total porosity of the four cores changes slightly, from around 10% to 12.2%. The mode value of T_2 for the four cores are almost the same, which is around 800 ms. This means the mode pore sizes of the four cores are the same, which can also be used for this whole dolomite block.

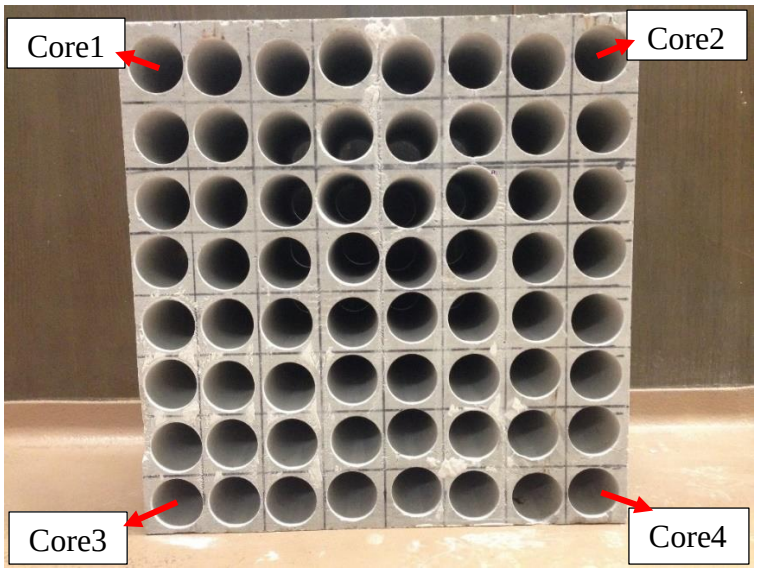

Fig. 5.3 Dolomite block for this study

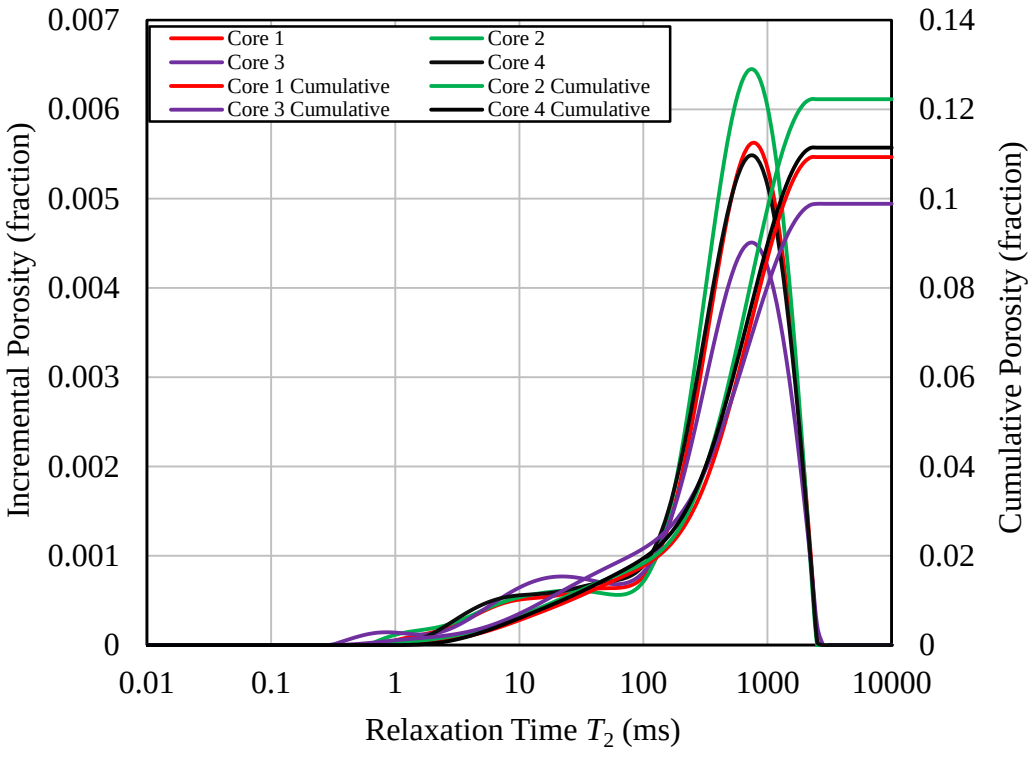

Fig. 5.4 Dolomite T_2 distribution

In order to get the pore size distribution, Eq. 5-4 is used. Each T_2 corresponds to a pore radius r_p. Take Core 1 for example. Its pore size distribution is shown in **Fig. 5.5**. We can see from the plot, the mode pore radius is 8 μm. Most of the pores have a radius between 2 μm to 20 μm.

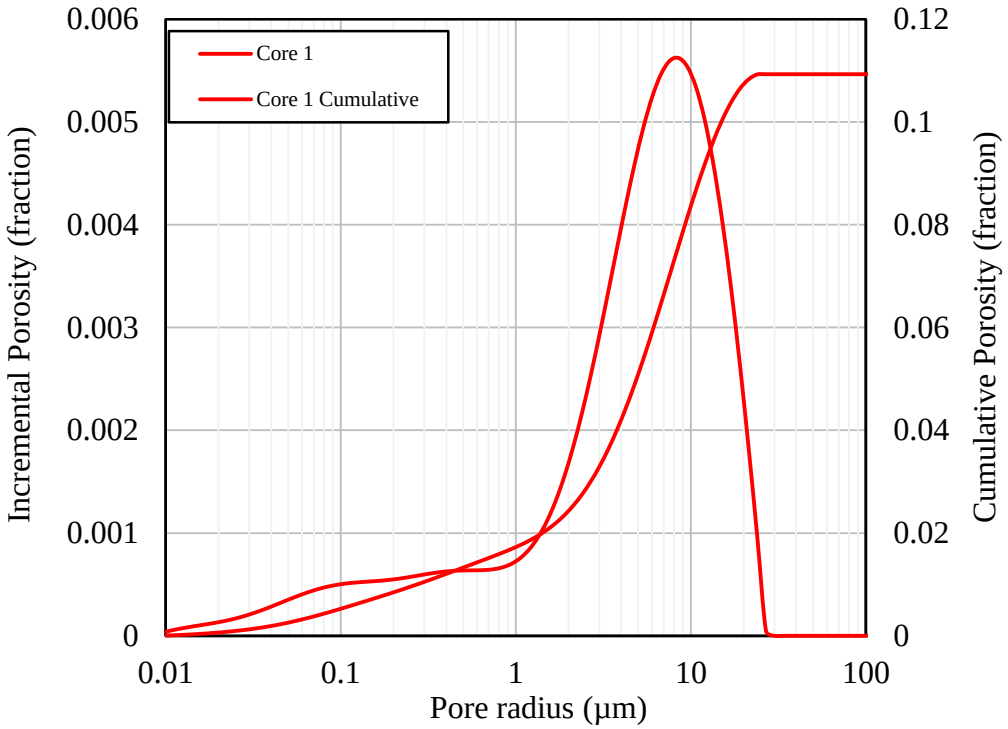

Fig. 5.5 The pore size distribution of the dolomite block

5.3 Acidizing Coreflood Experiment

Coreflood acidizing experiments were first carried out at room temperature. The inlet surface and outlet surface of an acidized core are shown in **Fig. 5.6** below. We can see that acid does not create wormholes throughout the core, but produces a spongy-like

surface. This is due to the low acid/rock surface reaction rate at room temperature. As has been discussed in Section 2, if the overall reaction is surface reaction limited, small pores and large pores tend to grow to a same size. It is verified by this set of experiment. In this case, wormholes do not form, and all the pores on inlet surface grow to a similar size.

Inlet surface Outlet surface

Fig. 5.6 Inlet and outlet surface of an acidized dolomite core at room temperature

In order to decrease the surface reaction limitation, experimental temperature was increased. We did another three sets of acidizing coreflood experiments, at 122 °F, 185 °F and 260 °F respectively. The three wormhole efficiency relationships are shown in **Fig. 5.7**. The optimal conditions are summarized in **Table 5.1**. The raw experimental data are shown in Appendix B.

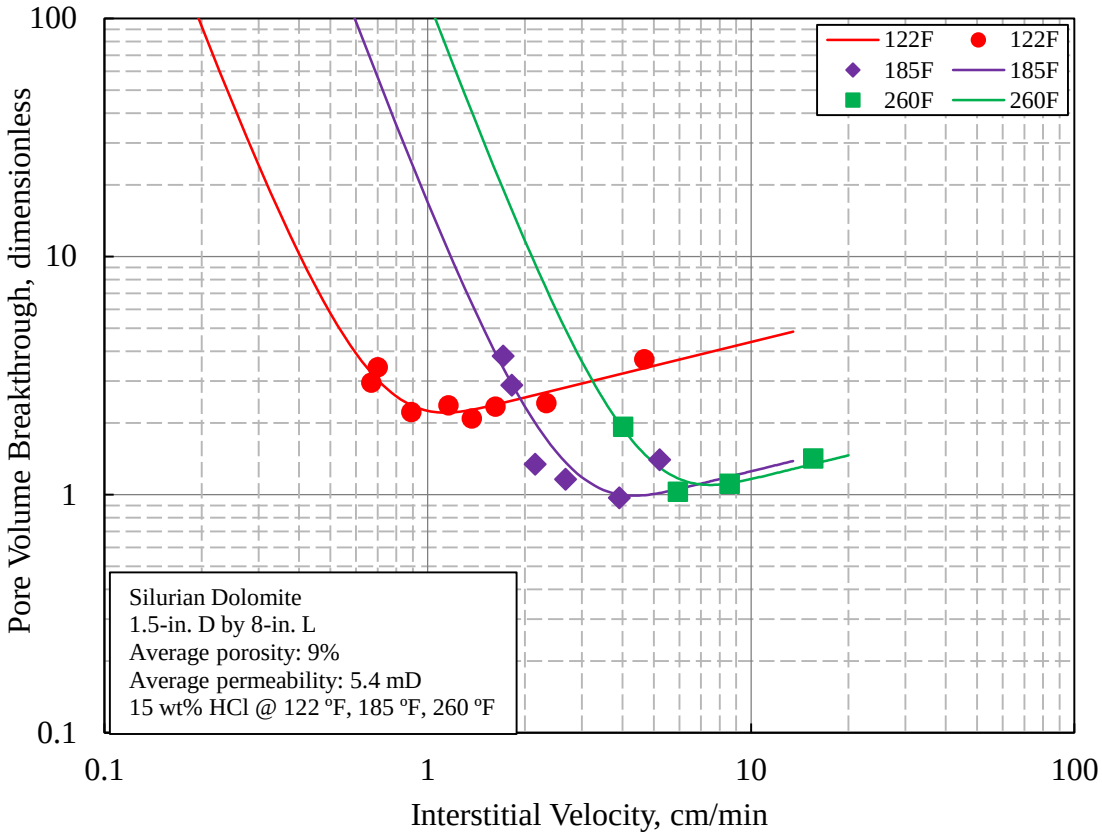

Fig. 5.7 Wormhole efficiency relationships of dolomite at 122 °F, 185 °F and 260 °F

Table 5.1 Optimal conditions in Fig. 5.5

Temperature, °F	$v_{i,opt}$, cm/min	$PV_{bt,opt}$	$v_{wh,opt}$, cm/min	$v_{i,tip,opt}$, cm/min
122	1.54	2.13	0.72	102.20
185	4.42	0.95	4.65	657.80
260	7.56	1.07	7.07	998.87

The yellow columns are experimental results, and the green columns are calculated results through Eq. 3-43, 3-44 and 3-45. The acid capacity number in this case is calculated by Eq. 5-5.

$$N_{ac} = \frac{\phi \beta_{15wt\%} \rho_a}{(1-\phi)\rho_r} = \frac{0.09 \times 1.27 \times 0.15 \times 1.07}{(1-0.09) \times 2.85} = 0.0071 \qquad (5\text{-}5)$$

Generally, the $v_{i,opt}$ increases with increasing temperature. However, unlike limestone, the $PV_{bt,opt}$ decreases from 122 °F to 185 °F, and increases slightly from 185 °F to 260 °F. Both $v_{wh,opt}$ and $v_{i,tip,opt}$ increase with increasing temperature. However, from 122 °F to 185 °F, the increase is significant.

5.4 Wormhole Structures from CT-Scanning

A Computed Tomography (CT) scanner is used to study the wormhole structures from the acidized cores. The scanner used is Toshiba Aquilion RXL 16-dector CT system, and is shown in **Fig. 5.8** below. During scanning, the sample is divided into multiple slices with a pre-determined thickness. Each slice contains CT numbers across the cross-sectional area. Larger CT number represents larger density while smaller CT number represents smaller density. Wormholes are detected as pixels with small CT numbers. The datasets are imported into an image processing software, and 3D wormhole images are produced.

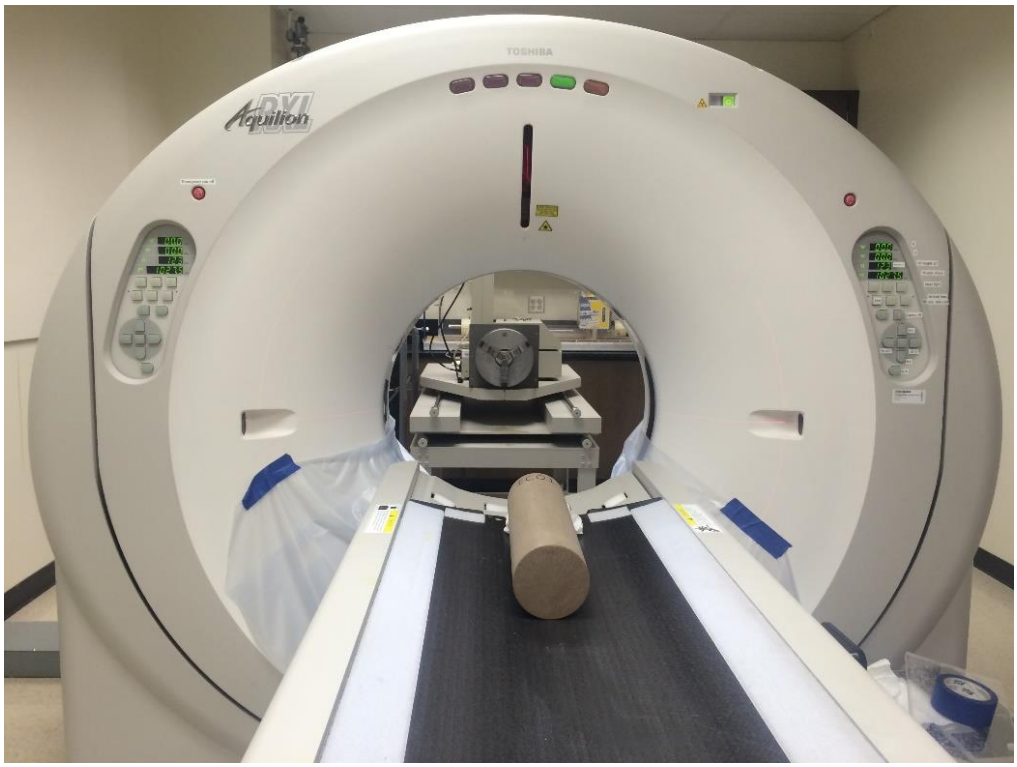

Fig. 5.8 Computed Tomography (CT) scanner used in this study

Fig. 5.9 below shows wormhole CT images for four acidized cores at 185 °F. From left to right, the acid interstitial velocities are 1.82 cm/min, 2.67 cm/min, 3.91 cm/min and 5.22 cm/min. As can be seen from this figure, at low acid interstitial velocity (image (1)), the wormhole is thick compared with structures at other three velocities. More acid is consumed to enlarge the wormhole diameter, and the corresponding breakthrough pore volume is larger, which is 2.88 for this image. As the acid interstitial velocity increases from 1.82 cm/min to 2.67 cm/min, the wormhole diameter becomes thinner, less acid is used when wormhole breaks though the core (1.16 pore volume).

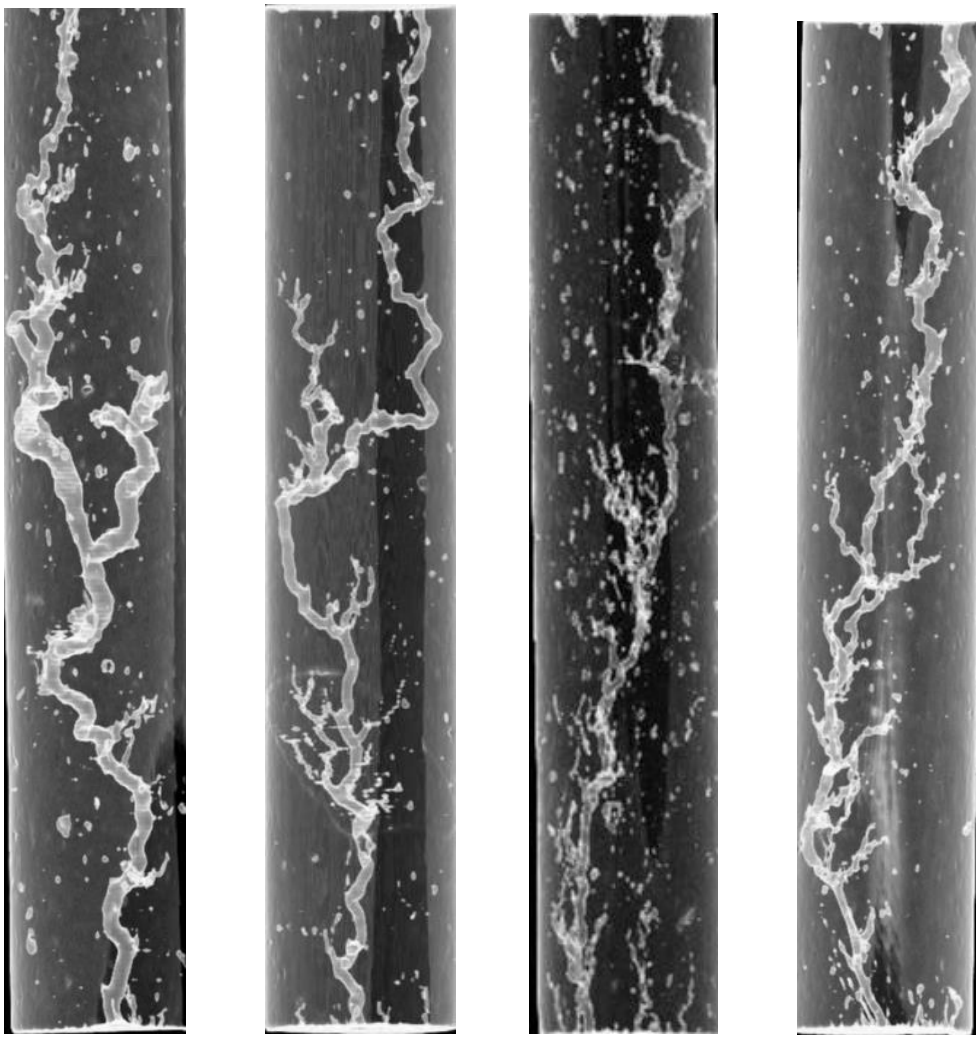

(1)	(2)	(3)	(4)
v_i = 1.82 cm/min	v_i = 2.67 cm/min	v_i = 3.91 cm/min	v_i = 5.22 cm/min
PV_{bt} = 2.88	PV_{bt} = 1.16	PV_{bt} = 0.97	PV_{bt} = 1.4

Fig. 5.9 Wormhole CT images for acidized dolomite cores at 185 °F

Image (4) shows the wormhole structure produced at higher acid interstitial velocity. The wormhole is thin compared with the left images, but a few wormhole branches are created along the dominant wormhole and extend to a certain distance. Not

only these branches consume acid, they can also change the local acid flow geometry and cause more acid loss to the surrounding rock. At this interstitial velocity, the acid is not wasted on enlarging wormhole diameter, but wasted on creating wormhole branches along the dominant wormhole. The corresponding breakthrough pore volume is relatively large, which is 1.4 for this image.

Image (3) in Fig. 5.9 shows the wormhole structure with the acid interstitial velocity close to the optimal. The wormhole is thin with minor branches extended from the dominant wormhole. The corresponding breakthrough pore volume is smallest among these four images, which is 0.97.

The acidized cores at 260 °F are also scanned and the CT images are shown in **Fig. 5.10**. In Fig. 5.10, the acid interstitial velocities are 5.94 cm/min, 8.59 cm/min and 15.57 cm/min from left to right. The optimal acid interstitial velocity is identified as 7.56 cm/min. Since the acid interstitial velocity is smaller than the optimal, the left image shows a thicker wormhole with little branches created. The other two images show the wormhole structures created by acid interstitial velocities that are higher than the optimal. As can be seen, wormhole branches are created along the dominant wormhole. Severe wormhole competitions can also be seen at the inlet.

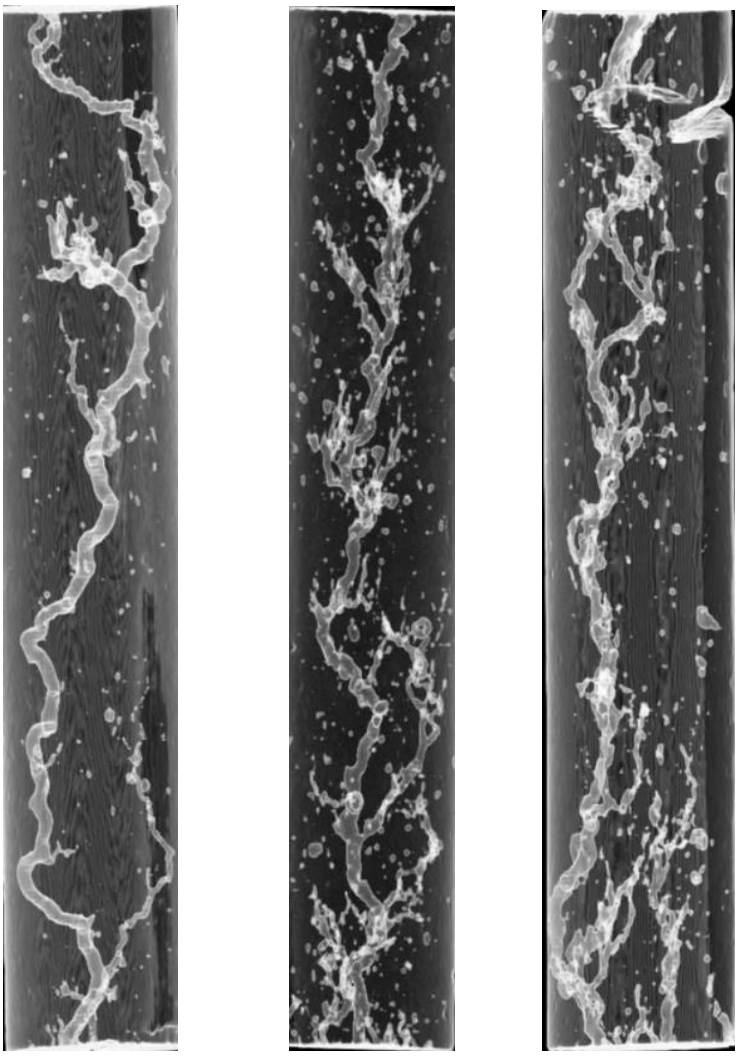

(1)	(2)	(3)
v_i = 5.94 cm/min	v_i = 8.59 cm/min	v_i = 15.57 cm/min
PV_{bt} = 1.03	PV_{bt} = 1.11	PV_{bt} = 1.44

Fig. 5.10 Wormhole CT images for acidized dolomite cores at 260 °F

Wormhole CT images for the acidized cores at 122 °F are shown below in **Fig. 5.11**. From image (1) to image (8), the acid interstitial velocities are increasing.

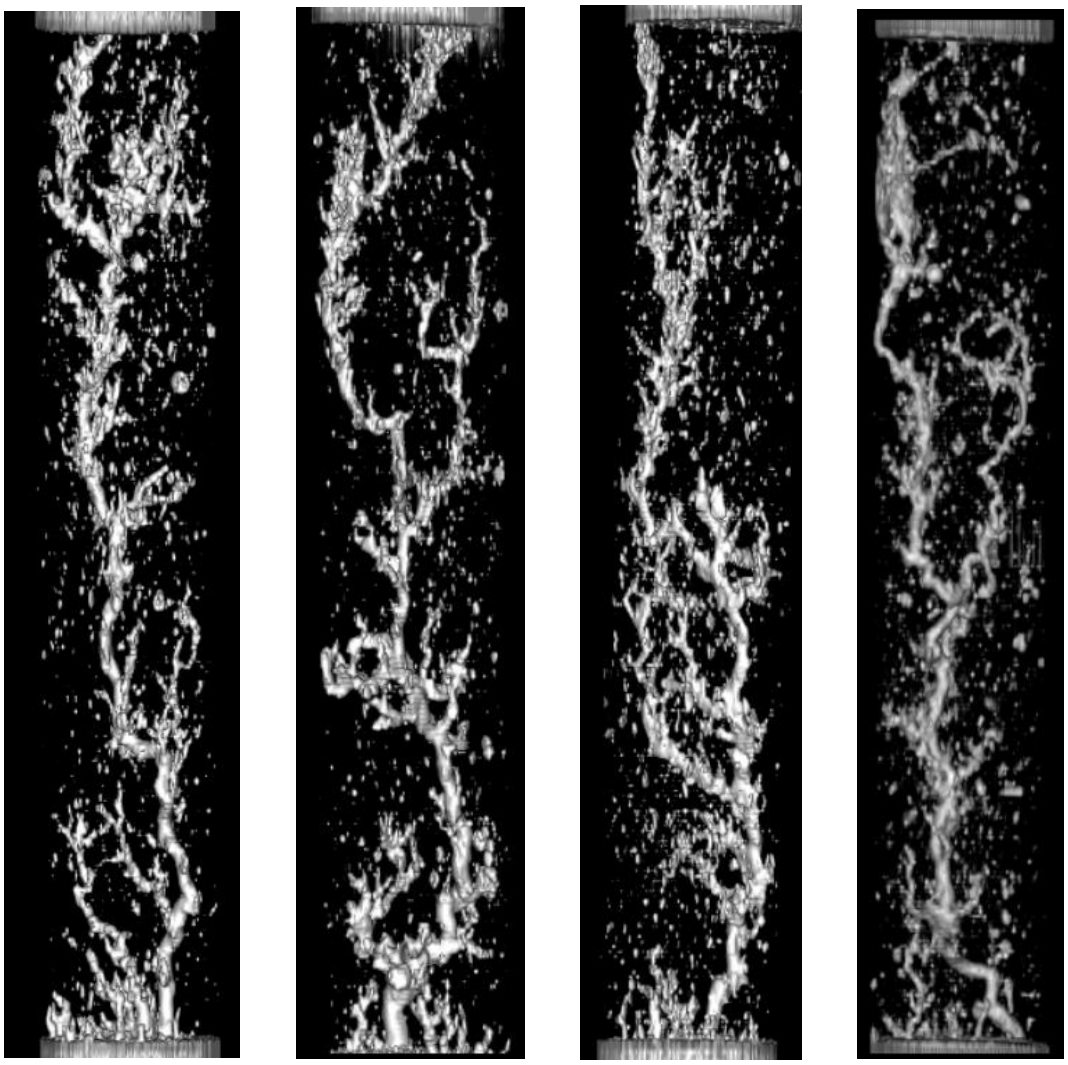

(1)	(2)	(3)	(4)
v_i = 0.67 cm/min	v_i = 0.7 cm/min	v_i = 0.89 cm/min	v_i = 1.16 cm/min
PV_{bt} = 2.95	PV_{bt} = 3.43	PV_{bt} = 2.22	PV_{bt} = 2.37

Fig. 5.11 Wormhole CT images for acidized dolomite cores at 122 °F

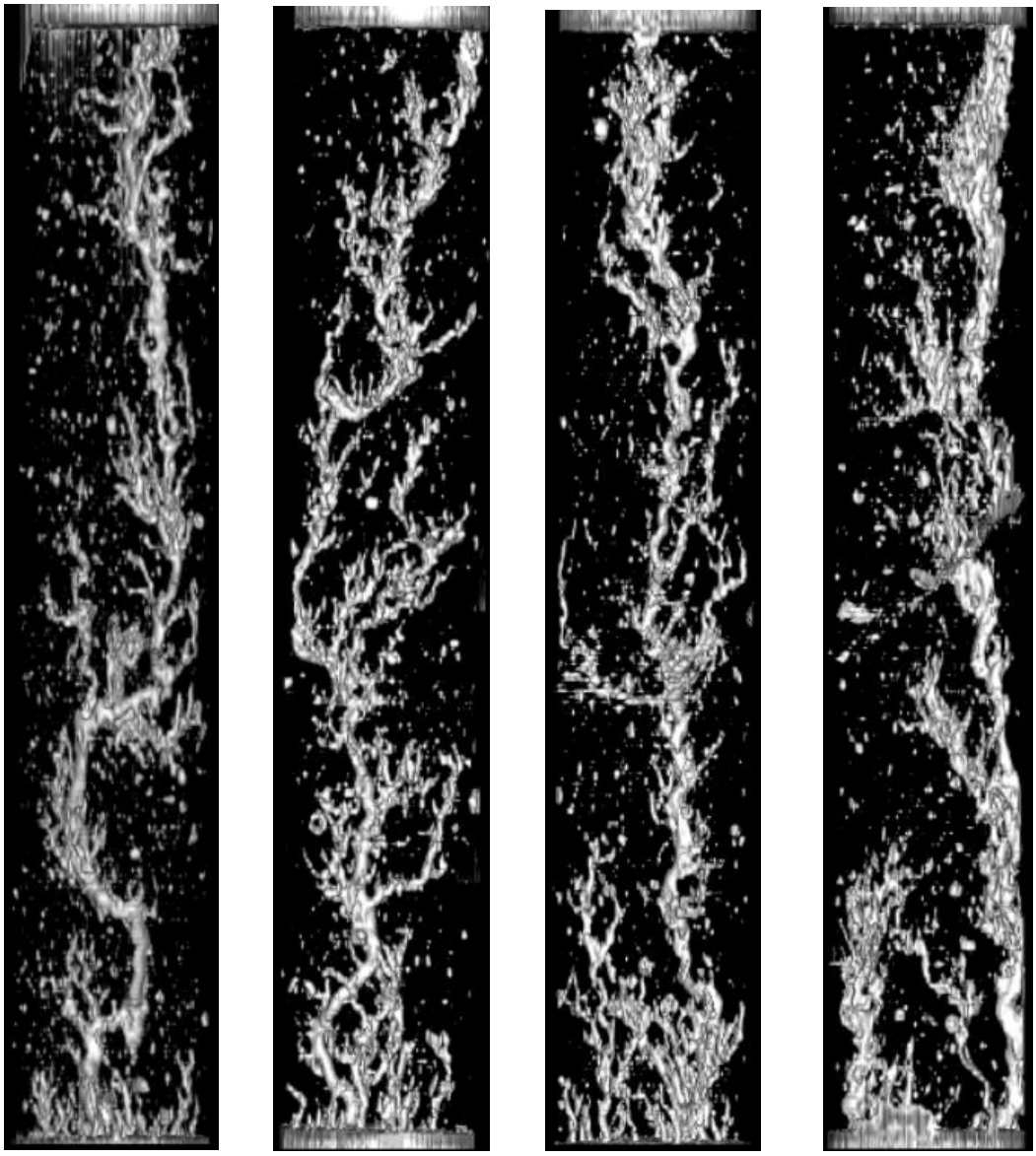

(5) v_i = 1.37 cm/min PV_{bt} = 2.09

(6) v_i = 1.62 cm/min PV_{bt} = 2.34

(7) v_i = 2.33 cm/min PV_{bt} = 2.42

(8) v_i = 4.67 cm/min PV_{bt} = 3.7

Fig. 5.11 Continued

In general, compared with the wormhole CT images at 185 °F and 260 °F, all the wormhole images at 122 °F present structures that have larger volumes. It is in agreement with larger breakthrough pore volumes for these cores.

If we focus on the inlet part of these wormholes (bottom of each image), we can see that there are severe wormhole competitions when the acid interstitial velocity is large. More small wormholes are created at the inlet part in images (6), (7) and (8) than other images. Besides, once the wormhole competitions disappear, these three images also present severe branching along the dominant wormhole.

Images (1) and (2) show that the wormholes at low acid interstitial velocities have a larger wormhole diameter at the inlet. Wormhole structures shown in image (4) is close to the optimal conditions with less branches and thinner diameter.

The breakthrough pore volumes at 122 °F are around twice as much as those at 185 °F and 260 °F, and are around four to five times breakthrough pore volumes of most limestone. This is due to the low surface reaction rate at 122 °F. It takes more time for pores growing into wormholes at the wormhole tip. This time is long enough for the acid loss creating other wormholes close to the wormhole tip. This is the reason that we can see much more tiny branches from the wormhole CT images at 122 °F at all the eight interstitial velocities, while these tiny branches cannot be seen from dolomite wormhole images at higher temperature, nor from limestone wormhole images.

5.5 Model-Based Explanation

If we analyze the optimal conditions in detail, we can see the $v_{i,opt}$ increases around 3 times from 122 °F to 185 °F, and $PV_{bt,opt}$ decreases around 2 times. In the meanwhile, the diffusion coefficients increases from 5.49×10^{-5} cm^2/s to 8.96×10^{-5} cm^2/s. Eq. 3-22 is clearly not applicable to this case. This means the overall reaction is not diffusion limited. Eq. 3-40 is used to analyze the experimental results, shown as Eq. 5-6 below.

$$\frac{v_{wh,opt1}}{v_{wh,opt2}} = \frac{\kappa_1}{\kappa_2} \tag{5-6}$$

κ depends on $v_{i,opt}$, as has been discussed in the calculation example of Section 2. Therefore, in order to use Eq. 5-6 above, specific quantities are needed, which are shown in **Table 5.2**. In the calculation, $r_{p,\mathrm{mode}}$ is 8 μm, and $\bar{L}_{p,\mathrm{mode}}$ is taken as 10 times the $r_{p,\mathrm{mode}}$, which is 80 μm. The diffusion coefficient D is calculated through Eq. 3-15; $E_f C_0^{m-1}$ is calculated through Eq. 3-4 and 3-5; K is calculated through Eq. 2-5; κ is calculated through Eq. 2-9.

Table 5.2a Parameters at 122 °F

D	5.49×10^{-5}	cm^2/s
$E_f C_0^{m-1}$	6.99×10^{-4}	cm/s
K	2.38×10^{-2}	cm/s
κ	6.79×10^{-4}	cm/s

Table 5.2b Parameters at 185 °F

D	8.96×10^{-5}	cm^2/s
$E_f C_0^{m-1}$	7.79×10^{-3}	cm/s
K	7.18×10^{-2}	cm/s
κ	6.27×10^{-3}	cm/s

Table 5.2c Parameters at 260 °F

D	1.43×10^{-4}	cm^2/s
$E_f C_0^{m-1}$	2.93×10^{-2} (*)	cm/s
K	1.49×10^{-1}	cm/s
κ	2.45×10^{-2}	cm/s

The $E_f C_0^{m-1}$ marked with * at 260 °F may not be correct, because m is calculated as 1.09 through Eq. 3-5. However, according to Lund et al. (1973), m should be within 0 and 1.

We first compare the optimal conditions at 122 °F and 185 °F. Experimental results comparison and model-based comparison are shown by Eq. 5-7 and Eq. 5-8.

$$\frac{v_{wh,opt185F}}{v_{wh,opt122F}} = \frac{4.65\text{cm/min}}{0.72\text{cm/min}} = 6.46 \tag{5-7}$$

$$\frac{v_{wh,opt185F}}{v_{wh,opt122F}} = \frac{\kappa_{185F}}{\kappa_{122F}} = \frac{6.27\times10^{-3}\text{cm}}{6.79\times10^{-4}\text{cm}} = 9.23 \tag{5-8}$$

We can see the comparison is not satisfactory. More detailed calculation is needed. However, we can conclude that the overall reaction rate depends on both surface reaction rate and diffusion rate between 122 °F and 185 °F. The increase of κ with increasing temperature is larger than the increase of D.

However, for optimal conditions between 185 °F and 260 °F, Eq. 3-42 can give good comparison. Experimental results comparison and model-based comparison are shown by Eq. 5-9 and Eq. 5-10.

$$\frac{v_{wh,opt260F}}{v_{wh,opt185F}} = \frac{7.07\text{cm/min}}{4.65\text{cm/min}} = 1.52 \tag{5-9}$$

$$\frac{v_{wh,opt260F}}{v_{wh,opt185F}} = \frac{D_{260F}}{D_{185F}} = \frac{1.43\times10^{-4}\,\text{cm}^2/\text{s}}{8.96\times10^{-5}\,\text{cm}^2/\text{s}} = 1.59 \tag{5-10}$$

This indicates that from 185 °F to 260 °F, the overall reaction rate is close to being diffusion limited. In fact, if we only look at Fig. 5.7, we can see from 185 °F to 260 °F, the optimal breakthrough pore volume increases a very limited amount, which is similar to that of limestone. Although $PV_{bt,opt}$ in this case is around 1, which is larger than most of $PV_{bt,opt}$ for limestone. But from the wormhole CT images, we can see there are no extra tiny wormhole branches along the dominant wormhole, like the case of 122 °F. The slight larger $PV_{bt,opt}$ is solely due to the lower acid dissolving power and smaller porosity in this case, which results in a lower acid capacity number.

Another interesting result is that from 122 °F to 185 °F, the optimal breakthrough pore volume decrease 2.2 times. Compared with limestone, this trend is opposite. In this temperature range, diffusion limitation increases with increasing

temperature, which causes a large increase in the overall reaction rate. It takes less time for pores growing into a wormhole at the wormhole tip, and wormhole propagates faster. During this limited time, the acid loss cannot create tiny branches due to its lower interstitial velocity at the wormhole wall close to the tip. Therefore, the injection volume becomes smaller with increasing temperature in this temperature range. However, once the overall reaction is fully diffusion limited, the temperature increase only causes a slight increase for $PV_{bt,opt}$, as are cases for limestone and high temperature dolomite. This is due to the slight increase of overall reaction rate for an already fully diffusion limited reaction.

5.6 Results Application

Based on the experimental results and model analysis, we can see the overall reaction between HCl and dolomite is mixed kinetics between 122 °F and 185 °F, with surface reaction rate being a constraint for the overall reaction rate; it is close to being diffusion limited between 185 °F and 260 °F. We can generate a treatment design chart for dolomite formations using the method described in Section 4.

If the temperature is below 185 °F, from Eq. 3-40, we can get

$$\frac{v_{wh,opt1}}{v_{wh,opt2}} = \frac{\kappa_1}{\kappa_2} = \frac{E_f C_0^{m-1}\big|_{T1}}{E_f C_0^{m-1}\big|_{T2}} \tag{5-11}$$

Substituting Hung's model into Eq. 5-11, we can get

$$\frac{v_{i,tip,opt1}}{v_{i,tip,opt2}} = \frac{E_f C_0^{m-1}\big|_{T1}}{E_f C_0^{m-1}\big|_{T2}} \tag{5-12}$$

At 122 °F, $v_{i,tip,opt} = 102.2\text{cm/min}$, $E_f C_0^{m-1} = 6.99 \times 10^{-4}\text{cm}$. Substituting them into Eq. 5-12, we can get Eq. 5-13 for temperature below 185 °F.

$$\frac{v_{i,tip,opt1}}{102.2\text{cm/min}} = \frac{E_f C_0^{m-1}\big|_{T1}}{6.99\times10^{-4}\text{cm}} \tag{5-13}$$

If the temperature is above 185 °F, we have Eq. 5-14 below.

$$\frac{v_{i,tip,opt1}}{v_{i,tip,opt2}} = \frac{D\big|_{T1}}{D\big|_{T2}} \tag{5-14}$$

At 185 °F, $v_{i,tip,opt} = 657.8\text{cm/min}$, $D = 8.95 \times 10^{-5}\text{cm}^2/\text{s}$. Substituting these two values into Eq. 5-14, we can get Eq. 5-15 for temperature above 185 °F.

$$\frac{v_{i,tip,opt1}}{657.8\text{cm/min}} = \frac{D\big|_{T1}}{8.95\times10^{-5}\text{cm}^2/\text{s}} \tag{5-15}$$

If we plot Eq. 5-13 and Eq. 5-15 in a same plot, we have **Fig. 5.12** as the treatment design chart for the dolomite formation. The red curve shows the relationship between the optimal wormhole tip interstitial velocity and the temperature for dolomite rocks. A transition points at 185 °F divides this curve into two regions, one for mixed kinetics and the other one for diffusion limited kinetics. If the overall reaction is diffusion limited when the temperature is below 185 °F, the relationship is described by the blue dash line. This is usually for HCl/limestone.

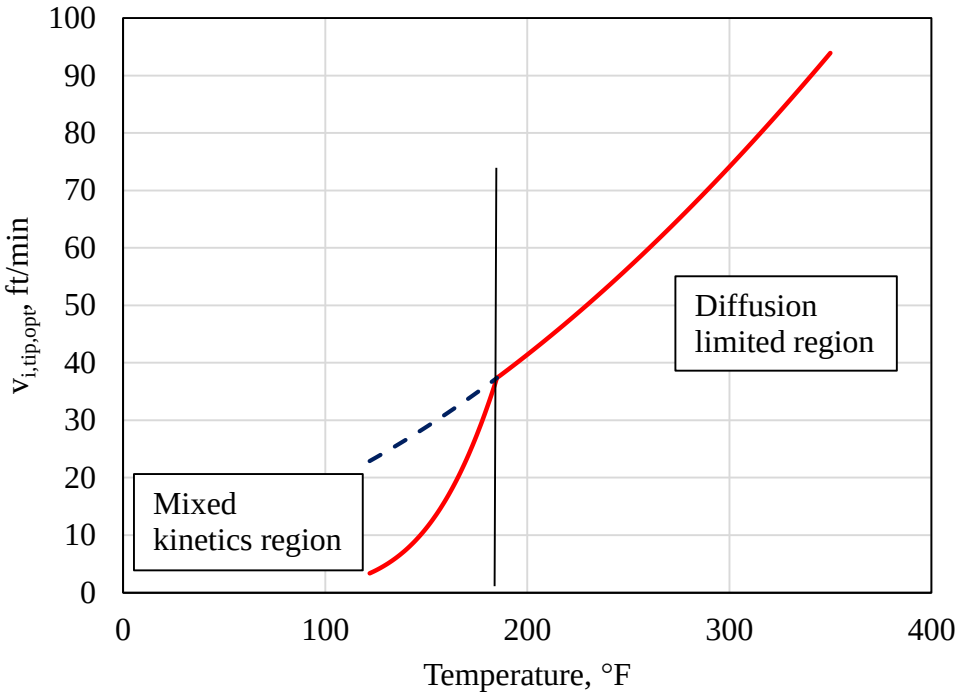

Fig. 5.12 Field treatment design chart for Silurian dolomite of 15 wt% HCl

Note that 185 °F is one of the test temperature for our acidizing coreflood experiments. It is used as a transition temperature for mixed kinetics and diffusion limited kinetics here. However, the exact temperature may not be 185 °F. Lund et al. (1973) showed that the dissolution between HCl and dolomite becomes diffusion limited at around 212 °F through rotating disk study. However, once this temperature is determined, the design chart in Fig. 5.12 can be readily modified.

Besides the treatment design chart, the following suggestions can also be considered before designing a treatment.

1. If reservoir temperature is low, based on wormhole efficiency relationship of 122 °F, more acid volume is needed.
2. If reservoir temperature is high, dolomite rock behaves the same as limestone. Although $PV_{bt,opt}$ is larger than that of limestone, it is solely due to lower acid capacity number, and is not related with lithology (different surface reaction rate) at all.

6 CONCLUSIONS AND RECOMMENDATIONS

6.1 Conclusions

This dissertation presents a model to calculate the optimal conditions of acidizing coreflood experiments. This model comprises three parts, pore scale, wormhole tip scale and core scale. Based on this model, sensitivities of temperature and acid concentration are analyzed. A new method to make use of lab acidizing results to field treatment is developed. Finally, this model is used to analyze dolomite acidizing behavior. The conclusions of this study can be summarized as below.

1. The model developed in this study can predict optimal conditions of acidizing coreflood experiment successfully. The calculated optimal conditions are satisfactorily close to our lab measurements.
2. Wormhole tip interstitial velocity governs wormhole propagation. It is the basis to study the optimal conditions of different scales. Being general to flow geometries, it solely depends on the pore size distribution and acid/rock reaction.
3. For fully diffusion limited reactions, the average/instantaneous optimal wormhole propagation velocity is linearly proportional to the acid diffusion coefficient. This is proven both experimentally and theoretically in this study.
4. If HCl concentration is less than 24%, increasing concentration results in an increase of optimal interstitial velocity. If HCl concentration is larger than 24%, the optimal interstitial velocity decreases with concentration. However, average optimal wormhole propagation velocity always increases with increasing acid

concentration. The optimal breakthrough pore volume always decreases with increasing acid concentration, due to increase of acid capacity.

5. A method is developed to upscale lab optimal acid injection rate to field treatment. The acid pumping rate should keep increasing during the treatment to compensate for acid loss and concentration decrease. A general matrix treatment design method is developed for limestone formations.
6. For dolomite, wormholes cannot be created at room temperature with a reasonable acid volume. With increasing temperature, the overall reaction eventually changes from being surface reaction limited to diffusion limited. When the overall reaction is in mixed kinetics, the optimal breakthrough pore volume decreases with increasing temperature. Once it becomes diffusion limited, wormholing behavior is the same as that of limestone. A general matrix treatment design method is developed for dolomite formations.

6.2 Recommendations

1. The correlation for breakthrough pore volume has limitations. The current correlation is a combination of linear flow equation and Hung's model. However, recent experiments show that it is significantly affected by pore size distribution. More deterministic method is needed.
2. Average pore length in this model is involved in the porous medium model. In this study, this value is estimated based on Micro-CT data. If a more representative

measurement is available, this model can be more accurate and more detailed analysis can be made.

3. The fluid loss behavior merits further investigation, both in lab conditions and in field conditions. This can be achieved through numerical modeling. This fluid loss model can be used to study wormhole diameter in more detail. It is also helpful for optimal breakthrough pore volume calculations.

REFERENCES

Bazin, B. 2001. From Matrix Acidizing to Acid Fracturing: A Laboratory Evaluation of Acid/Rock Interactions. SPE Production & Facilities 16 (1): 22-29.

Buijse, M.A. and Glasbergen, G. 2005. A Semiempirical Model to Calculate Wormhole Growth in Carbonate Acidizing. Paper presented at the SPE Annual Technical Conference and Exhibition, Dallas, Texas. SPE 96892. DOI: 10.2118/96892-ms.

Conway, M.W., Asadi, M., Penny, G.S. et al. 1999. A Comparative Study of Straight/Gelled/Emulsified Hydrochloric Acid Diffusivity Coefficient Using Diaphragm Cell and Rotating Disk. Paper presented at the SPE Annual Technical Conference and Exhibition, Houston, Texas. Society of Petroleum Engineers 00056532. DOI: 10.2118/56532-ms.

Daccord, G., Lenormand, R., and Liétard, O. 1993. Chemical Dissolution of a Porous Medium by a Reactive Fluid—I. Model for the "Wormholing" Phenomenon. Chemical Engineering Science 48 (1): 169-178. DOI: http://dx.doi.org/10.1016/0009-2509(93)80293-Y

Daccord, G., Touboul, E., and Lenormand, R. 1989. Carbonate Acidizing: Toward a Quantitative Model of the Wormholing Phenomenon. SPE Production Engineering 4 (1): 63-68. DOI: 10.2118/16887-pa

Domelen, M.S.V., Talib, N.N., and Glasbergen, G. 2011. Return to Basics and Proper Planning Opens the Possibility to Acid Stimulate a Difficult Chalk Formation. Paper presented at the SPE European Formation Damage Conference, Noordwijk, The Netherlands. SPE SPE-144159-MS. DOI: 10.2118/144159-ms.

Dong, K., Jin, X., Zhu, D. et al. 2014. The Effect of Core Dimensions on the Optimal Acid Flux in Carbonate Acidizing. Society of Petroleum Engineers. DOI: 10.2118/168146-MS.

Dong, K. 2012. Experimental Investigation for the Effect of the Core Length on the Optimal Acid Flux in Carbonate Acidizing, Master thesis, Texas A&M University, College Station, Texas (August 2012)

Etten, R.J. 2015. Experimental Investigation on the Effect of Permeability on the Optimum Acid Flux in Carbonate Matrix Acidizing, Master thesis, Texas A&M University, College Station, Texas (May 2015)

Fredd, C.N. and Fogler, H.S. 1999. Optimal Conditions for Wormhole Formation in Carbonate Porous Media: Influence of Transport and Reaction. SPE Journal 4 (3): 196-205. DOI: 10.2118/56995-pa

Furui, K., Burton, R.C., Burkhead, D.W. et al. 2010. A Comprehensive Model of High-Rate Matrix Acid Stimulation for Long Horizontal Wells in Carbonate Reservoirs. Paper presented at the SPE Annual Technical Conference and Exhibition, Florence, Italy. SPE SPE-134265-MS. DOI: 10.2118/134265-ms.

Gong, M. and El-Rabaa, A.M. 1999. Quantitative Model of Wormholing Process in Carbonate Acidizing. Paper presented at the SPE Mid-Continent Operations Symposium, Oklahoma City, Oklahoma. Society of Petroleum Engineers 00052165. DOI: 10.2118/52165-ms.

Guin, J.A. and Schechter, R.S. 1971. Matrix Acidization with Highly Reactive Acids. Society of Petroleum Engineers Journal 11 (4): 390-398. DOI: 10.2118/3091-pa

Guin, J.A., Schechter, R.S., and Silberberg, I.H. 1971. Chemically Induced Changes in Porous Media. Industrial & Engineering Chemistry Fundamentals 10 (1): 50-54. DOI: 10.1021/i160037a010

Harris, O.E., Hendrickson, A.R., and Coulter, A.W. 1966. High-Concentration Hydrochloric Acid Aids Stimulation Results in Carbonate Formations. DOI: 10.2118/1654-PA

Hoefner, M.L. and Fogler, H.S. 1987. Role of Acid Diffusion in Matrix Acidizing of Carbonates. Journal of Petroleum Technology 39 (2): 203-208. DOI: 10.2118/13564-pa

Hoefner, M.L. and Fogler, H.S. 1988. Pore Evolution and Channel Formation During Flow and Reaction in Porous Media. AIChE Journal 34 (1): 45-54. DOI: 10.1002/aic.690340107

Huang, T., Zhu, D., and Hill, A.D. 1999. Prediction of Wormhole Population Density in Carbonate Matrix Acidizing. Paper presented at the SPE European Formation Damage Conference, The Hague, Netherlands. SPE 54723. DOI: 10.2118/54723-ms.

Hung, K.M., Hill, A.D., and Sepehrnoori, K. 1989. A Mechanistic Model of Wormhole Growth in Carbonate Matrix Acidizing and Acid Fracturing. Journal of Petroleum Technology 41 (01). DOI: 10.2118/16886-pa

Kent, A.W., Burkhead, D.W., Burton, R.C. et al. 2013. Intelligent Completions and Un-Cemented Liners Combine to Provide a Fully Completed Solution with Zonal Isolation in Norway. Society of Petroleum Engineers. DOI: 10.2118/166209-MS.

Levich, Veniamin G. *Physicochemical Hydrodynamics*. 1962. Englewood Cliffs, N.J.: Prentice Hall, Inc

Lund, K., Fogler, H.S., and Mccune, C.C. 1973. Acidization—I. The Dissolution of Dolomite in Hydrochloric Acid. Chemical Engineering Science 28 (3): 691-IN691. DOI: http://dx.doi.org/10.1016/0009-2509(77)80003-1

Lund, K., Fogler, H.S., Mccune, C.C. et al. 1975. Acidization—Ii. The Dissolution of Calcite in Hydrochloric Acid. Chemical Engineering Science 30 (8): 825-835. DOI: 10.1016/0009-2509(75)80047-9

Panga, M.K.R., Ziauddin, M., and Balakotaiah, V. 2005. Two-Scale Continuum Model for Simulation of Wormholes in Carbonate Acidization. AIChE Journal 51 (12): 3231-3248. DOI: 10.1002/aic.10574

Schechter, R.S. and Gidley, J.L. 1969. The Change in Pore Size Distribution from Surface Reactions in Porous Media. AIChE Journal 15 (3): 339-350. DOI: 10.1002/aic.690150309

Schechter, Robert S. *Oil Well Stimulation*. 1992. Englewood Cliffs, New Jersey: Prentice-Hall, Inc

Wang, Y., Hill, A.D., and Schechter, R.S. 1993. The Optimal Injection Rate for Matrix Acidizing of Carbonate Formations. Paper presented at the SPE Annual Technical Conference and Exhibition, Houston, Texas. SPE 26578. DOI: 10.2118/26578-ms.

Zakaria, A.S., Nasr-El-Din, H.A., and Ziauddin, M. 2015. Predicting the Performance of the Acid-Stimulation Treatments in Carbonate Reservoirs with Nondestructive Tracer Tests. SPE Journal. DOI: 10.2118/174084-PA

Ziauddin, M.E. and Bize, E. 2007. The Effect of Pore-Scale Heterogeneities on Carbonate Stimulation Treatments. Paper presented at the SPE Middle East Oil and Gas Show and Conference, Kingdom of Bahrain. Society of Petroleum Engineers SPE-104627-MS. DOI: 10.2118/104627-ms.

APPENDIX A

This appendix shows the thin section images for another seven types of carbonate rocks, including Indiana limestone (6 mD), Austin Chalk, Edwards White limestone, Edwards Yellow limestone, Lenders limestone, Marble and Indiana limestone (240 mD).

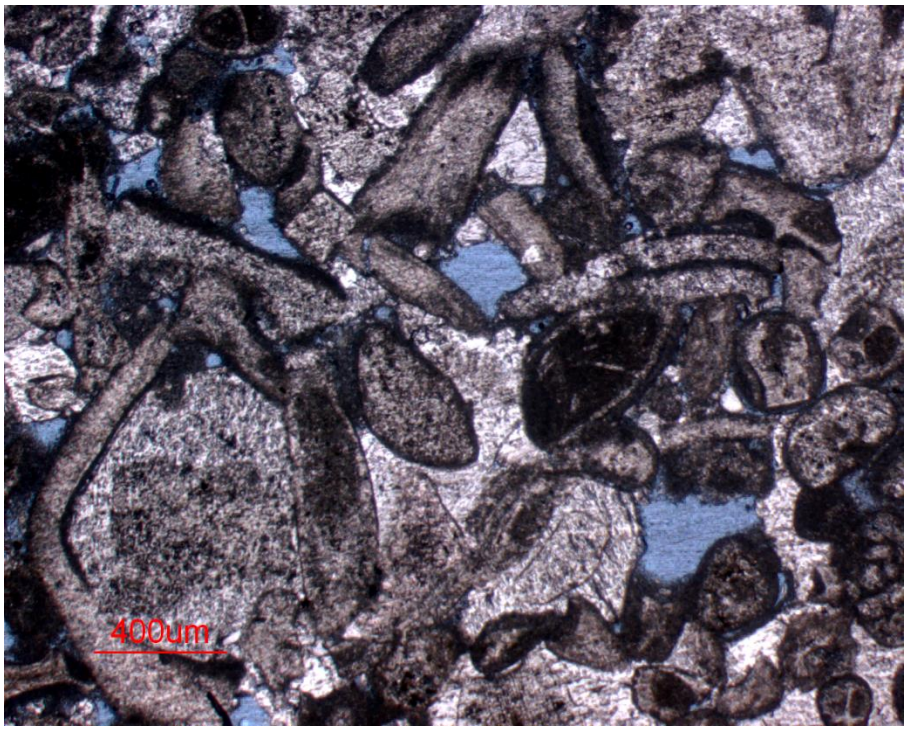

Fig. A.1 Thin section image for Indiana limestone (6 mD) with 10×Magnification

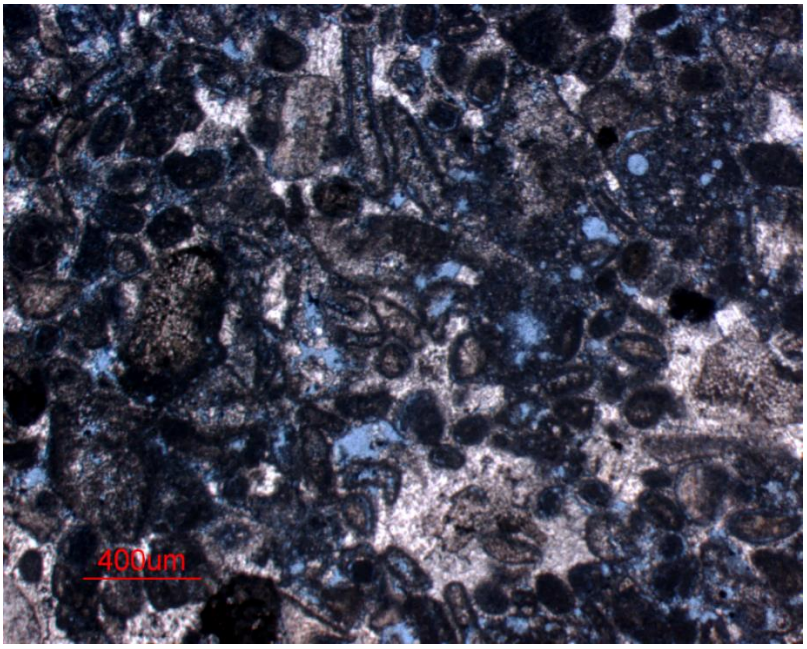

Fig. A.2a Thin section image for Austin Chalk with 10×Magnification

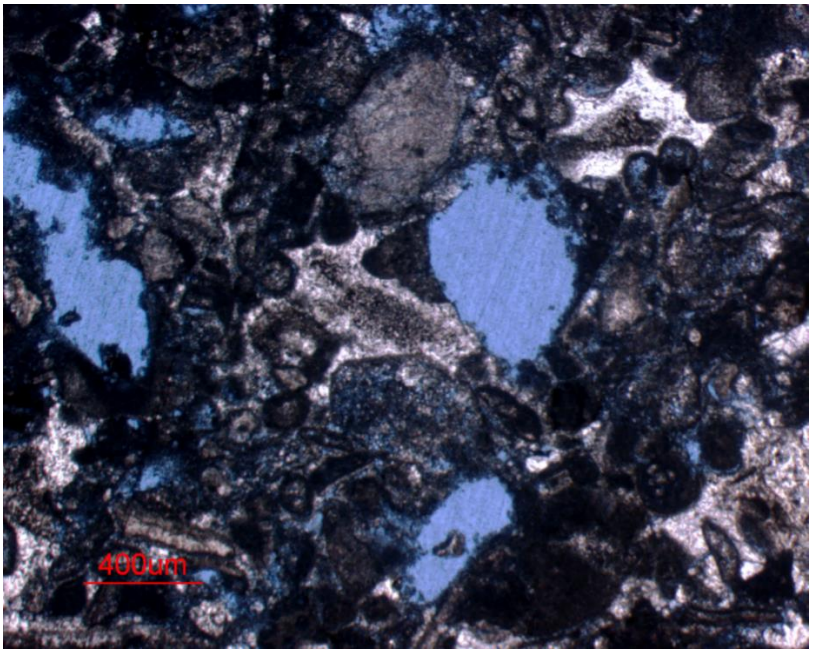

Fig. A.2b Thin section image for Austin Chalk with 20×Magnification

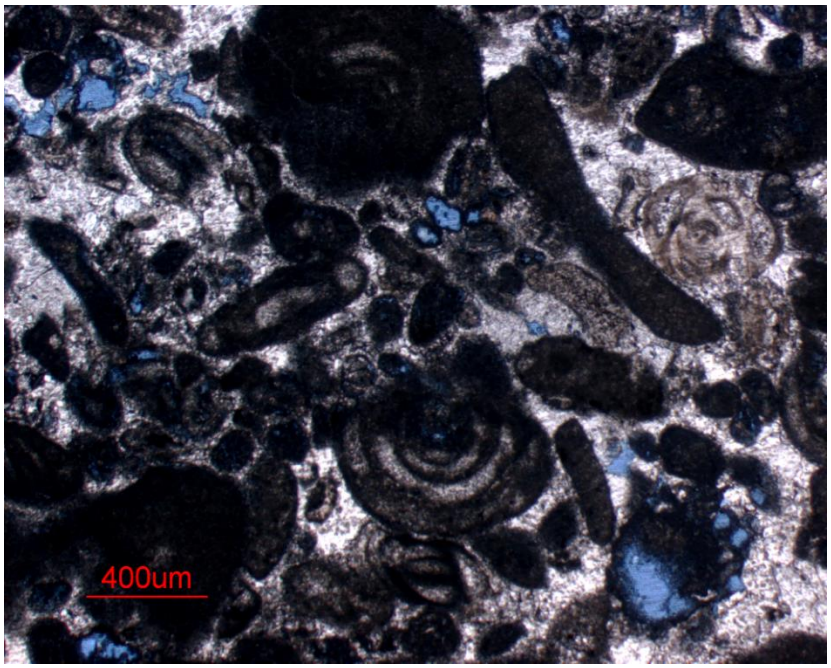

Fig. A.3a Thin section image for Edward White limestone with 10×Magnification

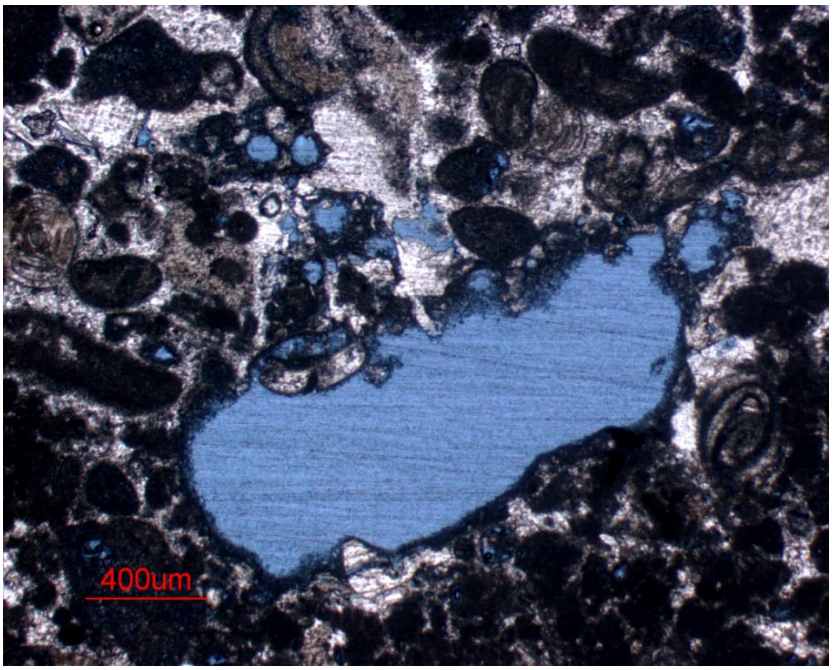

Fig. A.3b Thin section image for Edward White limestone with 20×Magnification

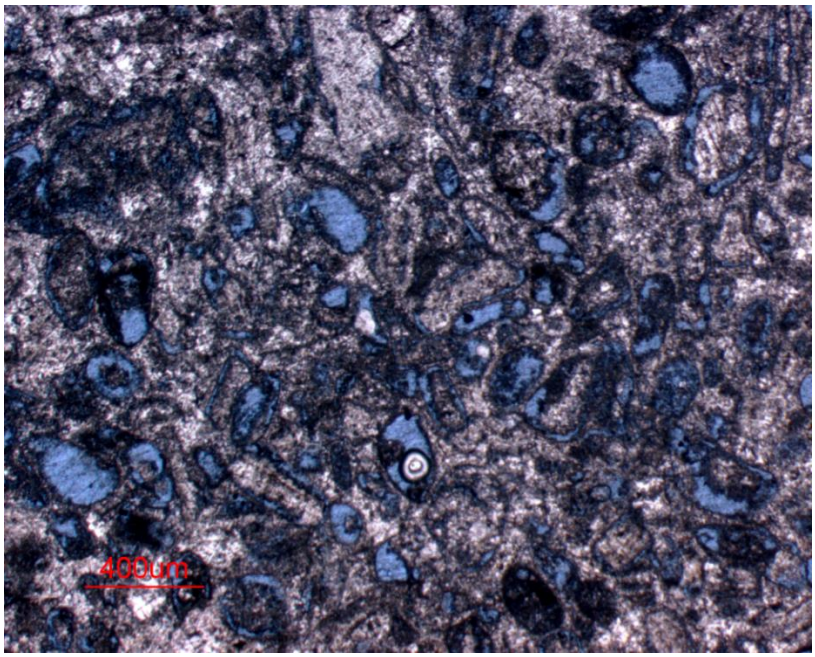

Fig. A.4a Thin section image for Edward Yellow limestone with 10×Magnification

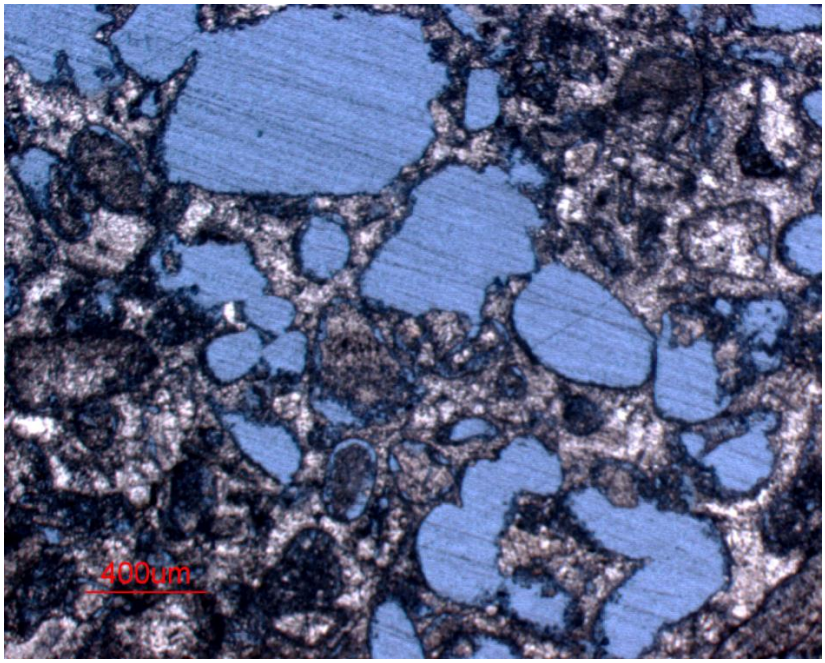

Fig. A.4b Thin section image for Edward Yellow limestone with 20×Magnification

Fig. A.5 Thin section image for Lenders limestone with 10×Magnification

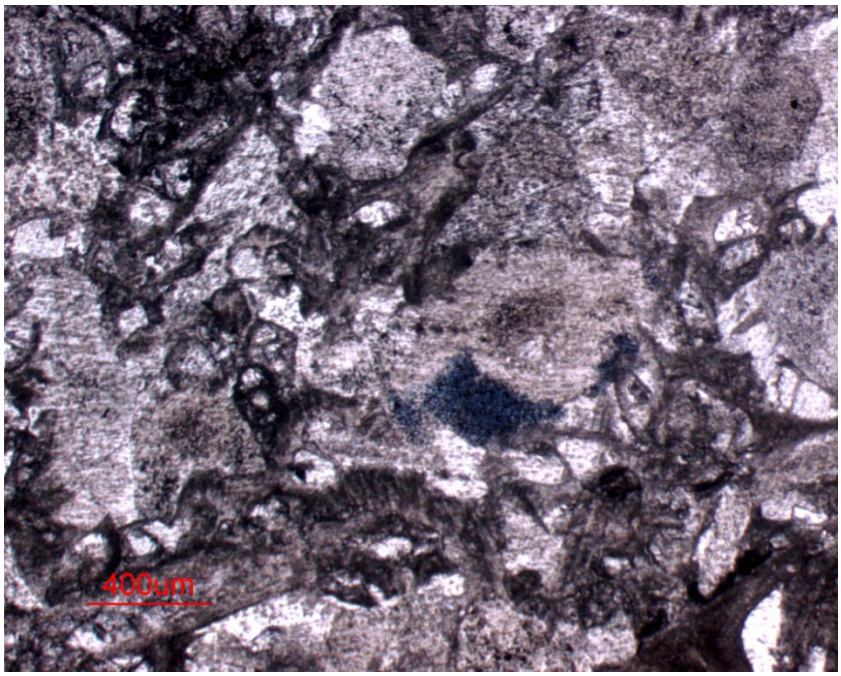

Fig. A.6 Thin section image for Marble with 10×Magnification

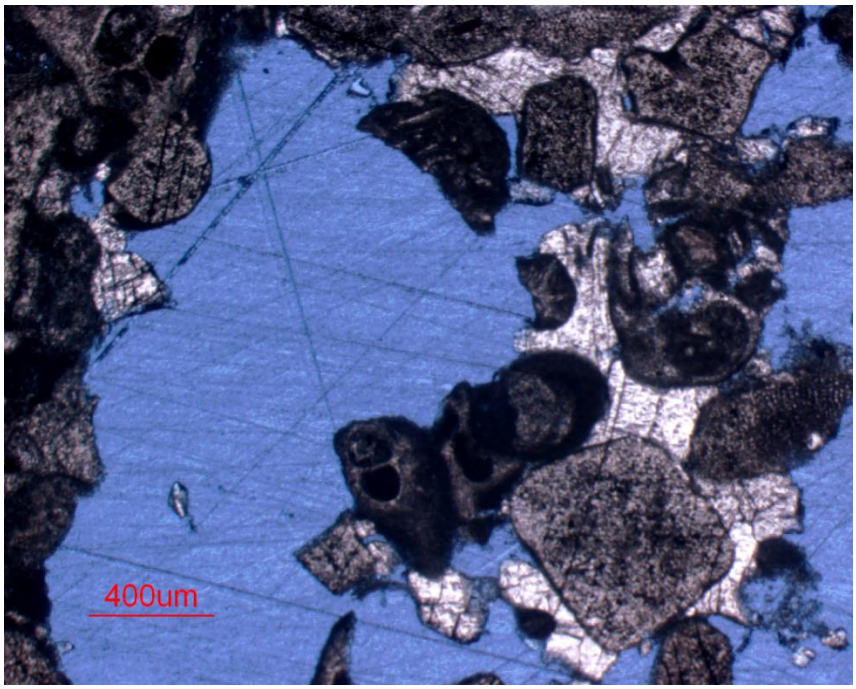

Fig. A.7 Thin section image for Indiana limestone (240 mD) with 10×Magnification

APPENDIX B

The X-ray diffraction measurement for dolomite cores shows that more than 99% of the mineral is dolomite. The raw measurement data is shown in **Fig. B.1**.

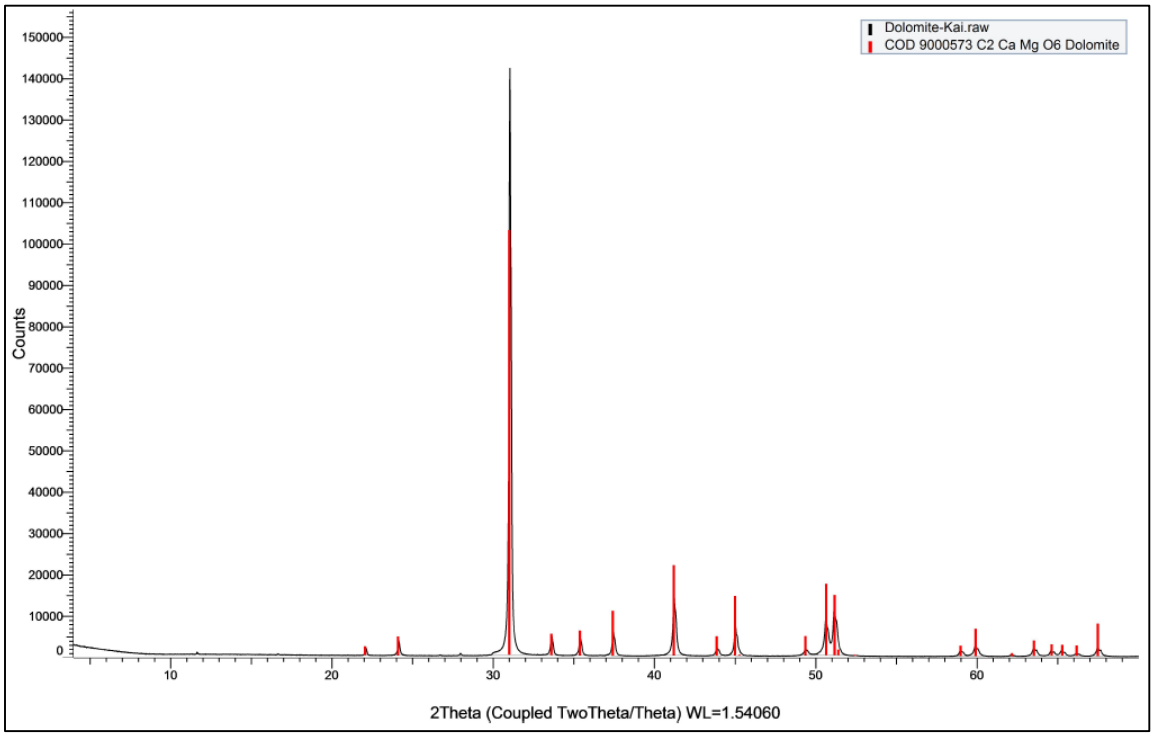

Fig. B.1 Raw X-ray diffraction measurement data

The original acidizing coreflood experimental data carried out for this study are shown from **Table B-1** to **Table B-5** below.

Table B-1 Experimental data for 28 wt% HCl/ Indiana limestone (13 mD) at room temperature

Core#	Dry weight	Wet weight	Permeability	Porosity	Acid injection rate	Acid interstitial velocity	PV_{bt}
	gram	gram	mD		ml/min	cm/min	
1	526.03	557.75	8.5	14%	3.3	2.11	0.25
2	546.49	569.73	2	10%	6	5.25	0.26
3	522.61	555.07	13.3	14%	1.4	0.88	0.31
4	525.76	556.07	12.2	13%	1.2	0.8	0.28
5	526.21	556.95	8.5	13%	0.8	0.53	0.65
6	525.5	556.45	9	13%	2.05	1.35	0.28
7	522.13	554.83	12.8	14%	10	6.21	0.31
8	524.11	556.58	9.1	14%	2.15	1.35	0.3
9	543.48	570.73	2.4	12%	1.81	1.35	0.21

Table B-2 Experimental data for 28 wt% HCl/ Desert Pink limestone at room temperature

Core#	Dry weight	Wet weight	Permeability	Porosity	Acid injection rate	Acid interstitial velocity	PV_{bt}
	gram	gram	mD		ml/min	cm/min	
1	438.39	498.76	36.4	26%	10	3.37	0.44
2	437.05	499.1	51.36	27%	16	5.24	0.44
3	431.03	493.87	54.13	27%	6.2	2	0.69
4	436.67	499.18	80.8	27%	3.7	1.2	0.95
5	445.74	504.91	55.1	26%	13	4.46	0.46
6	444.73	504.2	58.21	26%	4	1.37	0.82
7	444.73	504.2	42.6	26%	7.8	2.67	0.45
8	439.39	497.72	47.9	25%	5.7	1.99	0.84
9	430.87	492.34	49.4	27%	6	1.98	0.53
10	445.23	503.35	69.9	25%	16	5.59	0.51
11	444.78	502.76	38.6	25%	4.6	1.61	0.49

Table B-3 Experimental data for 15 wt% HCl/ Silurian Dolomite at 122 °F

Core#	Dry weight	Wet weight	Permeability	Porosity	Acid injection rate	Acid interstitial velocity	PV_{bt}
	gram	gram	mD		ml/min	cm/min	
1	557.93	580.13	1.9	10.0%	1.5	1.37	2.09
2	559.11	580.88	4	9.0%	5	4.67	3.7
3	557.84	579.64	7	9.0%	2.5	2.33	2.42
4	553.37	576.2	7.5	10.0%	1	0.89	2.22
5	557.92	579.74	6.6	9.0%	0.75	0.7	3.43
6	557.07	579.64	10.3	10.0%	1.8	1.62	2.34
7	561.12	579.41	3.3	8.0%	0.6	0.67	2.95
8	565.52	585.75	2.9	9.0%	1.15	1.16	2.37

Table B-4 Experimental data for 15 wt% HCl/ Silurian Dolomite at 185 °F

Core#	Dry weight	Wet weight	Permeability	Porosity	Acid injection rate	Acid interstitial velocity	PV_{bt}
	gram	gram	mD		ml/min	cm/min	
1	581.37	601.6	1.9	8.7%	1.7	1.71	3.82
2	570.94	593.77	7.2	9.9%	3	2.67	1.16
3	571.12	594.48	16.8	10.1%	6	5.22	1.4
4	574.86	593.86	5.4	8.2%	1.7	1.82	2.88
5	579.34	598.24	4.5	8.2%	2	2.15	1.34
6	556.66	576.93	16.5	8.7%	3.9	3.91	0.97

Table B-5 Experimental data for 15 wt% HCl/ Silurian Dolomite at 260 °F

Core#	Dry weight	Wet weight	Permeability	Porosity	Acid injection rate	Acid interstitial velocity	PV_{bt}
	gram	gram	mD		ml/min	cm/min	
1	564.75	585.28	5.8	8.9%	6	5.94	1.03
2	575.83	596.04	9.7	8.7%	4	4.02	1.93
3	563.9	587.8	20.2	10.3%	10.1	8.59	1.11
4	571.26	592.14	6.1	9.0%	16	15.57	1.45